Analysis of Random Curve and Vortex Filament Topology

by

Anda Xiong

A thesis submitted to the

University of Birmingham

for the degree of

DOCTOR OF PHILOSOPHY

Theoretical Physics Group

School of Physics and Astronomy

College of Engineering and Physical Sciences

University of Birmingham

April 2022

ABSTRACT

This thesis covers a range of topics through the analysis of random curves and vortex filaments in various contexts. We find that phase vortices in random wave model, which is a type of model for quantum and wave chaos, are closed random walks whose length distribution is of universal scaling relation. We analyze the phase vortex in two-plus-one dimensional random waves and find that they can be classified into three types based on length: small loops whose behaviour is model-dependent, large loops that are closed random walks, and vortex lines that are long enough to penetrate through the space before getting closed.

Since vortex loops are closed random walks, we investigate the knot probability of them by generating a very large amount of sampling of equilateral and non-equilateral closed random polygons and determining their knot type by the Alexander polynomial. Then with statistical analysis we confirm a general probability equation for knots in random polygons. We also investigate a series of problems regarding to the knot probability of random polygons.

The vortex in three-plus-one-dimensional space-time is two-dimensional surface and we call them vortex worldsheet. We find that while the topology of the vortex worldsheet is relativistically invariant, the topology of the vortex in the time-slice of observers in different reference frame changes with the Lorentz boost. We discuss constructions we used for the scenario and the superluminal region on the vortex world sheet, which is where the speed of phase vortex exceeds the light speed.

DEDICATION

Dedicated to my parents

ACKNOWLEDGMENTS

I thank my parents for their forever love and support. My parents have their approach to the meaning of life and essence of nature via entrepreneurship and art. While my pursuit of physics is new in our family, the spirit of curiosity and persistence is passed through generation. I am grateful to my supervisor, Professor Mark R Dennis, for his guidance on the thesis. He is truly a physicist of wisdom and optimism, with his good taste and insight to theoretical physics. I also thank Xiaoqian Xu for staying with me and keep me from starving by her wonderful cooking skill. I thank my colleagues in the theory group on the fourth floor of physics east building, such as Enrico, Gabriel, Ben, Jordan, Jack with whom I shared office, and everyone I have worked together with, especially Professor Stu Whittington, who is truly a British gentleman of kindness, patience, and wisdom. I thank Sandy Taylor for leaving his data to me so that I can carry on the analysis to knot probability. I thank organizers to the conference held in Beijing 2019 on knotted field, for it has been great inspiration to me.

For the ideal I hold

Even a thousand times of death

does not make me regret

Qu, yuan, *Li-Sao*

Contents

List of Figures

List of Tables

Chapter One

Introduction

1.1 Motivation and Outline

Physics is a subject for the principles of the nature and matters it contains. In early stage of mechanics, people focus on the dynamics of single objects in ideal cases such as how will they move when there are forces exerted. Then, as human knowledge develops, there begin interests on more complicated dynamics, such as chaos and statistical physics for random phenomena.

Chaos describes the unpredictability of physical systems that evolve with exponential uncertainty regarding to the measured initial condition. If a system is chaotic, then it has at least one positive Lyapunov exponent [Spr03; Str18], which is a measure of expansion of linearized neighborhood of certain point. Therefore, since in reality there is always inevitable error in the measurement, then as such error grows exponentially in time, finally there may be a non-negligible difference between predictions made based on early observation and reality. Similarly, bifurcation describes sudden non-negligible changes made when parameters in the system are changed slightly. Both chaos and bifurcation contribute to the complexity of

dynamics because they make predictions become more difficult by their nature of uncertainty.

Assuming determinism in macroscopic world, then theory of probability is only a method to describe the world as it appears to us rather than what it truly is, as chaos and bifurcation can make things appear happening by chance while in fact happening in determinism. For example, in theory of probability, throwing a dice has result in equal probability of one-sixth for each face, however, in reality, by the time the dice is thrown, its future is determined and there is only one result of full certainty existing in the future, yet it only appear to observers that each face has equal probability because the judgment of the observer is limited by his ignorance to the dice. Had the observer have enough information required for prediction, such as the forces given by the hand to the dice, the moment of inertia of the dice, the air resistance that the dice endure during the process, the hardness of the table it falls on, and many other information, and had the observer have enough capability of calculating the whole process, then the observer will see the result of throwing a dice as happening in certainty rather than by chance. Chaos and bifurcation causes observers to require much more information for accurate prediction, but the "unpredictability" they cause is only for observers' calculation, while they do not break the determinism of the incidence in objective reality.

While chaos and bifurcation make dynamics in macroscopic world complicated and make people turn to theory of probability, quantum chaos, on the other hand, attracts people's attention as a counterpart of it in microscopic world. Just like light has wave-particle duality, chaos in the macroscopic world is often considered in terms of the chaotic dynamics of point particles, while quantum (wave) chaos is studied in terms of the solutions of a wave equation such as Schrodinger's equation. As studied in chapter 2, quantum chaos and wave chaos are modeled by

the Random Wave Model (RWM) and we specifically study the phase vortex, which is the zero of both real and imaginary part of the field, in waves of various dispersion relation. Unlike classical chaos in macroscopic world that there is no randomness required in the explicit construction of dynamical equations, quantum chaos, however, has explicit randomness in the wave equation. Therefore, both classical chaos and quantum/wave chaos embody essence of "unpredictability", but they are different in the way of exhibiting random probability.

Both the trajectory of particles in classical chaos and the vortex line in quantum/wave chaos in three-dimensional space are one-dimensional line, and a specific area of studying one-dimensional lines in three-dimensional space is the knot theory. A knot is an embedding of a circle, which is a closed one-dimensional line, in three-dimensional space. In chapter 3, we study knot theory in particular the probability of knots in closed random walks, as we find in chapter 2 that vortices in random wave model are closed random walks. In chapter 3, we raise and verify a general equation for the knot probability in random polygons, which is an equivalent name for closed random walks. We find that the knot probability of random polygons in R^3 is different from previous knowledge in Z^3. We verify these results by a large data simulation providing high accuracy for fitting. The simulation includes generating equilateral and non-equilateral random polygons and determining the knot type by the Alexander polynomial. I have independently completed necessary algorithms for calculation, but the data is generated by my supervisor's former postdoc Alexander Taylor who left before completing the analysis. I did the whole analysis and reach to conclusions in chapter 3.

In chapter 4, we study the vortex world sheet in complex wave field. Unlike in previous chapters where the systems are of randomness, in this chapter we study vortex worldsheet out of direct construction of complex wave field. We study the

vortex in three-plus-one-dimensional space-time where the vortex forms vortex world sheet, which is two-dimensional surfaces. We find that while the topology of vortex worldsheet is invariant in space-time, the topology such as knot type in time-slice is dependent to frame of reference, and Lorentz boost leads to topology change in the eyes of observers in time. We also calculate the speed on the vortex sheet and discuss the superluminal effect of phase vortices.

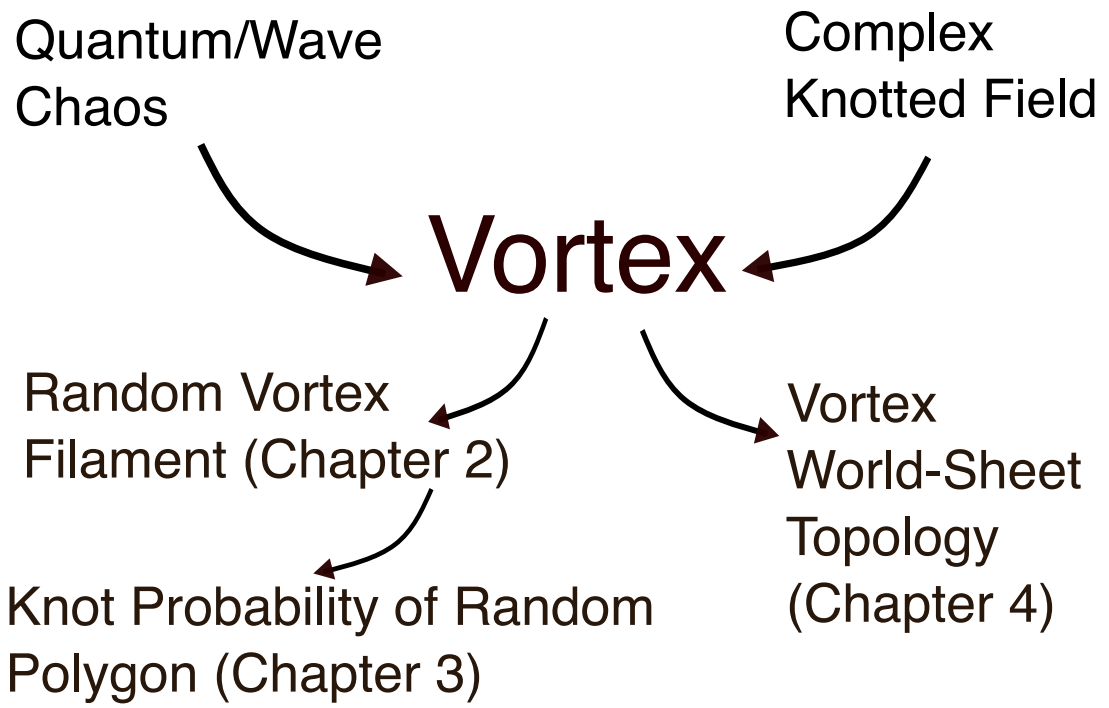

Figure 1.1: The outline of this thesis.

Shown in figure 1.1 is the outline of this thesis. Motivated by the studies of quantum and wave chaos, we search for the vortices which are random curves in space and space-time. In chapter two we study the statistical behaviour of these random vortex filaments. Then since these random vortex lines may be closed random walks, we study the knot probability of random polygons in chapter three, and find general equation for the knot probability in R^3, which may be applied to broad statistical science context. On the other hand, we also study vortices in designed field, beyond

random field. We construct complex knotted field that satisfies the d'Alembert equation in three-plus-one dimensional space-time, and study the topology of the vortex worldsheet which is what vortex swipes through in time.

1.2 Random Wave Model for Quantum Chaos and Wave Chaos

The famous "wave-particle duality" of light and in quantum physics extends the research from classical chaos to quantum chaos through studies on billiard systems. Imagine a region of certain shape of boundary in which particles are trapped and bounce back and forth like balls on a billiard table, then the dynamics of particles depend on the shape of the boundary of the billiard region. One famous example of billiard system is raised by Sinai [Sin70] that he proved particles in a square billiard with a circle boundary in its center that bounces back particles have trajectories that are ergodic and chaotic except measure zero. If a trajectory is ergodic then it will eventually covers the whole space in terms of passing through the neighbourhood of arbitrary point in the space as time advances, and if a trajectory is chaotic then another trajectory in its neighbourhood will diverge from it with a positive exponential rate.

As billiard systems are shown to be chaotic and ergodic, and since they are simple examples for chaos, following the spirit of "wave-particle duality" people study if there will be similar behaviour of chaos when transforming the consideration on chaotic dynamics of billiards into the consideration of waves as the counterpart, which clearly is like a wave trapped in a periodic boundary.

Two famous conjectures on quantum chaos were made by Berry and Tabor in

1977 [BT77] and later by Bohigas, Giannoni and Schmit in 1984 [BGS84]. Denote λ as the quantum energy eigenvalue and $P(S)$ as the level spacing distribution, which is the probability distribution of spacing S between two adjacent λ, λ_j and λ_{j+1}, then Berry and Tabor conjectured that for "generic" cases, meaning that excluding certain known counterexamples, if the corresponding system in classical dynamics is integrable, then the λ appear like independent random variable and $P(S)$ is like a Poisson process such that

$$P(S) = e^{-S} \tag{1.1}$$

Based on the result of Berry and Tabor, Bohigas, Giannoni and Schmit showed that if the corresponding system in classical dynamics is chaotic, particularly as they showed with the Sinai billiard, then $P(S)$ follows Gaussian orthogonal ensemble of random matrices, and thus enable the random matrix theory originally from nuclear physics to describe quantum energy levels. Particularly, there have been papers developed for the statistics of random waves such as [Ber78; BD00; MK88; BGS02; Den07] on statistical quantities like velocity, correlation and nodal density for various cases.

Even though later people realize that random wave model whose corresponding classical dynamics is chaotic does not exhibit chaos in terms of positive Lyapunov exponent in the wave counterpart because of the linearity of Schrödinger equation [Ber89], the random wave model nonetheless has link to a broad range of concepts in physics, such as in optics [ZG07; DAK18] where people study the optical vortices in random wave model, and in wave chaos for ocean acoustics [TB10], Helmholtz equation [LM10], especially the famous pioneering work by Longuet-Higgins [Lon57] where he resembled the sea water surface as an ensemble of long-crested wave as

$$\Psi(x, y, t) = \sum_n c_n \cos(u_n x + v_n y + \sigma_n t + \epsilon_n) \tag{1.2}$$

and study statistical properties such as energy spectrum and nodal density.

Quantum chaos and wave chaos are two terms not exactly equivalent but intersect and are closely related. While quantum chaos, apparently indicated by its name, focuses on systems whom and whose corresponding system in classical dynamics exhibit chaos, the studies in the field of wave chaos are not restricted to quantum mechanics. Despite of their different purpose and targeted physical scenario, both quantum and wave chaos may adapt similar mathematical expression for model construction by plane wave solution to the Helmholtz equation and its Gaussian random ensemble written as

$$\Psi(\boldsymbol{r}) = \sum_{\boldsymbol{n}} a_{\boldsymbol{n}} \exp(i\boldsymbol{k}_n \cdot \boldsymbol{r} + \chi_n) \tag{1.3}$$

A new insight to this random wave ensemble was formulated and verified by Mark Dennis and colleagues in 2008 [OHo+08] when they consider the vortex statistics globally rather than locally, and with classification from view of topology. Rather than local statistics of vortices such as velocity and vorticity, they view vortices in terms of their topology, such that whether a vortex is a loop or not, because loops differ from open strings by their topology. They study the length distribution of vortex loops and find a scaling relation indicating the self-similarity of the vortex loop soup. In chapter 2 we carry on this spirit of global statistics of vortices under topological view and push further to find more universal behaviours of vortices in random wave models. Yet before going further on details in chapter 2 we introduce more background knowledge essential to this thesis.

1.3 Knot Theory

As we will discuss in detail in chapter 2 and 3, vortices in random waves are found to be random walks and we propose and verify the general equation for knot probability in closed random walks. In order to discuss our result concretely in chapter 3 which

is the chapter for knot probability, and in chapter 4 which is the chapter for knotted vortex worldsheet, in this section we introduce necessary information of knot as the basis.

1.3.1 Knot Classification and Polynomial

Knots are embedding of topological circles in three-dimensional Euclidean space. The world we spatially live in is a three-dimensional Euclidean space, in which countless physical phenomena may appear as knots, such as polymers [WDL+98; RW11; OW07], vortices in extremely broad scenarios [Pis99] such as optics [OHo+08; ODP09; Den+10], liquid crystals [MA14], superfluid [SBR98; POB12; KBS01], normal fluid [Ric98; RSB99; Mag+13; KI13] and cosmic strings [VV84]. In a more extended perspective, open strings that are not topological circles may locally entangle and thus appear as knots localized in certain area. Therefore, knots are fundamental structure of the world we live in, and are key factors of low dimensional topology studies of physical phenomena.

An early attempt to classification of knots in done by Tait, inspired by Kelvin's conjecture that atoms are in fact knotted ether, which is later shown to be wrong, but inspired the work on knot theory and led Tait to the early work of making a knot table.

Lord Kelvin in 19^{th} century conjectured that the essence of atoms is in fact knotted ether, such as the hydrogen atom is one type of knotted ether while the oxygen atom is another type of knotted ether. Ether is a type of existence of a type of material that is imagined to be existing every where in the world and assumed to be the medium of light's propagating. Ether was thought to be of no colour or shape but people believed it to exist because it is not only a long-lived folklore but

also attributed to the propagation of light. However, as we later know, propagation of light, unlike the propagation of sound wave, does not require medium, and the famous experiment by Michelson and Morley on the light speed shows that there is no ether as medium of light's propagation. Furthermore, as discovered later and learned in today's middle school, atoms are electrons moving around nuclei made by protons and neutrons, and it is the electrons rather than the knot type of ether that determines the chemistry characteristics of different elements. Yet, these knowledge, while commonly studies today, was not known ay the time, so Lord Kelvin's conjecture gained its popularity at that time, and naturally inspired Tait to make a knot table for knots' classification, just like a periodic table for elements.

Since Tait, there have been mathematicians classifying knots based on the crossing number of knots, and such table grows up to knots of 16 crossings. As the number of crossing of knots increases, the diversity of knots of that crossing number increases drastically. There is only 1 type of knot of three crossings, 1 of four crossings, 2 of five crossings, 3 of six crossings, 7 of seven crossings, 21 of eight crossings, 49 of nine crossings, 165 of ten crossings, 552 of eleven crossing knots and so on. A classical work that is still widely used today is table made by Rolfsen for knots up to 10 crossings [Rol76]. Even though Rolfsen made a small mistake in his table that he misidentified a single ten-crossing knot as two different knots, so he thought there were 166 ten crossing knots but there are actually only 165 of them, his work is still classic and widely used today because for in many context 10 crossing knots are complicated enough.

In the figure 1.2, we draw diagrams for knots of three to seven crossings, including the unknot, which is labeled as 0_1. The diagrams are hand-drawn, in order to empathize the care that needed to be taken during the time that knot theory is developed by pen and paper, without modern help from the computer.

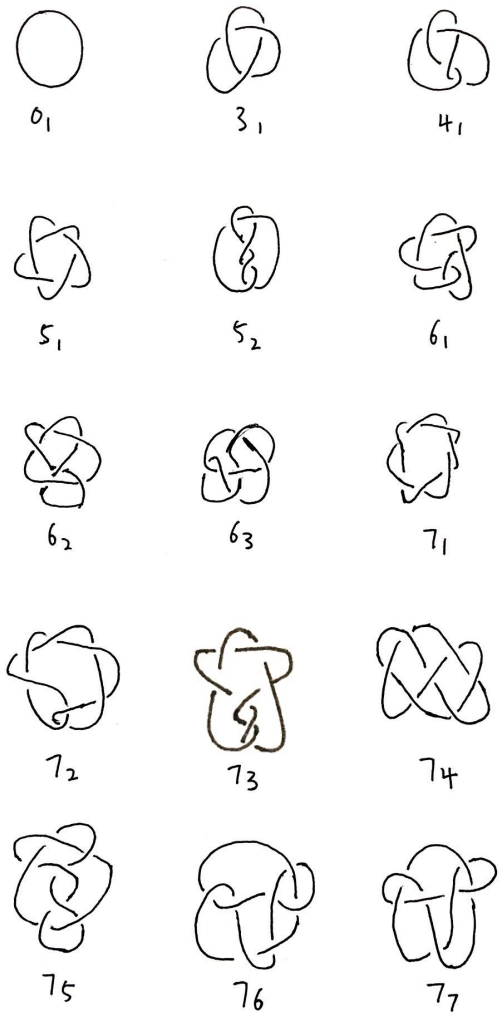

Figure 1.2: A table of diagrams for knots from 3 to 7 crossings including the unknot, which is labeled as 0_1. As will be discussed in later section, we concluded the probability of random knots mainly based on the probability data of these knots. Knots with crossing number higher than 7 happen to have less probability and therefore have less clear statistical behaviour.

Knot polynomials mark a great progress on knot theory because it enables algebraic representation of knots. People may write down a polynomial based on the skein relation of knots and therefore studies on knots are no longer limited within geometrical interpretations. An early and commonly used knot polynomial to dis-

tinguish knots is the Alexander polynomial, invented by James Waddell Alexander II [Ale28] and only became famous decades after. Then about half century later, Vaughan Jones introduced another polynomial, the Jones Polynomial [Jon87], named after himself. A difference between the Alexander polynomial and the Jones polynomial is that the Jones polynomial can distinguish the chirality of knots while the Alexander cannot. Yet since in our research we primarily care about the probability of knots disregarding the chirality of knots, we use Alexander polynomial rather than the Jones polynomial because the Alexander polynomial is simpler and computed in a higher speed.

Now we introduce how to compute the Alexander polynomial of a given knot [OW07]. We do it with specific examples. Firstly, let us consider the "figure-eight knot", knot 4_1, which is the second simplest knot, as shown in figure 1.3.

As shown in the figure, this knot has four crossing, and that is why it is called knot 4_1 because it has four crossings, and the sub-index 1 indicate that it is the first type of its kind, even though there is only one four-crossing knot. The four crossings in this knot are labeled by dark green number 1, 2, 3, 4. Naturally, these four crossings separate this knot into four pieces of curves represented by four numbers 1, 2, 3, 4 in red, and these "curves" are called "arcs". These four arcs are defined such that they start from one crossing as being the underlying arc, and stop at the next crossing as being the underlying arc again. It is worth noticing that an arc does not stop when it crosses a crossing as an over-crossing arc. Taking the second arc as an example: it starts from the second crossing as an underlying arc, then go through the third crossing without being stopped because it is an over-crossing arc, and finally it stops at the first crossing where it is the underlying arc again. It is important that when labeling the arcs, one may start from arbitrary place, but must continuously go through the knot following the curves by always

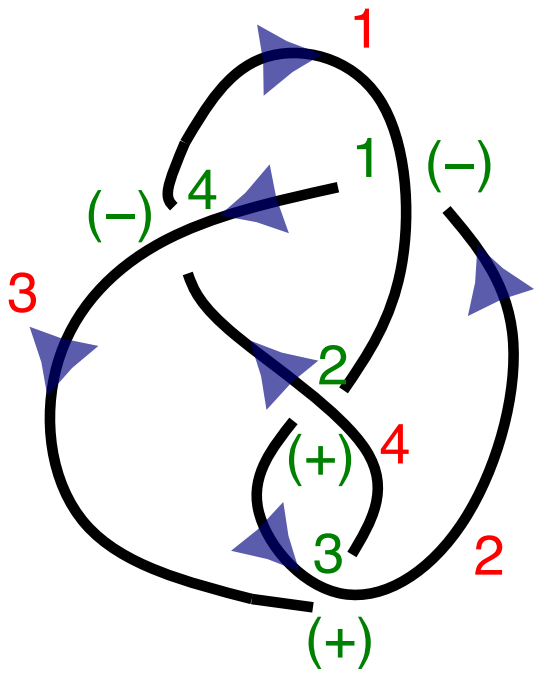

Figure 1.3: The diagram of the knot 4_1. Direction of the arcs are labeled by blue arrows. The red numbers 1 to 4 represent the arcs while the green numbers 1 to 4 represent the crossings. The plus and minus sign in parenthesis in green represent the sign of the crossing, which is determined by the right-handed rule.

keeping in one direction.

After labeling the crossings and arcs, one determines the sign of each crossing in the way shown in the figure 1.4.

The sign of crossing is determined by the right-hand rule. One may either take the over-crossing arc as the x-axis and underlying arc as the y-axis, and then the sign is positive if the z-axis direction is going out of the paper while is negative if the z-axis direction is going into the paper. Or equivalently one may take the underlying arc as the thumb finger and clenching the rest four fingers. The sign is positive if the sign of the over-crossing arc is the same to the direction of the rest four fingers and vice versa. After determining the sign of crossing, there are three values

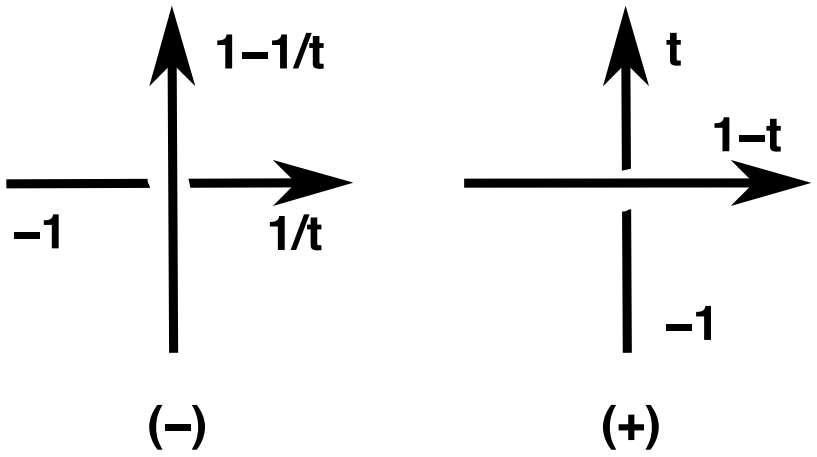

Figure 1.4: The positive and negative crossings whose sign is determined by the right-handed rule and there are three values assigned to the threes arcs connected to such crossing based on the sign of it.

assigned to the arcs as shown in the figure. For minus sign crossing, the assigned value for over-crossing arc, incoming underlying arc, and outgoing underlying arc is $1 - 1/t$, -1 and $1/t$. Meanwhile for the positive sign crossing, the three assigned values are $1 - t$, -1, and t.

Now after labeling the crossings and arcs and determining the sign of crossings we may write down a matrix based on them. For the knot 4_1 introduced above, the matrix to write down is

$$D(t) = \begin{vmatrix} 1-\frac{1}{t} & -1 & \frac{1}{t} & 0 \\ -1 & t & 0 & 1-t \\ 0 & 1-t & -1 & t \\ \frac{1}{t} & 0 & 1-\frac{1}{t} & -1 \end{vmatrix} \tag{1.4}$$

In the matrix $D(t)$, element (1,1) is $1 - 1/t$, because the first arc is an over-crossing arc at the first crossing, and since the first crossing is an negative crossing,

the assigned value to it is $1 - 1/t$. The element (1,2) is -1, because the second arc at the first crossing is an incoming arc, and the value for an incoming arc at a negative crossing is -1. The element (1,3) is $1/t$, because the third arc at the first crossing is an outgoing arc whose value is $1/t$. The element (1,4) is 0 because the fourth arc does not intersect with the first crossing and therefore is irrelevant. The element (2,1) is -1 because the first arc at the second crossing is an incoming arc at a positive crossing whose value is -1. Following this definition, we write down the matrix $D(t)$ where the element (i, j) is the value of the i^{th} arc at the j^{th} crossing. This definition gives us an n by n matrix such that n is the number of crossing of the knot. After obtaining $D(t)$, one compute any principle minor of $D(t)$ and multiplies or divide the result by power of t or $1-t$ to obtain a polynomial in t that has constant term, and this polynomial is our "Alexander polynomial". For knot 4_1, the Alexander polynomial is $t^2 - 3t + 1$.

We give another example for knot 3_1, as the figure 1.5 shows.

Following our previous definition that $D(i, j)$ is the value of i^{th} arc at the j^{th} crossing, the $D(t)$ of the knot 3_1 is

$$D(t) = \begin{vmatrix} -1 & \frac{1}{t} & 1 - \frac{1}{t} \\ \frac{1}{t} & 1 - \frac{1}{t} & -1 \\ 1 - \frac{1}{t} & -1 & \frac{1}{t} \end{vmatrix} \tag{1.5}$$

The first arc at the first crossing is an incoming arc at a minus crossing, therefore $D(1, 1)$ has value of -1. The second arc and the third arc at the first crossing are the outgoing and the over-crossing arc, so $D(1, 2) = 1/t$ and $D(1, 3) = 1 - 1/t$. Following the definition, we write down $D(t)$ and compute its principle minor. We may, for example, consider the 2 by 2 matrix at the bottom left, whose determinant is computed to be $((1-1/t)\cdot 1/t)-1 = 1/t-1/t^2-1$. Then we multiplies

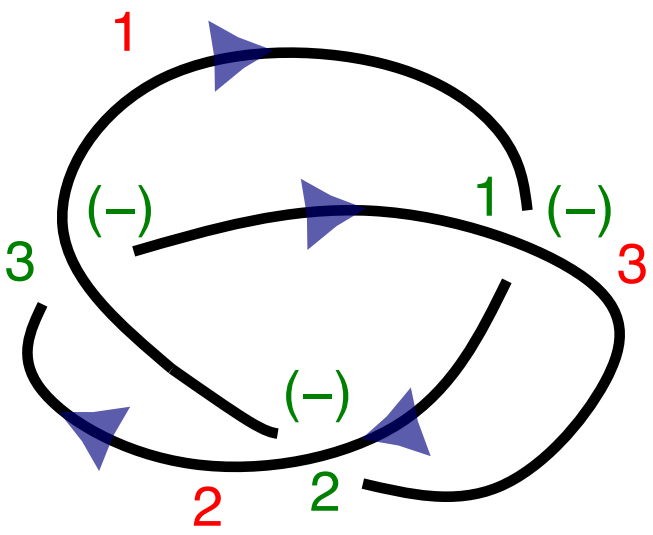

Figure 1.5: The diagram of the knot 3_1. Direction of the arcs are labeled by blue arrows. The red numbers 1 to 3 represent the arcs while the green numbers 1 to 3 represent the crossings. The plus and minus sign in parenthesis in green represent the sign of the crossing, which is determined by the right-handed rule.

it by the second power of t, which is t^2, and obtain the Alexander polynomial to be $t^2 - t + 1$.

There are other equivalent ways of evaluating the Alexander polynomial, such as besides assigning value -1, t, $1 - 1/t$, one could also assign value $-t$, 1, t, -1 for arcs that are left arc before crossing, right arc before crossing, left arc after crossing and right arc after crossing. These different method will give the same result [OW07] as to compute the principle minor of $D(t)$ and let us obtain the Alexander polynomial of a given knot.

Compared to the method of calculating the Alexander polynomial, the Jones polynomial is similar in the way that it is also based on the crossings and skein rela-

tion of knots, but the way of computing the Jones polynomial is more complicated than the Alexander polynomial. The skein relation is the relation of two curves that whether they are right-handed crossed or left-handed crossed or not crossed, as shown in the figure 1.6.

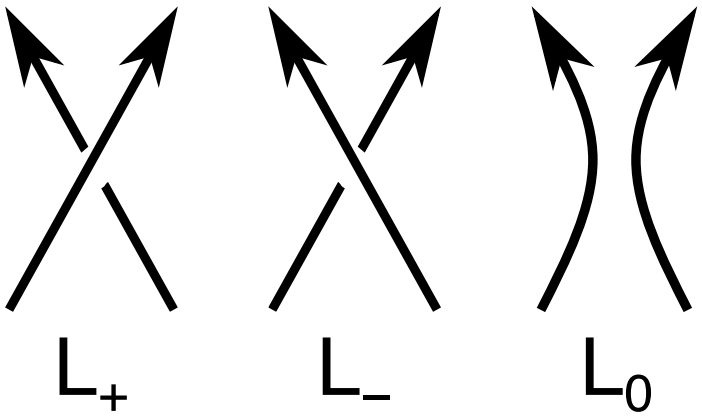

Figure 1.6: The diagram of the skein relation. There are three types of skein relations L_0, L_+ and L_- as shown in the figure.

The basic idea of calculating the Jones polynomial is to operate changes on the skein relations and step by step until the given knot becomes unknotted. During such operations, one writes down polynomials with multiplications and divisions based on how skein relation is changed each step, and finally as the given knot is changed to an unknot through steps, the polynomials that multiplied through is the Jones polynomial. In a more intuitive description, finding the Jones polynomial is equivalently decomposing the knot and finding the corresponding accumulated changes made during such decomposition.

Since the Alexander polynomial is a faster computing algorithm and is valid enough for our research purpose, which is to study the probability of random knots, we use the Alexander polynomial to algebraically represent knots in our research. Admittedly, the Alexander polynomial is not perfect in the sense that for knots with

higher crossing numbers, it happens that two knots with high crossing number may happen to have the same Alexander polynomial while they are different knots. However, it does not brings trouble to our research because the Alexander polynomial is accurate for all knots with crossing number smaller or equal to 7, and majority of 8 and 9 crossing knots. As we will show in our later research, it is sufficient for us to study and conclude general principles of knot probability.

1.3.2 Previous Knowledge on Knot Probability

Previous studies on the knot probability are both theoretical and numerical. A notable theoretical result on knot probability is done by Hammersley in 1961 on lattice model [Ham61]. Denote p_n to be the number of n-edge polygon, Hammersley showed that

$$0 < \lim_{n\to\infty} n^{-1} \log P_n \equiv \kappa < \infty \tag{1.6}$$

Which equivalently means that

$$P_n = e^{\kappa n + o(n)} \tag{1.7}$$

where κ is a constant called connected constant of the lattice and for simple cubic lattice the range of κ is between log3 and log5. Here the term $o(n)$ is different from $O(n)$. A function $f(n)$ is $o(n)$ if $lim_{n\to\infty} f(n)/n = 0$, and for example $\log(n)$ is $o(n)$, while $f(n)$ is $O(n)$ if $f(n) \leq An$ for some positive constant A and large enough n. Hammersley showed that the number of $n-$ edge polygon has same growth rate to self-avoiding random walks as n increases.

Based on Hammersley's work, Sumners and Whittington in 1988 [SW88] pushed his result further and showed that

$$\lim_{n\to\infty} n^{-1} \log P_n^0 = \kappa_0 \tag{1.8}$$

where P_n^0 is the probability of the unknot 0_1 of n-edge polygon, and this equivalently leads to

$$P_n^0 = e^{-(\kappa-\kappa_0)n+o(n)} = e^{-a_0 n+o(n)} \tag{1.9}$$

for some positive a_0

This means that the probability of the random polygon unknot decreases exponentially to zero as its edge number increases, or equivalently saying that a random polygon is almost certain knotted as n goes to infinity, as one would intuitively anticipate and appreciate, which is also called as the "Frisch-Wasserman-Delbruck conjecture" [OW07].

However, it is important to realize that, the above theoretical result is built on the lattice model, which is $\mathbb{Z}^3$, while our real world is $\mathbb{R}^3$. All those knotted light, polymers and vortices exists in our $\mathbb{R}^3$ world, and mathematically theorem in $\mathbb{Z}^3$ and $\mathbb{R}^3$ are not necessarily mutually adaptive. Therefore, it is not sufficient to push forward the theoretical result from $\mathbb{Z}^3$ to $\mathbb{R}^3$, so the probability of knot in $\mathbb{R}^3$ remains unknown, even though it is reasonable to believe that such exponential term from $\mathbb{Z}^3$ should also exist in $\mathbb{R}^3$. However, as we find out, an solely exponential term is not sufficient to describe the knot probability, which turns out to be in the form of an asymptotic expansion formula. Even though, theoretical works done by Hammersley, Sumners, Whittington and other researchers [Dia95] pushed forward the knowledge of knot probability.

Besides theoretical work, there have also been numerical studies on knot probability, such as a series of works done by Deguchi and colleagues [DT94; DT97; UD17] through numerical simulations. Deguchi studies the probability of some simple prime and composite knots because the simpler the knots are, the higher probability they have, and therefore have clearer statistical pattern. This work of Deguchi, like many others, is based on Gaussian random polygons. Gaussian random poly-

gons are random polygons whose edge length distribution obeys Gaussian normal distribution. Deguchi's work confirms that the knot probability obeys the form of asymptotic expansion, but due to limited computation capacity, he did not realize that in fact the probability of the unknot is also in the form of asymptotic expansion rather than a simple power law decay, as we will show in later chapter. Deguchi also did not include the correction term into the knot probability formula, a possible reason is that he did not have numerical data result for many knots, and even limited accuracy for presented knots. On contrary, our simulation, with exceeding numerical quality, reveals the role of correction terms in the knot probability formula. Although Deguchi's numerical work is limited and thus stops him from further conclusion, admittedly his work is on the right track and paves the road for later research.

1.3.3 Helicity Conservation and Knotted Field

Knots are important to the study of fields such as quantum and fluid field because not only the vortices may form knots but also the essence of the field is closely related to knot theory. The study of vortex is a key to the nature of fluid field because vortices are the zeros and the topological defect of the field, and thus it is a tool to categorize the field. The knotted vortex lines is closely related to the helicity of the field, which is an essential concept to topological fluid dynamics.

In fluid dynamics, the helicity is defined as the integral of the dot product of the velocity $\boldsymbol{u}$ and the curl of $\boldsymbol{u}$ over the spatial volume V:

$$H = \int_V \boldsymbol{u} \cdot (\nabla \times \boldsymbol{u}) dR \tag{1.10}$$

One may write it in an equivalent form as

$$H = \int_V \boldsymbol{A} \cdot \boldsymbol{B} dR \tag{1.11}$$

where $\boldsymbol{B} = \nabla \times \boldsymbol{A}$ so that it is consistent to the definition of helicity in a broader sense. For example, for the magnetic helicity, $\boldsymbol{B}$ is the magnetic field while $\boldsymbol{A}$ is the potential. However $\boldsymbol{A}$ and $\boldsymbol{B}$ are not limited to the magnetic field definition, they can be more basic vector fields that represent different physical quantities. It is straightforward to see that the helicity is independent to the gauge of $\boldsymbol{A}$.

Moffatt and Ricca [MR92] considered the helicity in fluid dynamics and showed that its conservation is in fact equivalent to the Călugăreanu theorem [Căl59], which states that the linking number is equal to the sum of twist and writhe of a curve, and is an invariant quantity. Equivalently it means that the helicity is an invariant quantity under conditions. The conservation of helicity is the fourth fundamental conservation law after the conservation of energy, momentum, and angular momentum, and it is a fundamental approach to various fields such as turbulence [MT92; Zhu18] and electromagnetic field [BF84; Alp+18; TR96], especially after the works by Moffatt and Ricca revealing the conservation of helicity and that the geometrical reflection of it is the Călugăreanu theorem.

The Călugăreanu theorem [Căl61] states that the linking number n of a curve C is equivalent to the sum of the writhe W, the total normalized torsion T, and the number of rotation around C in integer N

$$n = W + T + N \tag{1.12}$$

Or equivalently,

$$n = W + TW \tag{1.13}$$

where $TW = T + N$ is the Twist of the ribbon curve.

The linking number is a conserved quantity under conditions (such as no topology change takes place) because the increase or decrease of the twist or writhe will induce the change of the other quantity to balance out so that the sum of the

twist and the writhe, the linking number n, is conserved.

Moffatt and Ricca in 1992 [MR92] showed that

$$H = n\Phi^2 = (W + T + N)\Phi^2 \tag{1.14}$$

Where Φ is the flux along the vortex tube in the fluid field. This means that the geometrical interpretation of the helicity is the linking number of the corresponding vortex knot. Comparing to the other three conservation laws of energy, momentum, and angular momentum whose geometrical interpretation is the invariance under symmetry transformation in time, linear movement and rotation, the conservation of helicity has its geometrical interpretation as the invariance of linking number as long as there is no topology change.

Besides helicity, the nature of the field theory links to the knot theory fundamentally in another perspective, such as the revealing work by Edward Witten [Wit89] and Xin Liu and Renzo Ricca [LR12] showing the straight connection between the Quantum field theory and fluid dynamics to the Jones polynomial.

Witten's work [Wit89] starts from the Chern-Simons 3-form, which is a quantity in Schwarz type of topological quantum field theory (TQFT), which is independent to choice of metrics. Consider a three-manifold M, compact simple gauge group G and connection A, then the integral of Chern-Simons 3-form, which is proportional to the Chern-Simons action, is

$$\begin{aligned} S &= \frac{k}{4\pi}\int_M Tr(A \wedge dA + \frac{2}{3}A \wedge A \wedge A) \\ &= \frac{k}{8\pi}\int_M \epsilon^{ijk} Tr(A_i(\partial_j A_k - \partial_k A_j) + \frac{2}{3}A_i[A_j, A_k]) \end{aligned} \tag{1.15}$$

where the curvature F is

$$F = dA + A \wedge A \tag{1.16}$$

and the least-action principle, here in terms of the field curvature, leads to the

dynamics

$$\frac{\delta S}{\delta A} = \frac{k}{2\pi} F = 0 \tag{1.17}$$

It is worth pointing out that, for abelian gauge field, the later half term in the Lagrangian is cancelled out due to symmetry and thus simplifies the equation to be

$$S = \frac{k}{8\pi} \int_M \epsilon^{ijk} A_i \partial_j A_k \tag{1.18}$$

It is truly amazing that this Lagrangian is equivalent to the helicity as we introduced above. Since as discussed earlier in the section, the geometrical reflection of the helicity is the linking number of a curve, therefore the equivalence between the Chern-Simons action in abelian gauge field and the helicity suggests that the Chern-Simons theory provides a natural framework for the study of knotted nature of quantum fields.

In this context, the Wilson loop operator around a circle C is defined as

$$W_C = Tr(Pe^{i \oint_C A_i dx^i}) \tag{1.19}$$

where P is the path-ordering operator. It is an integral over a closed circle, but of course such circle represents anything topologically equivalent to an S^1, either knotted or not, and it has the gauge form

$$Pe^{i \oint_C A_i dx^i} \to g(x) Pe^{i \oint_C A_i dx^i} g^{-1}(x) \tag{1.20}$$

From here, Witten and Xin Liu used similar but not exactly the same method to connect the essence of quantum and fluid dynamics to knot polynomials. The work of Xin Liu and Renzo Ricca is based on the helicity, which as him acknowledged inspired from the abelian Chern-Simons 3-form. Liu and Ricca started from helicity interpreted by Kauffman bracket for un-oriented loops to derive skein relations, and after that they included the orientation and reduced previous skein relation to the Jones polynomial. We do not include much of the deduction detail by Witten and

Liu and Ricca, but as the result they connected the expectation value of the Wilson loop operator and the helicity to the Jones polynomial by writing out equation that is in the same form to the skein relation of Jones polynomial, which is

$$(t^{1/2} - t^{-1/2})V(L_0) = t^{-1}V(L_+) - tV(L_-) \tag{1.21}$$

As the L_0, L_+ and L_- are shown in the figure 1.6

1.3.4 Designing Knot in Complex Field

The vortices in complex field may be designed into knots. The vortices in 3D space are either lines or loops depending on knotted or not, while in 3+1 space-time they gain an extra dimension and become vortex sheets. In order to distinguish such vortex sheet from vortex sheet in 3D space, we may name it vortex worldsheet for avoidance of confusion. Before further investigating the vortex world sheet in 3+1 space-time, it is necessary to firstly clarify the design of knots in 3D space. In particular, we begin by showing how to design a certain knot type in complex field.

In 1928, Brauner [Bra28] invented a method, later popularised by Milnor [Mil16], of creating a complex scalar field with (torus) knotted vortex lines. The method is to design a three-dimensional complex field on (x, y, z) whose vortex is knotted as designed. There are different ways of constructing field whose vortex is knotted, such as from toroidal expression of torus knot, but in the thesis we use the construction invented by Brauner so that we may construct knots beyond torus knots, even though different constructions may be transformed to each other for some knot types. Such a field is constructed as an algebraic function of the two supporting complex field functions $u = u(x, y, z)$, $v = v(x, y, z)$ [Den+10] defined as

$$u = \frac{x^2 + y^2 + z^2 - 1 + 2iz}{x^2 + y^2 + z^2 + 1} \tag{1.22}$$

$$v = \frac{2(x + iy)}{x^2 + y^2 + z^2 + 1} \tag{1.23}$$

as polynomials in terms of u and v will yield different complex field whose vortices form into various knot types, as will be shown in the following. As shown by the algebraic of u and v, u is symmetric on planar direction while v is symmetric on vertical direction. Intuitively, the field of u and v are shown by figure 1.7, where we plot the argument of the complex function. By inspection, it is easy to see that u has a circular vortex in the $x - y$ plane of radius 1, and v has a vortex line up the z axis.

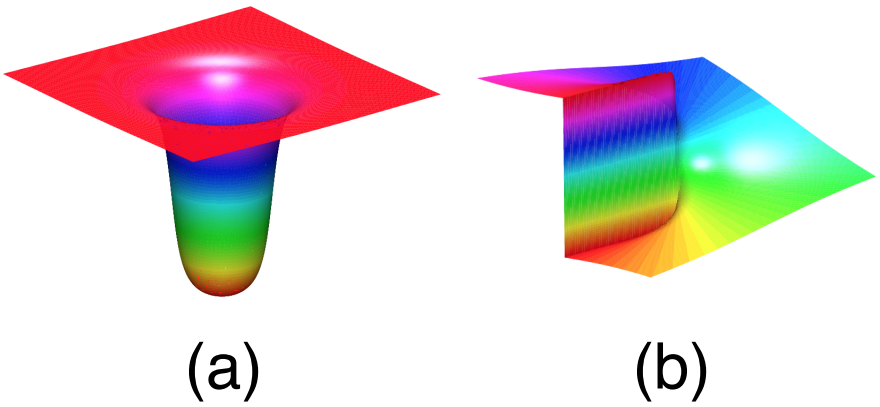

Figure 1.7: The field surface plot for u and v on $x - y$ plane at $z = 0$. This is plotting the complex argument and showing in HSV color gradient. Subplot (a) is for u and (b) is for v.

The color gradient clearly shows the change of the phase, and a net phase change of 2π, appearing as the color gradient going through the HSV spectrum, defines a phase vortex which is explicitly stated in equation (2.7) and (2.8). Then, the phase vortex of the field u and v is in figure 1.8

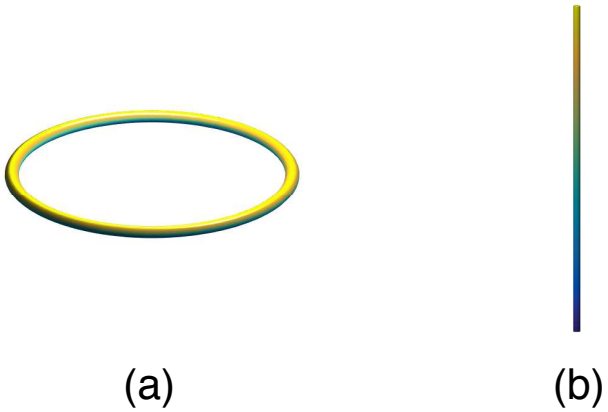

Figure 1.8: The phase vortex in u and v shown in subplot (a) and (b). The vortex in u is a loop while in v is a straight line at the origin.

The vortex in u is a loop while in v is a straight line at the origin. The loop winds around the origin while the straight line go through it, and as they are in complement to each other, together they may be used as primary tools to design vortices of more complicated shape. For any point in 3D space (x, y, z), its coordinate may be written as $R + z$ where $R = \sqrt{x^2 + y^2}$, as a combination of polar coordinate and height, which is exactly shown by the vortex in u and v. Meanwhile, as the u and v together form a complete coordinate system, there is $|u^2| + |v^2| = 1$.

It is shown in [Bra28] that a field of $u^q - v^p$ has vortex in terms of (p, q)-torus knot, which is a knot formed by winding a loop p time through the hole of the torus and q times around the torus, as in figure 1.8 that the vortex in v penetrate through the origin while the vortex in u winds around the origin. (The expression in some papers have reversed expression for u and v to the text here. Different papers have been using different u and v such that u in some paper is v in the others, and vice versa. However, the two terms u and v together always refer to the same expression. The only difference is the just the notation.)

The simplest example of which is the trefoil knot, which is the knot 3_1 in the knot table and is a (3, 2) torus knot, meaning that it is equivalently dwelling on the surface of a torus and goes 3 times through the hole of the torus and 2 times around it, as shown in figure 1.9. Therefore, the field whose vortex is a trefoil knot is

$$\Psi = u^2 - v^3 \tag{1.24}$$

$$= \frac{(x^2+y^2+z^2+2iz-1)^2}{(x^2+y^2+z^2+1)^2} - \frac{(2x+2iy)^3}{(x^2+y^2+z^2+1)^3} \tag{1.25}$$

Figure 1.9: The trefoil knot, equivalently in the name knot 3_1 or (3, 2) torus knot, obtained as the vortex of the field $\Psi = u^2 - v^3$.

Two other examples of constructing the torus knot is knot 5_1 and knot 8_{19} shown in figure 1.10, which are of (p, q) value (5, 2) and (4, 3), such that $\Psi = u^2 - v^5$ and $\Psi = u^3 - v^4$. The knot 5_1 is the second simplest torus knot after the trefoil knot, and both of them have apparent look of lines winding around the surface of a torus. The knot 8_{19} is the first non-alternating knot, and has relatively simpler

structure compared to other 8 crossing knots. The uniqueness of the knot 8_{19} is also discussed in the chapter of knot probability, such as its high occurrence probability.

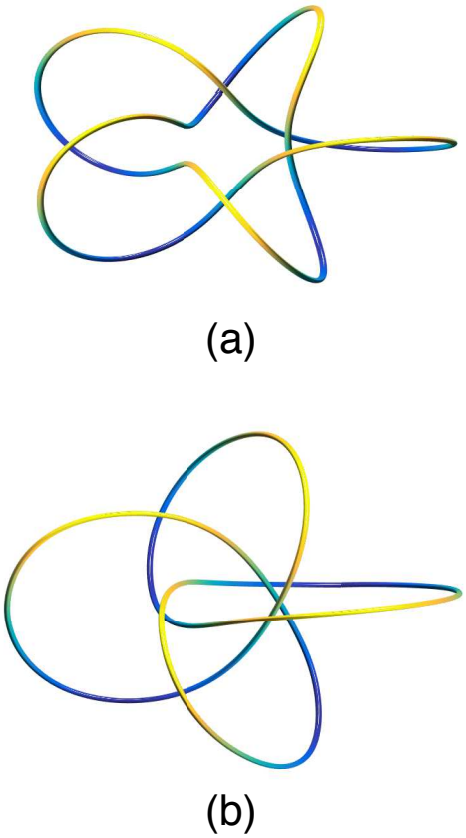

Figure 1.10: The knot 5_1 in subplot (a) and knot 8_{19} in subplot (b) are two torus knots with (p, q) of (5, 2) and (4, 3), so they come from $\Psi = u^2 - v^5$ and $\Psi = u^3 - v^4$

While the field $u^q - v^p$ has vortex of (p, q) torus knot, there are constructions for other geometries based on u and v as well, such as for the figure-eight knot, also known as the knot 4_1, which is not a torus knot. The field that has vortex to be a figure-eight knot is [Den+10]

$$\Psi = 64u^3 - 12u(3 + 2(v^2 - \bar{v}^2)) - 14(v^2 + \bar{v}^2) - (v^4 - \bar{v}^4) \tag{1.26}$$

where $\bar{v}$ is the complex conjugate of v. The vortex of such field is shown in figure 1.11

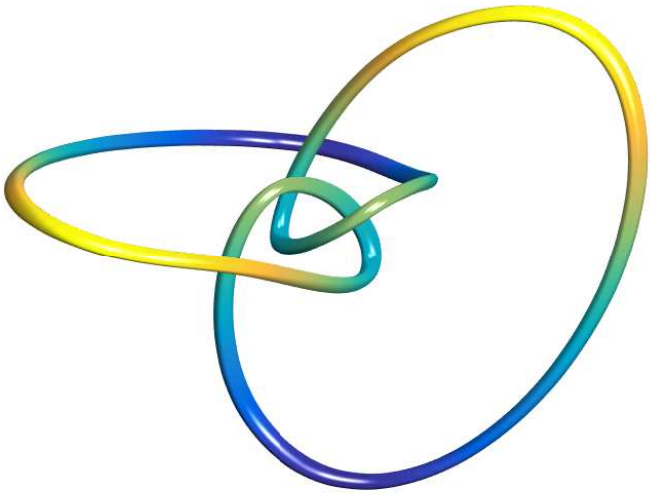

Figure 1.11: The figure-eight knot, equivalently in the name knot 4_1, obtained as the vortex of the field $\Psi = 64u^3 - 12u(3 + 2(v^2 - \bar{v}^2)) - 14(v^2 + \bar{v}^2) - (v^4 - \bar{v}^4)$.

The knots designed in such way may also have a tunable helicity as shown by Kedia et al [Ked+16], such that the helicity of certain knot type designed based on u, v may be changed by introducing an extra term such as u^n for some integer n and such n determines the degree of helicity revised. We will rely on the techniques of constructing knots in complex field in chapter 4, but the tunable helicity is not involved.

1.4 Necessary Topological Knowledge

Topology has particularly been an important tool for analyzing complicated dynamics because the idea of topology leads to consistence and robustness against

continuous changes such as small perturbations away from critical point. In the idea of topology, people focus on quantities such as homology which intuitively is the holes in the topology space, because they are invariant even when the geometry is changed: imagine a loop is deformed and local geometry such as curvatures certainly changes, but the homology of it is invariant as long as the loop is not cut or merged.

In chapter 2 we classify the vortices according to the homology, such that vortices are either open strings or closed loops, because closed loops are homeomorphic to S^1 circles. In chapter 4 our analysis to the vortex worldsheet, which is a surface in 3+1 dimensional space, also rely on the concept of homology. Therefore, it is necessary to introduce homology in this section. Besides homology, we also introduce the Poincare-Hopf theorem, also known as the Poincare index theorem, which links the topology of the manifold and the vector field on its surface, as it is necessary for our analysis in chapter 4.

1.4.1 Homology and Betti Number

The rigorous definition of homology group H on a topology space X is [Hat02]

$$H_n(X) := \ker(\partial_n)/\mathrm{im}(\partial_{n+1}) \tag{1.27}$$

where $H_n(X)$ denotes the n^{th} dimensional homology group on space x, and $\ker(\partial_n)$ is called cycles, and $\mathrm{im}(\partial_{n+1})$ is called boundaries. ∂_n is the boundary operator defined on chain complex C_n such that

$$C_{n+1} \xrightarrow{\partial_{n+1}} C_n \xrightarrow{\partial_n} C_{n-1}...C_1 \xrightarrow{\partial_1} C_0 \xrightarrow{\partial_0} 0 \tag{1.28}$$

where chain complex is a series of abelian groups that are connected by homomorphisms, which here specifically is our boundary operator ∂_i that satisfies

$$\partial_n \partial_{n+1} = 0 \tag{1.29}$$

Which is a famous conclusion in mathematics and physics that "the boundary of a boundary is none".

In detail, the boundary operator ∂_n of a simplex $\sigma = (v_0, ..., v_k)$, which is directly a set of elemental components (such as vertices and faces) and higher dimensional constitutes built from which, is defined as

$$\partial_n(\sigma) = \sum_i (-1)^i \sigma | [v_0, ..., \hat{v_i}, ..., v_n] \tag{1.30}$$

where $\hat{v_i}$ refers to v_i being removed. However, in order not to go into too much detail of this, we may sufficiently accept homologies simply as "holes" in the space, and n^{th} dimensional homology in topology is equivalent to an n-dimensional "hole" in topology, which also sometimes referred as the "Betti number" such that if

$$\text{Betti}_n = m \tag{1.31}$$

then there the number of n^{th} dimensional homology is m on certain manifold.

For example, in figure 1.12, $\text{Betti}_1 = 1$ because there is a one-dimensional hole bounded by the three edges of the triangle, according to the definition of the homology group in equation (1.27) and the vertices are labeled as v_0, v_1, v_2 and edges defined in equation (1.30).

1.4.2 The Poincare-Hopf Theorem

A fundamental theorem in topology is the Poincare-Hopf theorem (calling PH theorem in the following), also called the Poincare index theorem, which connects the topology of surfaces and the vector field on it [Lee13]. The PH theorem states that suppose on a compact differentiable manifold M there exists vector field v, and the direction of v at the boundary is all pointing in the same direction (all inwards or all outwards), then there is an equivalence between the sum of index values of zeros

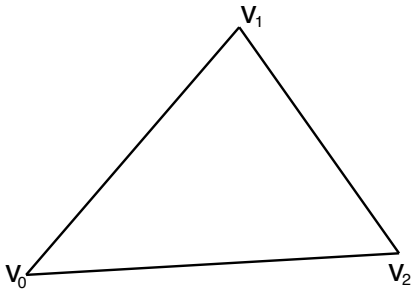

Figure 1.12: A triangle which has $\text{Betti}_1 = 1$.

of the vector field and the Euler characteristic of the manifold. Mathematically it states

$$\sum_i \text{index}_{x_i}(v) = (-1)^n \chi(M) \tag{1.32}$$

where χ is the Euler characteristic, and n is even if the v is everywhere pointing outward at the boundary while odd if v is everywhere pointing inwards at the boundary.

The index of a critical point describes the behaviour of vector field in its neighborhood. The index of a sink and a source is $+1$ while the index of a saddle point is $(-1)^k$ where k is the number of dimension that the vector field is shrinking, meaning a negative eigenvector of the Hessian matrix. The sink of a vector field is a local minimum where points in the neighborhood tend to while the source is a local maximum where points in the neighborhood move away from. While in three dimensional vector field the saddle point may have index either -1 or 1 depending on the eigenvector of Hessian matrix, such that if it is $(-1, -1, 1)$ then the index is $-1 \cdot -1 \cdot 1 = 1$ while if it is $(-1, 1, 1)$ then the index is $-1 \cdot 1 \cdot 1 = -1$, in two dimensional vector field the saddle point always have index value of -1 because $-1 \cdot 1 = -1$.

The Euler characteristic is a topological invariant describing the topology of a manifold. The definition of Euler characteristic χ is

$$\chi = V - E + F \tag{1.33}$$

where V, E, F are the number of vertices, edges, and faces. The Euler characteristic is a topological invariant such that objects that are topologically equivalent have same Euler characteristic. The Euler characteristic of a sphere is 2, and of a cube or tetrahedron or any convex polyhedron is always 2. The Euler characteristic of solid objects is 1, and of a circle or torus is 0. When one changes the topology of a manifold, by adding a handle the Euler characteristic decreases by 2, and by puncturing a hole the Euler characteristic decreases by 1. For example, a solid disk has $\chi = 1$, and if one punctures a hole in it, then it becomes a circle that $\chi = 1$; a torus has $\chi = 0$ and by adding a handle it becomes a double torus that $\chi = -2$, and furthermore a triple torus has $\chi = -4$.

Chapter Two

Universal Statistics of Spatial and Spatial-Temporal Wave Chaos Vortices

In this chapter we find universal scaling relation of the length distribution of vortex loops and open strings independent to the model specification of the random wave model, such that the universality holds between purely spatial and spatial-temporal random wave models. We show details of generating the random waves, finding the vortices, and analyzing the vortices.

2.1 Methodology and Simulation

As introduced in the chapter of introduction, there has been a series of research on quantum chaos since Berry [BT77] and Bohigas [BGS84], and the model they use is the random wave model, which was later also used for optics such as [Den+10]. The random wave model is an ensemble of plane waves as solution to the Helmholtz

equation with Gaussian random amplitude written as

$$\Psi(\boldsymbol{r}) = \sum_{\boldsymbol{k}} a_{\boldsymbol{k}} \exp(i\boldsymbol{k} \cdot \boldsymbol{r}) \tag{2.1}$$

where $\boldsymbol{r} = (x, y, z)$, $\boldsymbol{k}$ is the angular wave number, and $a_{\boldsymbol{k}}$ is the random amplitude.

This random wave model is dependent on three spatial dimension, where vortices in the space behave like Brownian random walks. We are curious what happens to the vortices when the set-up changes from 3D to 2+1D, such as whether the vortices will still behave like Brownian random walks. Further, studying waves in 2+1D is not just a question out curiosity, but it has motivation from a broad range of application, such as wave chaos for ocean surface wave [Lon57] and optics [DAK18].

Therefore, we extend from three-dimensional wave chaos to time-dependent wave chaos of two spatial dimension

$$\Psi(\boldsymbol{r}, t) = \sum_{\boldsymbol{k}} a_{\boldsymbol{k}} \exp(i(\boldsymbol{k} \cdot \boldsymbol{r} - \omega t)) \tag{2.2}$$

Specifically, we consider the model of a periodic boundary condition which explicitly leads to

$$\Psi(x, y, t) = \sum_{m,n=-N}^{N} a_{\boldsymbol{k}} \exp(2\pi i[(mx + ny)/L_0 - kt/T_0]) \tag{2.3}$$

where the amplitude is chosen to be Gaussian power spectrum of controllable width.

For the simulation of this 2+1 random wave model, it is important to choose the proper time scale T_0, length scale L_0, and the length of the unit grid dT and dL. We set $dT = dL$ so that only the T_0 and L_0 will be adjusted for vortex density. We set the time and length scale in the way such that the phase vortex density on spatial and temporal direction is isotropic, such that the total number of vortex points on spatial dimension N_L divided by L_0 is equal to the total number of vortex points on temporal dimension N_T divided by T_0, and thus gives a "normalized" scaling for later

investigation on the statistical properties of the random vortex, where for a given vortex point in 2+1 space, it has equal probability of moving on each dimension, at least in a global perspective. The dispersion relation between m, n and k are chosen to be representing three different relation: $k = \sqrt{m^2 + n^2}$ which is of d'Alembert, $k = m^2 + n^2$ which is of Schrödinger, and $k = \sqrt{m^2 + n^2 + g}$ which is of Klein-Gordon where g is the mass, so together with the 3D Helmholtz equation there are in total four sets of random waves to be compared.

N determines the number of random waves being superposed, therefore the large N is, the more random the wave ensemble is, as shown in figure 2.1. In same region, when N is larger, there are more random waves superposed, and thus bring greater randomness and unpredictability to the system.

It is beneficial to clarify the difference between "chaos" and "randomness" in this scenario, as they both leads to unpredictability. The word "chaos" classically refers to the unpredictability in the dynamical evolution, that consider an initial point in the dynamical system, as time advances the neighbourhood of its trajectory undergoes exponential divergence. Such exponential rate is called Lyapunov exponent and positive Lyapunov exponent indicates chaos in classical dynamics. Since points in the neighbourhood of trajectories diverge in an exponential rate, a little uncertainty in the measurement from the observer may leads to difference that grows exponentially in time, and that is the unpredictability in the system. However, classical chaotic systems are deterministic, meaning that had the system got a chance to evolve again, everything will faithfully and accurately reply: there is no "randomness" required (even though allowed) in classical chaos, and the "unpredictability" is attributed to the ignorance of the observer rather than the nature of the system. However, wave chaos and quantum chaos or quantum chaology is different. Truly, there is unpredictability in random wave model, however, such unpredictabil-

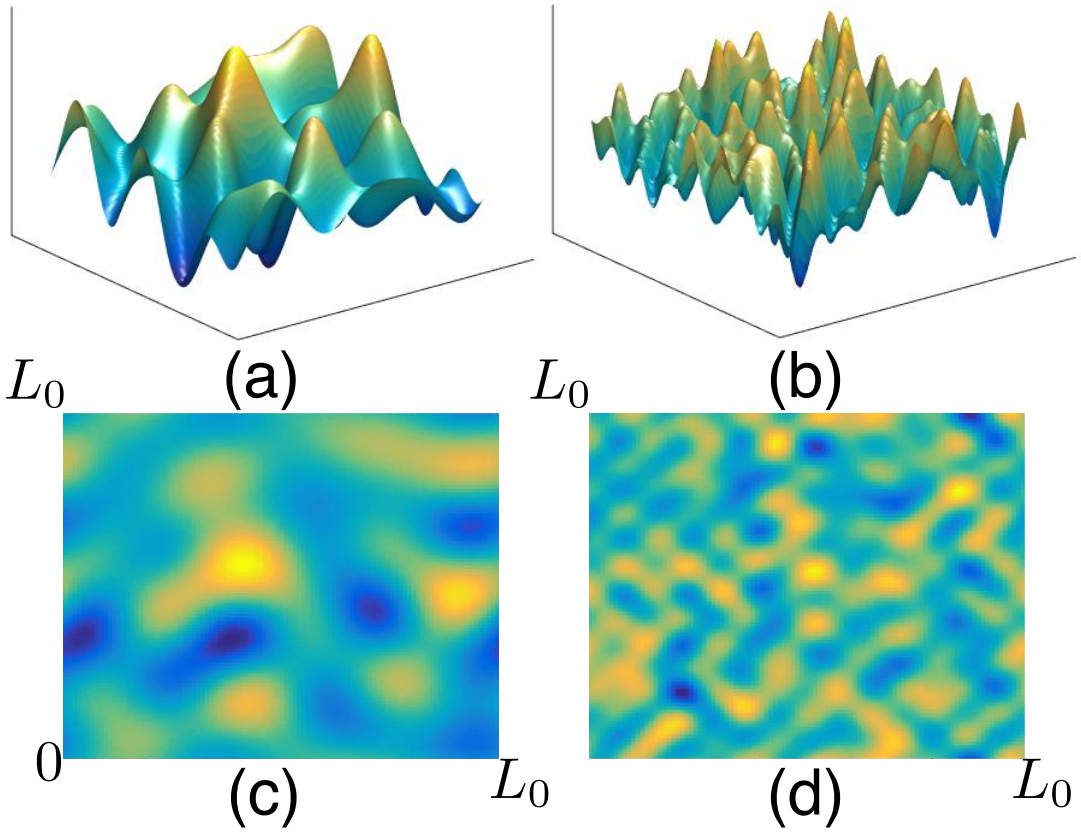

Figure 2.1: A comparison between random wave model of small and large N of equation (2.3). All subplots are on the $x-y$ plane plotting the real part of the wave equation. Subplot (a) and (c) are of $N = 3$ while (b) and (d) are of $N = 7$. Subplot (c) and (d) are of top view. This is a straightforward illustration on random wave ensemble of different number of waves.

ity comes from the randomness of the system: in a random wave ensemble, there could be randomness in amplitude or phase of the superposed waves. While classical chaos is deterministic, wave chaos or quantum chaos have randomness in their nature. Furthermore, classical chaos comes from the nonlinearity in the system, while the random wave model is a superposition of linear waves. These differences in nature of systems are worth for clarification, like Berry argues [Ber89] that "quantum

chaos" should be renamed as "quantum chaology", because the definition of classical chaos requires a positive Lyapunov exponent, leading to the unpredictability to the future, or equivalently exponential sensitivity to the initial condition, while such positive Lyapunov exponent does not exists in random wave model due to the linearity of Schrödinger's equation. Otherwise besides Schrödinger's equation, there is also Gross-Pitaevsky equation for superfluid turbulence which is a nonlinear wave equation, but it is not in the scope of our study.

A major difference between spatial and spatial-temporal random wave ensemble is the anisotropy of wave pattern on spatial and temporal dimension, as shown in figure 2.2. It is apparent that subplot (a)(c) and (b)(d) have different pattern, and that is because (a)(c) are plotting the $x - y$ plane of the wave while (b)(d) are plotting the $x - t$ plane of the wave. While (a)(b) are plotting the real part of the wave, which is of concern in some systems like ocean surface and atmospheric wave, (c)(d) are plotting the complex angle of the wave, which is crucial to other systems such as quantum mechanics and optics. The figure 2.2 is showing what we generate for numerical simulation. Comparing it to figure 2.1 where N is smaller, one can see that the wave ensemble here is more random. If N is too small, then the random fluctuation in the space is rather smooth, and thus there exist less vortices, then it requires many more repeated sampling for statistical result of vortices. On the other hand, if N is too large, then there is too much fluctuation and too many vortices, which require the sampling to have small enough grid to be of high enough resolution to reflect that many fluctuations. As will be shown later, we find phase vortices in the random wave ensemble. If N is too large, then it is possible that one unit box is representing more than one vortex point, and that will cause ambiguity for future analysis.

Here we arrive at another interesting comparison between classical chaos

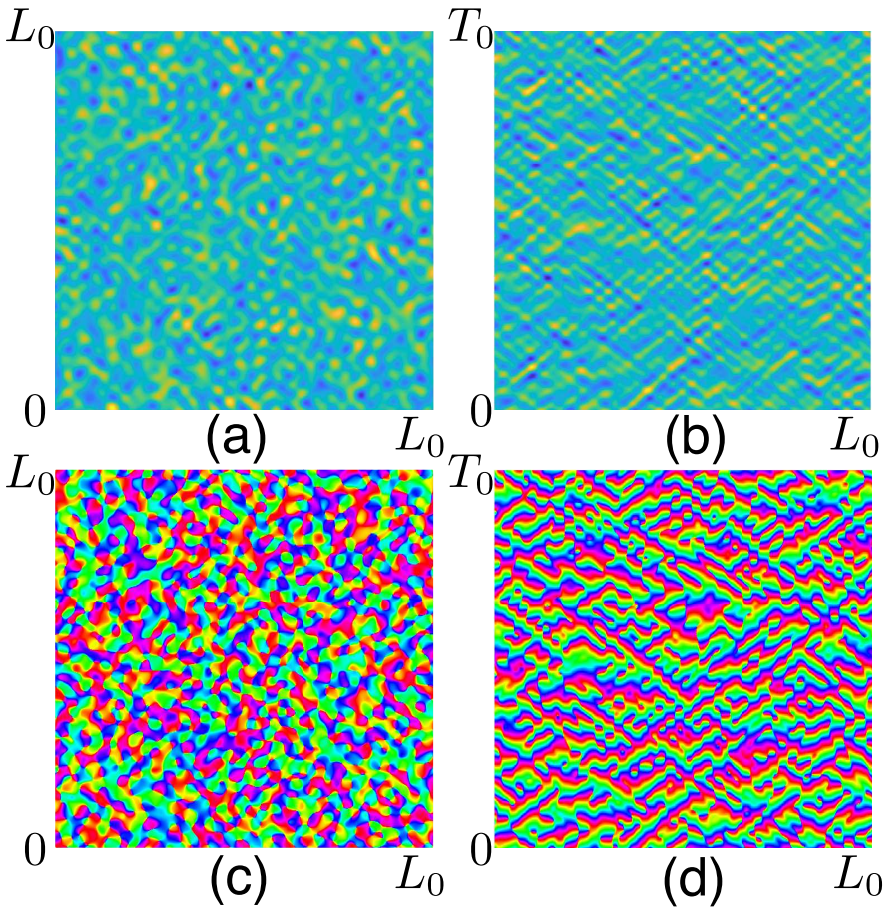

Figure 2.2: A comparison between $x-y$ plane and $x-t$ plane of equation (2.3) with $N = 23$ in d'Alembert dispersion relation, which is what we use for later numerical simulation. Subplot (a) and (c) are plotting on $x-y$ plane while (b) and (d) are on $x-t$ plane. Subplot (a) and (b) are plotting the real part of the wave while (c) and (d) are plotting the complex angle of the wave. It is apparent that the wave is non-isotropical on $x-y$ and $x-t$ plane.

and random wave ensemble in terms of the simulation's resolution. Whether the space-time and physical quantities are continuous or actually grid-like is a question of exceedingly degree of fundamentality, but at least in numerical simulation they are represented by grids and have a certain "resolution". For both classical chaos and random wave ensemble, the more unpredictability the system has, the higher

"resolution" it needs for simulation, because there exists more information per unit grid space. For classical chaos, the more chaotic the system is, the greater is the Lyapunov exponent and thus the more likely the system is sensitive to perturbation; so to be accurate for simulation one needs higher "resolution" such as smaller step-length during numerical integration. On the other hand for the random wave model, the greater N is, the more random waves exist per unit area, and thus yields more information that requires smaller grid to capture. Even though classical chaos and random wave ensemble embrace unpredictability in different nature, they appear similar demand to information's resolution during numerical simulations.

After generating the random waves we look for the phase vortex in the space. Generally speaking the vortices are the zeros of the field, and thus are interpreted as topological defects. In early studies the phase vortices are also referred as "wave dislocation" [Den09] in analogue to dislocation lines in solid lattices. For convenience expressing the complex wave in real and imaginary part as

$$\Psi(\boldsymbol{r},t) = \xi(\boldsymbol{r},t) + i\eta(\boldsymbol{r},t) = \rho\exp(i\chi) \tag{2.4}$$

the phase vortices are the intersection of the zeros of real and imaginary part where

$$\xi(\boldsymbol{r},t) = \eta(\boldsymbol{r},t) = 0 \tag{2.5}$$

the phase at the vortex core is undefined, but there is a net phase change of 2π circulating around the vortex. Topologically such circulation equals a topological charge s which is an integer in unit of 2π

$$s = \frac{1}{2\pi}\oint d\boldsymbol{r}\cdot\nabla\chi \tag{2.6}$$

and topologically is the winding number around the given point.

On the 2D-plane, for simulation the plane is divided into grids, such that the plane is divided into n by n grids of some preferable integer n, therefore the net

phase change of the wave field Ψ at (x, y) is defined as

$$\begin{aligned}\phi_{net} = &\arg(\Psi_{x+1,y} \cdot \Psi^*_{x,y}) + \arg(\Psi_{x+1,y+1} \cdot \Psi^*_{x+1,y}) \\ &+ \arg(\Psi_{x,y+1} \cdot \Psi^*_{x+1,y+1}) + \arg(\Psi_{x,y} \cdot \Psi^*_{x,y+1})\end{aligned} \tag{2.7}$$

which is equivalently tracking through the phase change going from (x, y) to $(x + 1, y)$, then to $(x + 1, y + 1)$ and to $(x, y + 1)$, then finally return to (x, y). $\Psi_{x,y}$ is a phase vortex point on the plane if $\phi_{net} = \pm 2\pi$.

Then we generalize from 2D plane to 3D space. While on 2D planes we search around the four vertices around a face, on 3D there are six faces of each box and we search on that six faces for the trace of vortices. Consider the wave field Ψ at position (x, y, z), even though we later generalize from (x, y, z) to (x, y, t), the algorithm is the same, the net phase change on the six faces is

$$\begin{aligned}\phi_1 = &\arg(\Psi_{x,y+1,z} \cdot \Psi^*_{x,y,z}) + \arg(\Psi_{x+1,y+1,z} \cdot \Psi^*_{x,y+1,z}) \\ &+ \arg(\Psi_{x+1,y,z} \cdot \Psi^*_{x+1,y+1,z}) + \arg(\Psi_{x,y,z} \cdot \Psi^*_{x+1,y,z}) \\ \phi_2 = &\arg(\Psi_{x+1,y,z+1} \cdot \Psi^*_{x,y,z+1}) + \arg(\Psi_{x+1,y+1,z+1} \cdot \Psi^*_{x+1,y,z+1}) \\ &+ \arg(\Psi_{x,y+1,z+1} \cdot \Psi^*_{x+1,y+1,z+1}) + \arg(\Psi_{x,y,z+1} \cdot \Psi^*_{x,y+1,z+1}) \\ \phi_3 = &\arg(\Psi_{x+1,y+1,z} \cdot \Psi^*_{x+1,y,z}) + \arg(\Psi_{x+1,y+1,z+1} \cdot \Psi^*_{x+1,y+1,z}) \\ &+ \arg(\Psi_{x+1,y,z+1} \cdot \Psi^*_{x+1,y+1,z+1}) + \arg(\Psi_{x+1,y,z} \cdot \Psi^*_{x+1,y,z+1}) \\ \phi_4 = &\arg(\Psi_{x,y,z+1} \cdot \Psi^*_{x,y,z}) + \arg(\Psi_{x,y+1,z+1} \cdot \Psi^*_{x,y,z+1}) \\ &+ \arg(\Psi_{x,y+1,z} \cdot \Psi^*_{x,y+1,z+1}) + \arg(\Psi_{x,y,z} \cdot \Psi^*_{x,y+1,z}) \\ \phi_5 = &\arg(\Psi_{x+1,y,z} \cdot \Psi^*_{x,y,z}) + \arg(\Psi_{x+1,y,z+1} \cdot \Psi^*_{x+1,y,z}) \\ &+ \arg(\Psi_{x,y,z+1} \cdot \Psi^*_{x+1,y,z+1}) + \arg(\Psi_{x,y,z} \cdot \Psi^*_{x,y,z+1}) \\ \phi_6 = &\arg(\Psi_{x,y+1,z+1} \cdot \Psi^*_{x,y+1,z}) + \arg(\Psi_{x+1,y+1,z+1} \cdot \Psi^*_{x,y+1,z+1}) \\ &+ \arg(\Psi_{x+1,y+1,z} \cdot \Psi^*_{x+1,y+1,z+1}) + \arg(\Psi_{x,y+1,z} \cdot \Psi^*_{x+1,y+1,z})\end{aligned} \tag{2.8}$$

For each box representing $\Psi_{x,y,z}$, if it belongs to part of the vortex line, then the vortex must come in from one face of the box and go out from another face of the

box. Therefore, if the data of the box is clearly enough, it should have two faces where there is net phase change of 2π. However, it is also possible that there are two vortex lines crossing at the same box because the resolution is not high enough. If the wave ensemble has less number of waves or there are plenty enough boxes to model the random wave with high enough resolution, then boxes should only have two faces where the vortex lines come in from one and go out from the other. However, if the wave ensemble contains a great number of random waves or the boxes is not presenting enough resolution, then it is possible that there are four faces of the box that have vortex coming in and going out. A simple way to solve it is to divide the space and time into smaller boxes to avoid the issue, so that in later analysis two vortex loops will not be accounted to one single loop. Statistically, if there is only a negligible number of boxes that have vortex lines crossed and merged, the analysis result will not be affected because the error from the vortex crossing boxes is balanced by the majority of clearly distinguished boxes. It is only confusing the analysis if there are a significant number of boxes who have four faces of vortex coming in and going out.

By checking the phase change at each point in the space one obtains the vortices in terms of data points, and the following step is to distinguish the vortex lines from another vortex line by checking whether they are connected or separated. The method we use is similar to method used in percolation theory. For each data point in 3D space, one could examine either its six direct neighboring positions (up, down, left, right, forward, backward) or twenty-six neighboring position including the shoulder position whether there is another existing vortex point, and here we adapt the rigorous criterion by only considering the six direct neighboring positions. Consider arbitrary two data points x_1 and x_2, if x_1 and x_2 are in each other's direct neighborhood, then x_1 and x_2 are considered to be of the same cluster. Following this criterion, vortex data points can be classified into independent clusters. In our

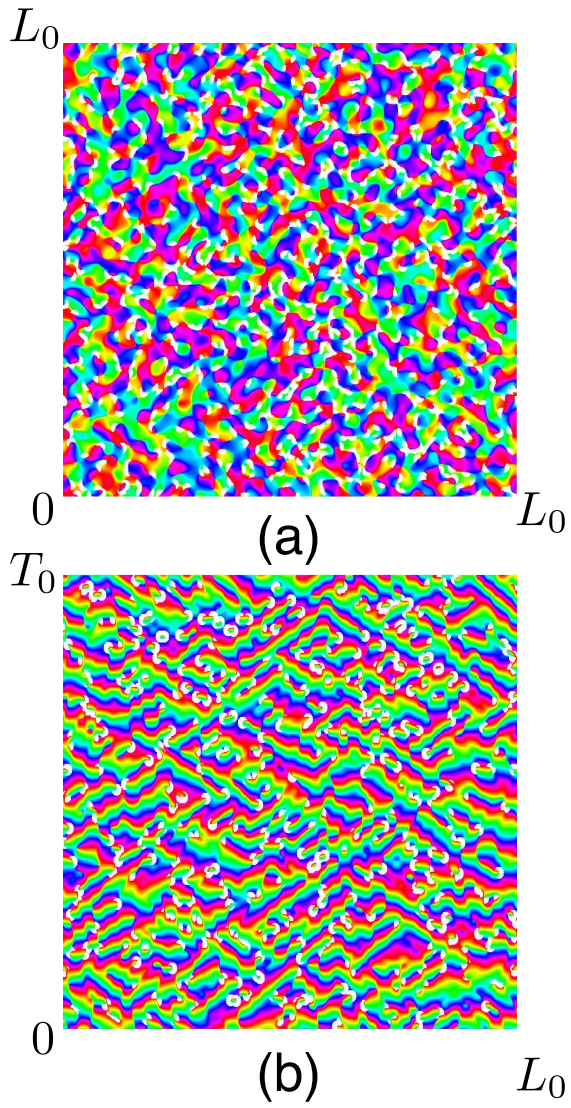

Figure 2.3: Vortices on (a) $x-y$ plane and (b) $x-t$ plane. The vortices are indicated by white circles. Theoretically vortices are lines of no thickness, but are here plotted in large white dots for ease of recognition.

case, such "cluster" is specifically indicating vortex lines.

The reason that these vortex data points only forms into lines but not other cluster such as surfaces is that the vortices are the intersection of the zero contours of real and imaginary part of the wave field. The zero contour of the real part is the

contour of a continuous region where every element in it maps to values of same sign (either all positive or negative). Such contour in 2D is a circle, and in 3D is a sphere. For same reason, the zero contours of the imaginary part are also spheres. Then, the vortex is the intersection of zero contour of real and imaginary part, which is the intersection of two spheres, which is a circle topologically written as S^1. If the loop is cut by the boundary of the space, then it is a line. Therefore, vortices are either homeomorphic to circles or lines.

Since we are studying the random wave of periodic condition, it is crucial to clarify the behaviour of vortex lines in the periodic boundary by clearly telling how and which of the vortex lines are connecting through the periodic boundary. Since one vortex line may cross the periodic boundary several times, it is crucial to identify and combine those vortex lines that are formed by different pieces of vortex line segments. The method of doing so is to find all vortex lines that reach the boundary, and find all line segments whose end point on the periodic boundary is in the neighborhood of one another. Naively, one may assume that a vortex loop is divided by the periodic boundary into two pieces whose end points connect, but in reality things are more complicated than that. For example, we may find line segment A whose ending point on the periodic boundary is x_1 and x_2, while line segment B's ending point is $x_2 + L_0$ and x_3, and line segment C's ending point is $x_1 + L_0$ and $x_3 + L_0$. Line segments A, B, C together form a single loop. As shown in figure 2.4, a single vortex loop may be constituted by several line segments, as adjacent lines are plotted in different color when crossing the periodic boundary.

As we realize that vortices are lines, we may further classify vortex lines into two types: loops and non-trivial homology (NTH) lines. While it is easier to define a loop, which is locally closed vortex lines, NTH lines may also be closed but the difference is that NTH lines are closed only because we are in a periodic boundary

Figure 2.4: Vortex loops identified by combining segments around a periodic boundary. Adjacent vortex line segments are in different color indicating each time crossing the boundary. To correctly identify vortex loops crossing the periodic boundary several times one needs to collect all pieces carefully.

condition, and phase vortices are intersection of zeros of real and imaginary part of the wave function, which is equivalently the intersection of two spheres, which is homotopic to S^1. The difference between loops and NTH lines is that is that isolated loops may be resolved independently topologically, and can shrink away and vanish upon varying the field parameters, while NTH lines may not be shrink to infinitesimal because it persist a non-trivial homology to the topology space of the whole region by "percolating" through it. Therefore, in a simpler way of saying, we categorize loops to be "local" S^1 while NTH lines to be lines that go across from one boundary to another boundary through the whole space like a "percolated" line, either closed or not. When the initial (t=0) wave field is periodic in x and y, its temporal evolution is not necessarily periodic in time, depending on the dispersion relation, therefore while all NTH lines are closed in spatial random wave ensemble, not all NTH lines are closed for spatial-temporal random wave ensemble, but still NTH lines may be distinguished from loops based on whether it "cuts" the plane

cross section of the space into two parts such that one part may not be connected to the other without crossing such NTH line.

The figure 2.5 plots the NTH line d'Alembert and Schrödinger wave field. The NTH lines in d'Alembert are nearly straight lines because they can be seen as segments of a very long loop cut by the boundary. On contrary, NTH lines in Schrödinger may be very long because there is full periodicity on x, y, t. Vortices in different color indicate that they are recognized as different vortices. In panel (b), the gigantic vortex spans the whole space with great length by crossing through the periodic boundary several times, while in panel (a) vortices are in different color because they are connected.

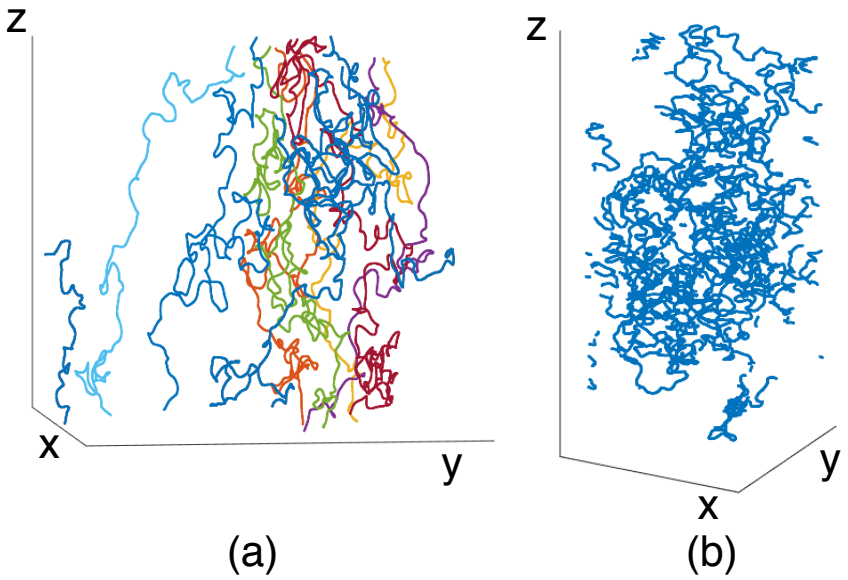

Figure 2.5: The NTH line found in the d'Alembert wave field in panel (a) and in the Schrödinger wave field in panel (b). Due to the boundary periodicity, the NTH lines in d'Alembert are cut on time boundary, while in Schrödinger they may be very long because there is also periodicity on time boundary in Schrödinger wave field.

2.2 Analysis on Random Wave Vortices

2.2.1 Degree of Fractality of Vortex lines

Vortices of different length scale have different geometry and degree of fractality, as shown in figure 2.6. There are small vortex loops and large vortex loop who has different degree of fractality, and there is NTH lines that have similar degree of fractality to large loop, which is of Brownian probability nature.

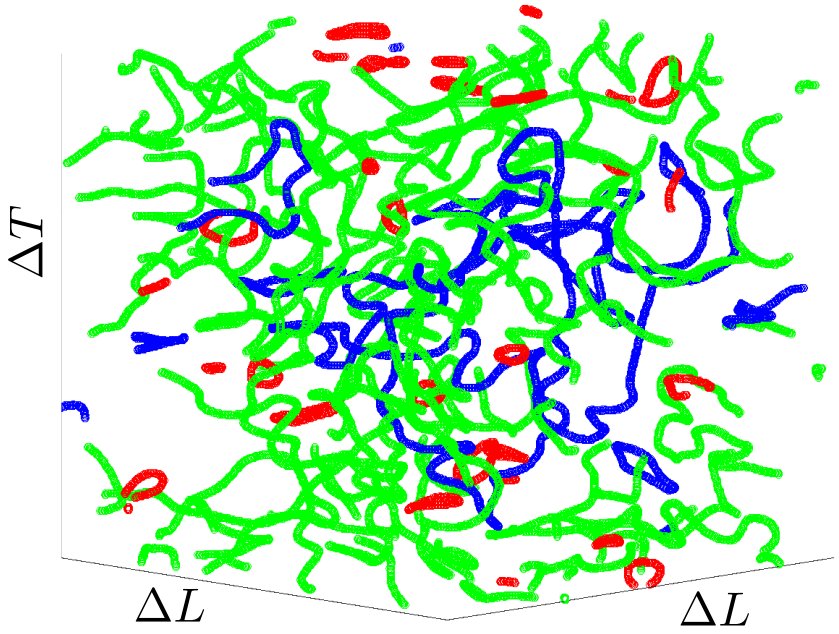

Figure 2.6: Vortices of different length scale plotted in different color in a local region of simulation. The vortices in red are small ones while in blue are large ones. Small and large vortices have different degree of fractality. Lines in green are NTH lines. NTH lines are extensively long, and all green lines belong to a same NTH line.

Fractals are commonly observed in nature, and the principle of fractality plays an important part to the creation and formulation of nature. Fractals are a set of

pattern which is repeated in different scale, and such repetition is usually due to the scale invariance of dominant physical effect. Consider in a region where there exists a field that apply certain effect to objects and such effect does depend on the position of the object, then such effect is scale-invariant, meaning that such effect is constant independent to scales. For example, the growth of tree branches is a straightforward example of fractal. At certain node, the former branch bifurcates into two branches; then at a later node, those two new branches both bifurcate so now there are four branches. Following this trend, the number of branches increases in an exponential speed, and further more since nearly all branches grow to the direction of the sun light, they look even more united. This mechanism of branching at each node does not depend on the position of the branch and simply takes place whenever there is a node, and therefore this branching mechanism can be considered as a scale invariant mechanism, whereas the tree branches form a fractal. This example also shows why fractality and scale invariance is related to a quantity whose growth depends on a power law. This is applied here to the configuration of space-time vortex filaments, such as line length with respect to space-time distance between the endpoints. For example, consider a power law function

$$f(x) = cx^k \tag{2.9}$$

has its domain on region (a, b). Then for $x \in (a, b)$, had there been a scaling factor m to x, then the function is

$$f(mx) = c(mx)^k = m^k \cdot f(x) \tag{2.10}$$

which is simply putting a factor of m^k to $f(x)$ while the function remains scale-invariant.

As fractal geometry involves repeating a pattern across scales, the number of times of such repetition defines the degree of fractality of such geometry. The

fractal dimension is defined as the log of number of repeated pattern over the log of unit length where such repetition takes place [Spr03], that is

$$D = -\frac{\log(N)}{\log(s)} \tag{2.11}$$

where N is the number of pattern repeated and s is the length of a period of the curve.

A similar definition for curves in space of fractal geometry is the relation between the Euclidean distance of two points on a curve and the arc length of the curve between them, as shown in figure 2.7. Consider two points on a curve in space,

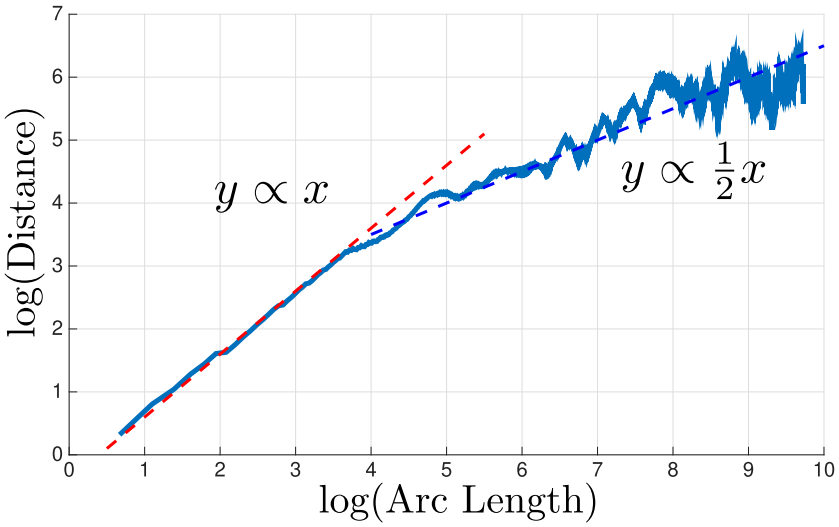

Figure 2.7: The Euclidean distance between two points on vortex loop plotted against the arc length in log-log scale. For small scale loops where the log(arc length) is under 4 the gradient is near 1 while for large scale loops over 5 the gradient is near $\frac{1}{2}$. The region in between is of transition. This plot shows that vortex loops of small scale have geometry of smooth curves while of large scale have geometry of Brownian random walk.

denote the Euclidean distance between them as R and the arc length on the curve

between that two points as l. Then the geometry of the curve may be characterized by the relation between R and l. If there exists

$$R \sim l^D \tag{2.12}$$

then such D may be called as the degree of fractality for the curve, because it categorizes how long does a curve extend in a unit length, which is a constant rate, in analogue to the number of patterns repeated in a unit length in equation (2.11). Firstly consider the simplest example, which is straight line, and obviously it is strictly $R = l$. Similarly, consider a circle-like curve, as the arc length $l = r\theta$, the Euclidean distance between two points is

$$R = \sqrt{2r^2 - 2r^2\cos(\theta)} = \sqrt{2}r\sqrt{1-\cos\theta} \tag{2.13}$$

$$\approx 2r\theta \propto l \tag{2.14}$$

However, for Brownian random curves the relation between R and l is $R \sim \sqrt{l}$ because consider a random walk whose each step $\vec{x_i}$ has length c, then after N steps the mean displacement

$$\langle \vec{x}_N \rangle = \langle \sum_{i=1}^{N} \vec{x}_i \rangle = 0 \tag{2.15}$$

while the mean square displacement is

$$\langle (\vec{x}_N)^2 \rangle = \langle (\sum_{i=1}^{N} \vec{x}_i)^2 \rangle \tag{2.16}$$

$$= \langle \sum_{i=1}^{N} \vec{x}_i^2 + \sum_{i \neq j} \vec{x_i} \cdot \vec{x_j} \rangle \tag{2.17}$$

$$= c^2 N \tag{2.18}$$

as $\langle \vec{x_i} \cdot \vec{x_j} \rangle = 0$ for $i \neq j$. Then

$$R \equiv \sqrt{\langle (\vec{x}_N)^2 \rangle} = c\sqrt{N} \tag{2.19}$$

$$\propto l^{1/2} \tag{2.20}$$

As the discretized arc length $l = cN$.

As shown in figure 2.7, vortex loops of different length scale have different degree of fractal geometry such that they have different D for $R \sim l^D$. For small loops of length below exp(4), $D \approx 1$, meaning that small loops have fractal geometry of smooth curves such as straight line or circular smooth curves. On the other hand, for large loops of length above exp(5), $D \approx \frac{1}{2}$, and large loops have fractal geometry of Brownian random walks. While it is true that one may argue that a curve having $D \approx \frac{1}{2}$ is only a necessary but not sufficient condition of being a Brownian random curve, we find that in large loops the distribution of directions is such that the vortex has an equal probability of turning in each direction, which makes the vortex loop a Brownian random loop.

2.2.2 Vortex Length Distribution

Previously, there have been theoretical studies and predictions made based on different models in different scenarios regarding the length distribution of vortex lines, such as cosmic strings [VV84] and loop soup CP^{n-1} model [Nah+13]. In the thesis I present theoretical analysis and numerical simulation on the length distribution of vortex lines.

The vortex lines may be classified into loops and NTH lines, where in d'Alembert and Klein-Gordon the NTH lines stops at the boundary of time while in Schrödinger the NTH lines gains the extensive length by crossing through the boundary and winding through the space multiple times. In this subsection I show the universal scaling relation of vortex loops and NTH lines length distribution.

The length distribution of vortex loops has universal scaling relation because vortex loops of length greater than exp(5) are closed random walks, or equivalently

random polygons, and form an ensemble of loops of fractal geometry. These loops have length from small to large, and their specific construction may be different, but they are all closed random walks with equal probability on each x-y-t direction. This is saying that such loop ensemble has scale-invariance on the probability distribution, and thus loops form a fractal, because by definition, fractals have certain "pattern" repeated across scales, and in loop soup such "repeated pattern" is the closed random walk.

With this fractality one may arrive at the length distribution of vortex loops. Consider in a region where n is the number density of vortex loops. From dimensionality, since the vortex loops are in three-dimensional space, the unit of n is $1/R^3$, then as one increase the region by dR, there is a corresponding change on the density dn, and from dimensionality there is

$$dn \sim R^{-4} dR \tag{2.21}$$

Combining equation (2.20) and (2.21) it is apparent that

$$dn \sim l^{-5/2} dl \tag{2.22}$$

as the loop length distribution of fractal Brownian closed random walk, and our numerical simulation agrees to it, as shown in figure 2.8.

figure 2.8 plots the histogram of the loop length distribution in log-log scale. It is evident that all four cases considered, which are the 3D random wave as solution to the Helmholtz equation, and 2+1D random wave as solution to the d'Alembert, Schrödinger, and Klein-Gordon's equation, have universal scaling relation of the loop length distribution, which is a gradient near $-\frac{5}{2}$, in agreement to equation (2.22). This scaling relation starts around exp(5.5) and ends around exp(8.5), and is in agreement to figure 2.7, where the large loop starts to exist from length exp(5.5). This is a cross supporting evidence that as loop length goes beyond certain level,

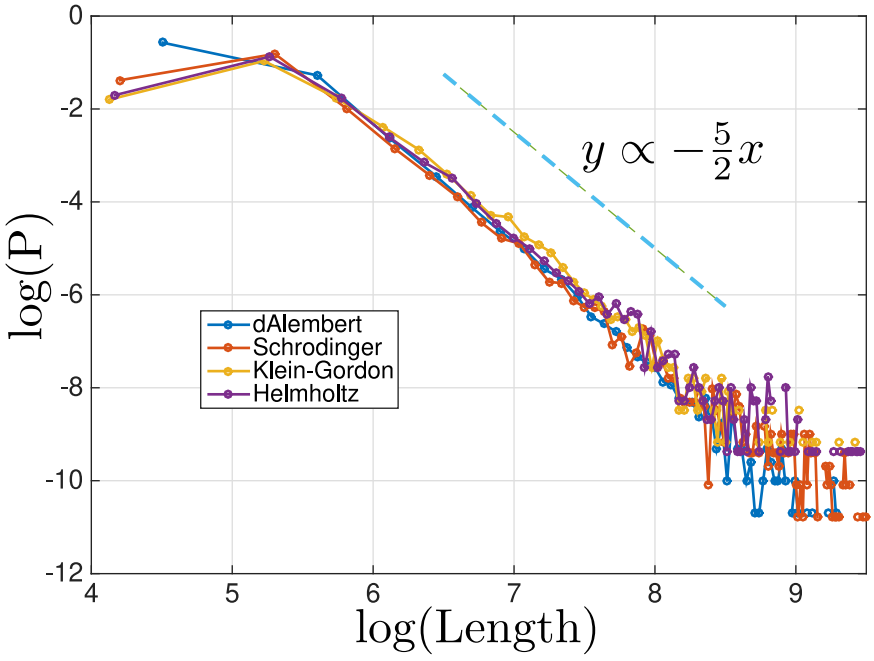

Figure 2.8: The histogram of loop length plotted in log-log scale. In the plot, the vortex loop from length of $\exp(5.5) \approx 244$ to $\exp(8.5) \approx 4915$ has a universal scaling gradient near -2.5, which is in accordance to theoretical result. There are in total four cases for comparison, which is 3D wave as solution to Helmholtz's equation, and 2+1D wave as solution to d'Alembert, Schrödinger, and Klein-Gordon.

which is $\exp(5.5)$ in our simulation, the loops starts to behave like closed random walks.

Besides the length distribution of vortex loops, the length distribution of NTH lines is also studied. The NTH lines percolate through the space, and do not appear as loops. However, according to our analysis to the nature of vortices that since the vortices is the intersection of two spheres, which are the zeros of real and imaginary part of the wave field, they should be loops, therefore NTH lines are ideally loops, but only appear not to be due to other reasons such as periodicity of boundaries or the size of simulation. In some cases the NTH lines are cut by the

boundary which has no periodicity due to the equation form, while in other cases the NTH lines are not presented as loops because the simulation is always finite while there could be part of the NTH line left outside of box. Either way, the NTH lines can be considered as part of the super gigantic loop cut by the boundary, while even such cut fragment is already of great length.

Given that the NTH lines are segments of gigantic loops, and since they percolate through the space, we may approximately view them as very long lines, as thus the density number n of the NTH lines is in unit R^{-1}. Thus,

$$dn \sim R^{-2} dR \tag{2.23}$$

and since equation (2.20)

$$R \propto l^{1/2} \tag{2.24}$$

Togther We get

$$dn \sim l^{-3/2} dl \tag{2.25}$$

ans this scaling relation is observed in figure 2.9.

In figure 2.9 we plot the length distribution of NTH lines in log-log scale of solution to d'Alembert and Klein-Gordon's equation. Even with fluctuation it is apparent that the NTH length distribution have a universal scaling gradient of $-\frac{3}{2}$, which starts around exp(9.1) and ends around exp(11.2), in agreement to theoretical prediction. The plot does not include the NTH line length distribution of the solution to Schrödinger and Helmholtz equation, due to very rare number of NTH line in those simulation.

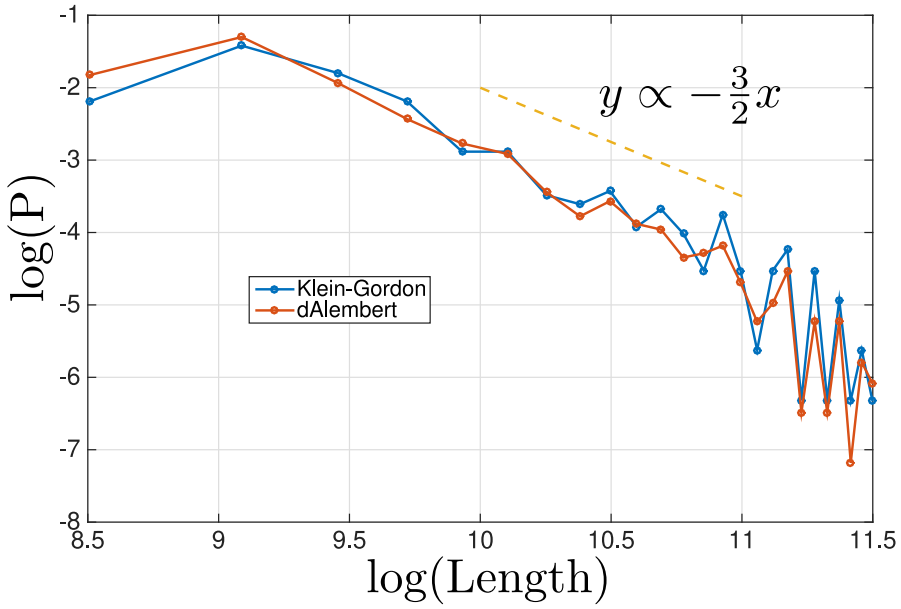

Figure 2.9: The histogram of NTH length plotted in log-log scale. Due to the form of Helmholtz and Schrödinger's equation, the number of NTH lines is extremely rare and makes it very difficult to generate enough sampling to observe a clear statistical pattern of the NTH line length distribution in them. However, there are slightly more NTH lines in the d'Alembert and Klein-Gordon's equation, as shown in the plot. The scaling gradient starts from around $\exp(9.1) \approx 8955$ and ends around $\exp(11.2) \approx 73130$.

2.3 Vortex Analysis Result by Scales

There are in total three types of vortex lines, as shown in figure 2.10. The one of the shortest length is the small loops. According to figure 2.7 they are mainly of length below $\exp(4)$ while their mixture with large loops ends around $\exp(5.5)$. Small loops are smooth curves and have fractal length dimension 1, but their statistical behaviour is model dependent, such as small loops in the d'Alembert's equation are more horizontal while in the Klein-Gordon's equation are more vertical. The second

type is the large loops, their universal scaling relation starts from length exp(5.5) and ends around exp(8.5) and have gradient $-\frac{5}{2}$. The large loops have fractal length dimension $\frac{1}{2}$, and are effectively closed random walks of equal probability on each x, y and t dimension. The third type is the NTH lines. Their scaling relation starts around exp(9.1) and ends around exp(11.2). The NTH lines percolate through the space-time at least one time, and since they are so long that each percolating branch is more like approximately 1D line rather than 3D random walks. Thus even though the NTH lines also have fractal length dimension $\frac{1}{2}$, their universal scaling gradient is $-\frac{3}{2}$.

We believe this classification and analysis of random vortex curves have broad application scenarios because they focus on mathematical meaning of the random curves without much limit from certain specific physical model. We hope the result in this section may be applied to studies on optical vortices, superfluid vortices, quantum chaos, wave chaos and many other cases where the vortices tangle in random waves.

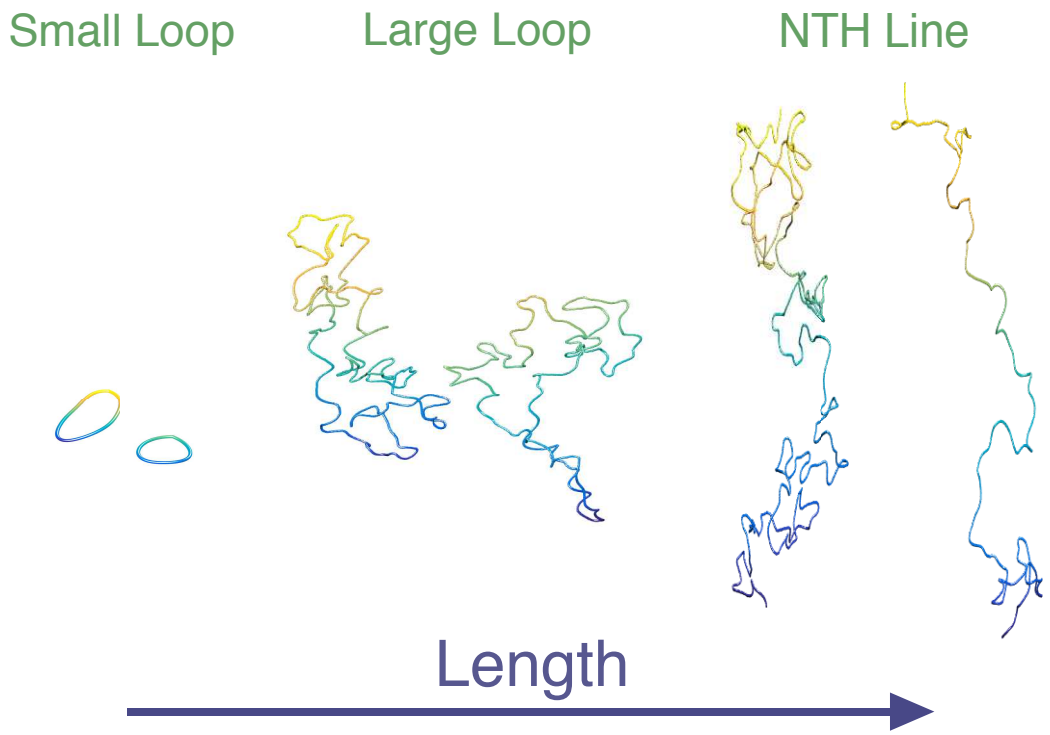

Figure 2.10: Three types of vortex lines plotted for direct comparison. The first type is the small loops, they are smooth curves and have fractal length dimension 1. The Second type is the large loops, they are closed random walks and have fractal length dimension $\frac{1}{2}$. The third type is the NTH lines, they percolate through the space with exceeding length, and also have fractal length dimension $\frac{1}{2}$.

Chapter Three

Probability of Random Knot

In this chapter we propose and verify the general equation of knot probability in random polygons. Sandy Taylor, my supervisor's former PhD student and Postdoc, generated the data and left without doing the analysis. I firstly repeated the method of generating data, and then did the analysis. We discuss two types of polygons: equilateral and non-equilateral, meaning that if the edge-length is constant or varying. We find an equation that can describe probability of all knot types in both cases. Our result in R^3 can be seen as a generalization to previous knowledge of knot probability in Z^3, and we believe our result may be applied to various problems because the knot probability of random walks reflects the geometry nature of 3D random walk. Contents in this chapter has been published as [Xio+21].

3.1 Generating and Distinguishing Knots

In this section we introduce how to generate knots and distinguish knot types for later analysis.

3.1.1 Generating Equilateral and Quaternionic Random Polygon

We begin with a simple clarification between random walks and random polygons. According to the definition, knots are topologically equivalent to loops, which are closed, while in daily life people may consider strings with open ends as knots as well since they are knotted locally. Therefore, we hereby clarify that we refer to knots as their strict definition, which is closed loops instead of any strings that are locally knotted. A problem comes naturally after this clarification is how to generate sampling as targeted, as the sampling being different from simply generating a random walk, which is not closed. For instead, we generate random polygons which are closed. We will explain in detail on our methods of generating random polygons in this section.

We study the probability of knotted random polygons with the contemporary computational ability privilege. In the past, the computational ability of computers pose limit on research topics that requires heavy computation. However, as the computing power increases significantly nowadays, people are now allowed to revisit problems that could be better understood with high performance supercomputers. We conducted a simulation with enormous number of random polygon sampling that exceeds previous attempt. We have a magnitude of 10^9 number of sampled polygons whose edge number goes up to 4000. Our analysis on knotted polygons mainly focused at the range of edge number N from 50 to 3000 where we observe the probability distribution of prime knots and composite knots. We analyzed over 10^8 magnitude of knots in this range of N, and such high data quality provides confidence on accuracy to our analysis.

We generate and analyze two types of random polygons classified by their

edge length distribution. The first type of random polygon is equilateral random polygon, meaning that it is a polygon whose edge-length is all the same. The second type is non-equilateral, specifically generated under Hopf fiberation mapping [CDS13]. We compare the result from these two cases so that what holds between different set-up is truly universal for knot probability of random polygons.

The method we use to generate the first type of random polygons follows that of Cantarella and coworkers [Can+16]. It is an algorithm that enables ones to generate Gaussian random polygons quickly and effectively. The principle of this algorithm is first to generate a polygon with N edges as one hope at once. Then, the polygon is folded in three-dimensional space in a way that the angle of folding between edges is Gaussian randomly distributed. It is worth noticing that during the second step of folding edges with rotational angle, edges are allowed to "cross" each other so they are not real "solid" edges. After these steps of generation, one obtains an equilateral polygon whose angles between edges are Gaussian random, and therefore satisfy the need for a random polygon.

Cantarella refers this method as "action-angle" method because in this set-up diagonal length and dihedral angles form a system of polygon moduli space, and they can be considered as action-angle coordinates in the symplectic geometry sense. Previous to Cantarella's action-angle method, people use "sinc integral method" to generate random polygons. The "sinc integral method" is to generate a polygon each edge one after another determined according to a probability density function adjusted based on previous edges. The advantage of Cantarella's method is its time-efficiency. It is shown by him that generating a N-edge polygon only takes time of $N^{5/2}$ magnitude.

The method we use to generate the second type of random polygons comes from the Hopf fiberation mapping, as previously studied by Cantarella and coworkers

[CDS13]. The Hopf fiberation mapping is a map from three-sphere S^3 to two-sphere S^2, whereas each point in S^2 comes from a circle S^1 in S^3. One may not directly visualize S^3 but may see S^2 in R^3. In order to distinguish the coordinates before and after the Hopf map, we denote the coordinate of S^3 to be x, y, z, w and of S^2 to be a, b, c, then the direct expression of Hopf Mapping from S^3 to S^2 is

$$\begin{aligned} a &= 2(xy + zw) \\ b &= 2(xz - yz) \\ c &= x^2 + z^2 - (y^2 + w^2) \end{aligned} \tag{3.1}$$

such that a, b, c are what we can visualize in R^3 while x, y, z, w is in the pre-image of the map. Based on the Hopf fiberation mapping, Knutson and Haussmann [HK97] constructed a mapping from the complex Stiefel manifold, which here specifically refers to a set of orthonormal 2-frame in n-dimensional space, to an n-edge polygon in three-dimensional space. The process of generating the random polygon is as follow. Firstly, generate a frame with Gaussian coordinate, which are two complex vectors u and w whose real and imaginary part are Gaussian randomly generated n-dimensional arrays.

$$\begin{aligned} u &= a + ib \\ w &= c + id \end{aligned} \tag{3.2}$$

Secondly, perform Gram-Schmidt process on u and w to get new frame u and v. In computer algorithm one may directly write as

$$\begin{aligned} u &= |u| \\ v &= w - (u^* \cdot w) \cdot u \\ v &= |v| \end{aligned} \tag{3.3}$$

Thirdly, apply the Hopf map to the complex frames u and v to obtain the final

random polygon as

$$\begin{aligned} a &= u \cdot u^* - v \cdot v^* \\ b &= 2\Re(u \cdot v^*) \\ c &= 2\Im(u \cdot v^*) \end{aligned} \tag{3.4}$$

whose edge length distribution follows a beta distribution shown by Cantarella et. al. [CDS13].

Following these algorithms, we generate random polygons with different edge number N. The sampled edge number starts from every integer from 6 to 50, because 6 is the minimum number of edges that a polygon could possibly be knotted. However, in the analysis we mainly looked at N starting from 40 to 50 for general knotted behavior, because it is where polygons are random enough for a comprehensive study instead of limited to very simple knots. Then the edge number N increases by 10 from 50 to 200, we keep such increase small enough so that when we fits the probability equation for knots later, our data could be delicate enough to reflect the difference from fitting with different parameters. Next we increase the edge number by 50 going from 200 to 1000. For prime knots the probability function passes over the peak and starts the asymptotic decrease in this range, while for composite knots the peak arrives at larger N and decreases more slowly, as will be explained in more detail in later chapter. In the end, we increase the edge number by 100 from 1000 to 4000. In the simulation, the larger edge number a polygon has, the more difficult it is to be generated. Therefore, we have less number of polygon samples at large N compared to at small N. This only affects our analysis on prime knots with crossing number larger than 8 because their occurrence probability, which is relatively low, fluctuates more obviously. Luckily, we are able to reach a general conclusion on knots based on data we have, as will be further explained in later chapters.

3.1.2 Determining the Knot Type by the Alexander Polynomial and the Reidemeister Move

As introduced in the previous chapter, we explained the definition of Alexander polynomial, how it effectively categorizes knots, and how to compute it. However, in practical calculation the performance could be enhanced by substituting polynomials by numbers, because in computer algorithm it is easier to spot numbers than polynomial. The method to substitute polynomials by numbers is to substitute t in the polynomial by a certain number and then calculate the absolute value of the polynomial. However, that certain number must be chosen carefully because otherwise it is not sufficient to represent different polynomials by different number. For example, the Alexander polynomial for knot 4_1 and 5_1 is $1 - 3t + t^2$ and $1 - t + t^2 - t^3 + t^4$, if we substitute t by -1 we will get result of 5 for both polynomial, which does not allow people to distinguish different knots based on polynomial substitution.

Rather than using symbolic values $\Delta(t)$ of the Alexander polynomial, we substitute t by three different values: -1, $\exp(2\pi i/3)$, and i, because each of these values gives outcome of an integer, and together they give a set of three numbers that are different as long as the original polynomial is different. One can certainly pick more values for substitution to t, but that will spend more time for calculation. In this way the Alexander polynomial of each knot is represented by three values after the substitution, as example of prime and composite knots given in the table 3.1.

As the list shows, if we represent the Alexander polynomial by substituting by these three numbers, we obtain a unique set of numbers for each knot type, and therefore it allows us to verify the knot type by computing the Alexander polynomial

0_1: (1, 1, 1)	3_1: (3, 2, 1)
4_1: (5, 4, 3)	5_1: (5, 1, 1)
5_2: (7, 5, 3)	6_1: (9, 7, 5)
6_2: (11, 5, 1)	6_3: (13, 7, 3)
7_1: (7, 1, 1)	7_2: (11, 8, 5)
7_3:(13, 4 ,1)	7_4:(15, 11, 7)
7_5: (17, 7, 1)	7_6:(19, 11, 5)
7_7 :(21, 13, 7)	$3_1\#3_1$:(9, 4, 1)
$3_1\#4_1$:(15, 8, 3)	$3_1\#5_1$:(15, 2, 1)
$3_1\#3_1\#3_1$:(27, 8, 1)	$4_1\#4_1$:(25, 16, 9)
$4_1\#5_1$:(25, 4, 3)	$4_1\#4_1\#4_1$:(125, 64, 27)

Table 3.1: The three values of the Alexander Polynomial after substituting t by -1, $\exp(2\pi i/3)$, and i

in terms of specific numbers instead of polynomial, and therefore simplifies the calculation.

It is true that the Alexander polynomial may be questioned of its validity for representing knots accurately because for higher crossing knots there exist seldom examples of two different knot type sharing the same Alexander polynomial. However, we find that such confusion is statistically negligible, especially because as we will show in later chapters, our results are mainly based on analyzing knots with crossing number less or equal to eight, where the repetition of Alexander polynomial is rare. We show the validity of representing knots by Alexander polynomial by considering the unknot (trivial knot) as an example, because the Alexander Polynomial for the unknot is 1, which is the most commonly repeated Alexander polynomial among knots. We show that the statistics of the unknot is not affected by other knots whose Alexander polynomial is also 1 in the below paragraph since the pos-

sible confusion is statistically negligible, as the minimal crossing number of them is 11, indicating very low probability of occurrence [Xio+21].

There are in total a number of around 3000 for all knots under 12-crossings, and there are only four of them whose Alexander polynomial is 1, which are also the only four knots whose Alexander polynomial value equals (1, 1, 1) after substituting t by -1, $\exp(2\pi i/3)$, and i. This means that our method of substituting t by -1, $\exp(2\pi i/3)$, and i for the value of Alexander Polynomial distinguishes knots faithfully.

The four knots that has the Alexander polynomial equal to 1 which is the same to the unknot are 11n-34, 11n-42, 12n-313, and 12n-430. In our observation, the occurrence of the unknot has a data magnitude of 10^8, while the average occurrence of the 11n-crossing knots and 12n-crossing knots is of 10^3 and 10^2 data magnitude at the peak of their probability distribution. This means that the systematic error of counting knots by their Alexander polynomial, caused by miscounting other knots who share a same Alexander polynomial, is only in a magnitude of 10^{-5}, which is statistically negligible. While it is true that there exist more knots of higher crossing number, and so there should be more knots whose Alexander polynomial is 1. However, as we will show in later chapters, the probability of knots decreases so rapidly as the crossing number increases, therefore we may see that the total probability of miscounting higher crossing number knots as the unknot is convergent, finite, and statistically negligible.

Another important and straightforward simplification that could be applied to the calculation of Alexander polynomial is Reidemeister move as shown in figure 3.1.

There are three types of the Reidemeister move, and they simplify the ap-

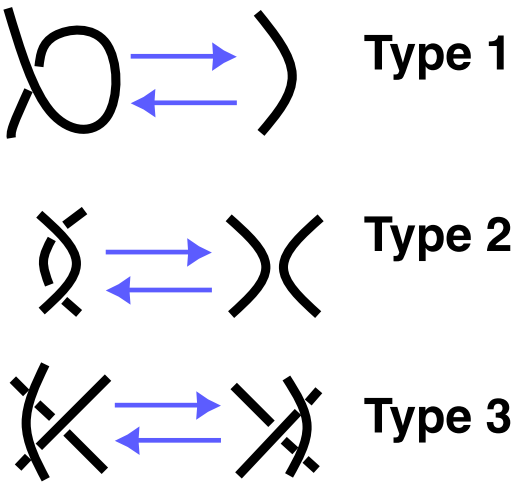

Figure 3.1: The diagram of the Reidemeister move in three types. The knot topology is considered equivalent under these changes thus they can be adapted to simplify the appearance of knots.

pearance of knots without changing its topology. Compared to actions like cutting or reconnecting lines that change the knot type of a given knot, the Reidemeister move does not change the topology nor the knot type of a given knot, therefore we may say that Reidemeister move only simplify the appearance of a knot while keep the knot type consistent. As shown in the plot, the first type of Reidemeister move does the action of "twisting": one may twist a line or twist it back without changing the Alexander polynomial. Algebraically this is because in the first type of Reidemeister move, lines going in a crossing and then going out right after it cancels each other in terms of their term in Alexander polynomial, meanwhile this is also apparent from view that such move does not change the knot type. The second type of Reidemeister move moves one piece of line over another, and the third type of Reidemeister move moves one piece of line over another crossing. The second and the third type of Reidemeister move does not change the knot type because

they do not remove any real crossing of lines but only perform actions that keep the knot type consistent before and after such action. In the sense of topology, equivalence does not break during any movement or action such that only causes change smoothly but not abruptly, such as creating or annihilating discontinuity. Therefore, the three Reidemeister moves are actions that preserve the topology and knot type of knots. While the knot type is preserved, what is changed is the total number of crossings that appear. In another word, Reidemeister move only take way crossings that does not change the topology of knots, and therefore saves the computing time that would be spent on calculating those unnecessary crossings that could be removed by the Reidemeister move, which give no effective information.

As the figure 3.2 shows, in the random polygons that are generated, we find that only a small portion of it is knotted while a greater part of it is unknotted, which should be removed during Reidemeister moves. In the first row of the plot, we show how the trefoil knot (knot 3_1) exists in random polygons. The trefoil knot is the simplest type of knot whose diagram is shown in the beginning of the second row. Then in the following plots we indicate by the red segments the truly knotted part in polygon, and the four of them are all trefoil knot. These four knotted polygons are selected from a range of total length from small to large, while they are all of the same knot type. As the total length of the polygon increases, the portion of the knotted part decreases. This phenomenon shows that even for a very large random polygon, the truly knotted part could be a small portion of it. Therefore, this is an effective example of the importance of performing Reidemeister move to speed up the knot identification, since removing the unknotted part by Reidemeister moves and only compute the Alexander polynomial of the knotted part is more time efficient than directly computing the Alexander polynomial of the whole random polygon.

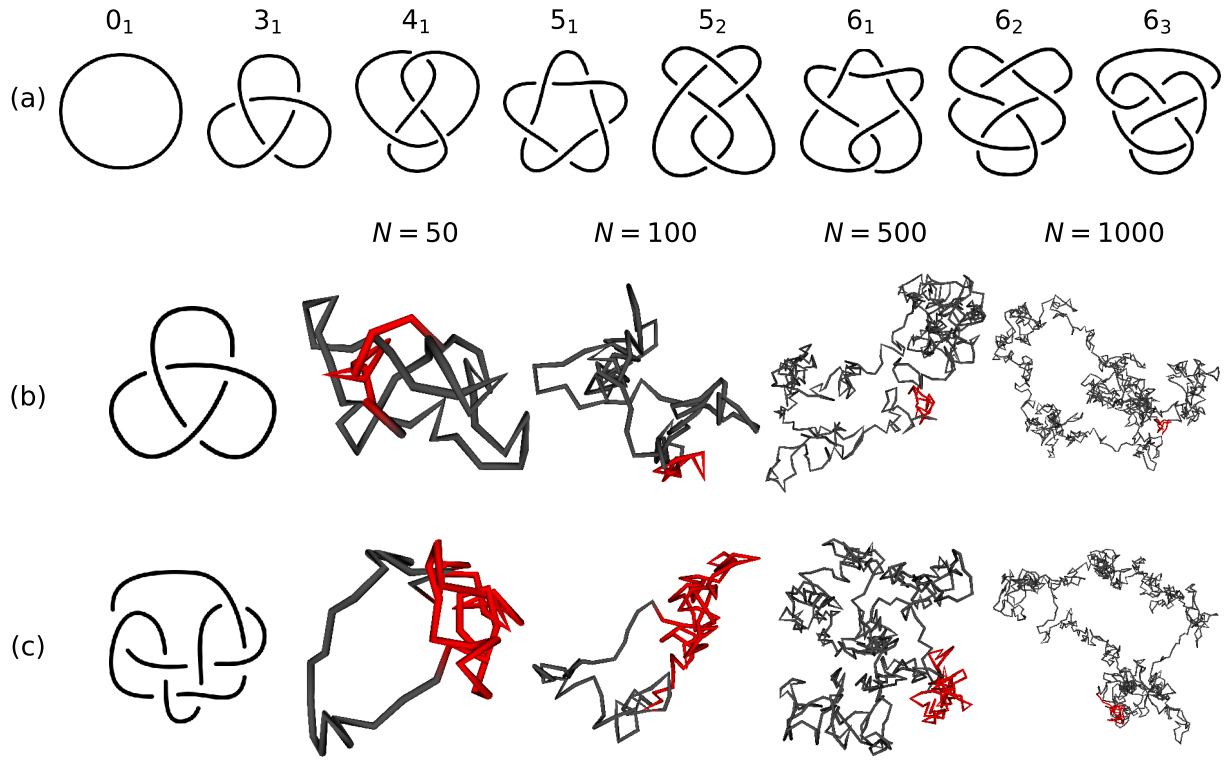

Figure 3.2: Spotted knotted part (coloured in red) in the total random polygon. The first row is the diagram of knots. The second row is the knot 3_1 detected in random polygons with different length, where the detected knotted part is coloured in red. The longer the random polygon is, the smaller is the knotted part, as shown in the figure. The third row is similar to the second row but the knot type is 7_6 instead of 3_1. This figure is generated by Sandy Taylor as part of our published paper [Xio+21], while row (a) is generated by Keith Alexander.

3.2 Analysis

As introduced in the chapter of introduction, previous knowledge on the knot probability of random polygons was worked out on Z^3 lattice model, where Sumners and Whittington [SW88] analytically showed that the probability equation is a purely exponential term, meaning that the probability of the unknot decreases exponen-

tially as the edge number increases, therefore one expects the random polygon to be almost certainly knotted when the edges number tends to infinity. However, as we will further investigate in this chapter, we find the knot probability equation on R^3 is different to previous knowledge on Z^3, and requires an additional power law term. Furthermore with such high accuracy of data we are able to investigate the correction terms of the knot probability equation, which in the end appears as an asymptotic equation. We raise and verify that the following formula as our ansatz is able to describe the probability of all knot types in random polygons

$$P_K(N) = C_K N^{v_K} \exp(-\frac{N}{N_K})[1 + \beta_K N^{-1/2} + \gamma_K N^{-1} + o(N^{-1})] \qquad (3.5)$$

The $P_K(N)$ is the probability of a random polygon being as the knot type K at polygon edge length N. The C_K is an amplitude coefficient that is dependent on the knot type. The N^{v_K} term is the power law term, and specifically we find that $v_K = v_0 + n_p$. For equilateral random polygons we find $v_0 = -0.19 \pm 0.001$ and n_p is the number of components in in a given knot, such as n_p=0, 1, 2, 3... for the unknot, prime knots, composite knots with 2 components, and composite knots with 3 components... For Quaternionic random polygons we find v_K to have the same value but only a larger error bar: $v_0 = -0.19 \pm 0.003$. This means that v_K is a universal coefficient for 3D random polygons independent to the distribution of edge length, and we expect its universality to exist in a wide range in statistical physics. The $\exp(-N/N_K)$ term is an exponential term where we find $N_K = 259.3 \pm 0.2$ for equilateral random knots and $N_K = 430.5 \pm 1$ for quaternionic random knots. The exponential term is not as universal as the power law term, but still is universal in the extent based on models of random polygon generation. For example, the N_K is the same for all equilateral random knots, no matter it is the unknot or prime knots or composite knots. The following terms are the correction terms, written out as an asymptotic expansion of the probability function. We observe that β and γ are knot type dependent, while their values are close for knots with close crossing number,

such as β and γ of 3_1 is closer to that of 4_1 than to 6_1.

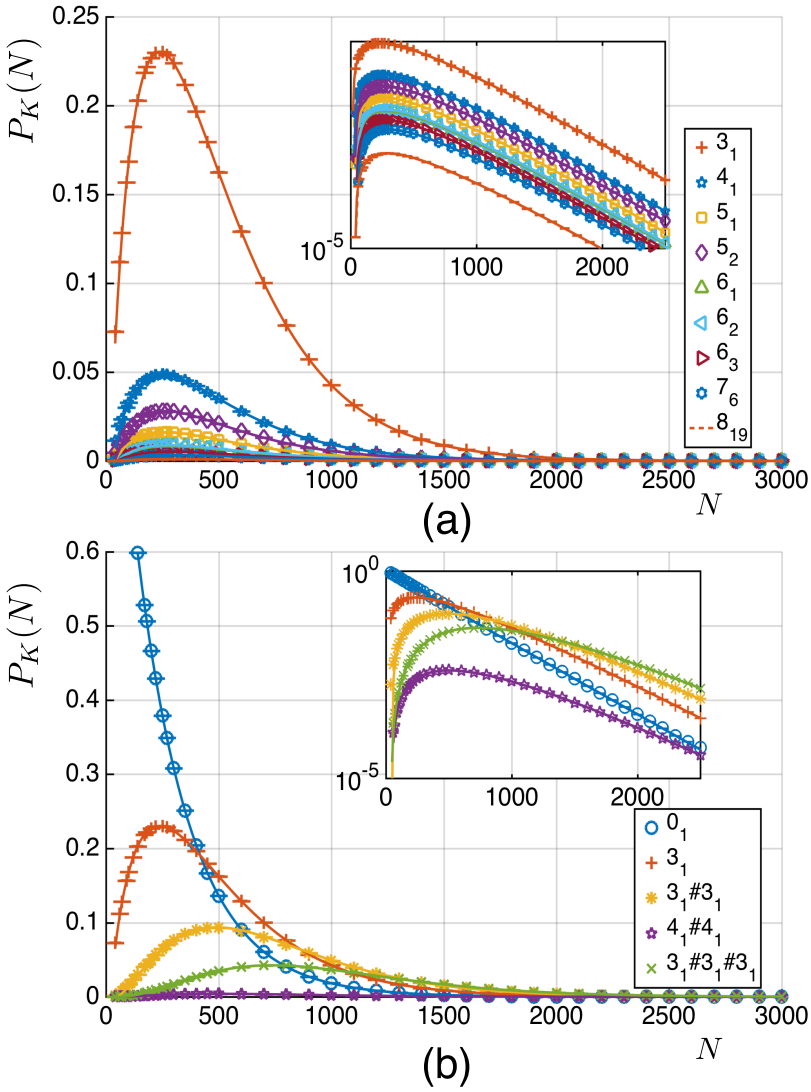

Figure 3.3: The probability distribution data and fit of prime knots (a) and composite knots (b) as a function of N, the edge number of the polygon. We plot the data and the fitting based on our ansatz and they are very close to each other. In the inset, We plot the probability in log scale and in panel (a) and they seems to be parallel to each other, suggesting a universality which is dominated by exponential term of large N.

The panel (a) of figure 3.3 shows the probability of some common prime knots

as a function of N, the number of edges. It is observed that usually the probability amplitude of knots with less crossing number is higher than that of knots with higher crossing number. This is natural in a statistical intuition that knots with higher number of crossings are usually more complicated and therefore less likely to exist. All curves reach their probability peak around 250 to 300, and vanish asymptotically close to zero at N around 2500 to 3000. The inset plot has a logarithmic scale on y-axis, which is the knot probability. It appears that all lines tend to the x-axis with the same gradient, because for large N the equation is dominated by the exponential term, which appears to be horizontal line in logarithmic scale. The error bar is plotted but is too small to see because the sampling is large. Consider a total sample of n polygons with edge number N, and m of them belong to the knot type K, then $\hat{p} = m/n$ is the unbiased estimator of p, the probability of occurrences of knot type K. Define $\hat{q} = 1 - \hat{p}$, then the variance of distribution m is npq and the corresponding standard deviation is $\sigma = \sqrt{npq}$. Therefore, the standard deviation of $\hat{p}$ is $\sigma/n = \sqrt{pq/n}$

The panel (b) of the plot shows the probability of the unknot, prime knot 3_1, and composite knots with two and three components. As the number of components of knots increase, the peak of the probability function arrives later at larger N, while the amplitude is also lower. The inset plot has a logarithmic scale on y-axis, which is the probability. Curves tends to straight lines with different gradient as N increases indicate that with different number of components in the knot, the probability functions do not have same power law and exponential term. This behaviour is different to the inset in the panel a where curves have same gradient indicating that they might have same exponential and power law term. However, it is only a deduction from the appearance, and we will further investigate and prove our claim in detailed analysis in the following.

We compare result obtained from quaternionic non-equilateral random polygon. The figure 3.4 is plotting the same thing to the above plot, which is the probability of prime knots (panel (a)) and composite knots (panel (b)), but generated in our quaternionic model, which serves as a comparison to our result obtained from equilateral random polygon model.

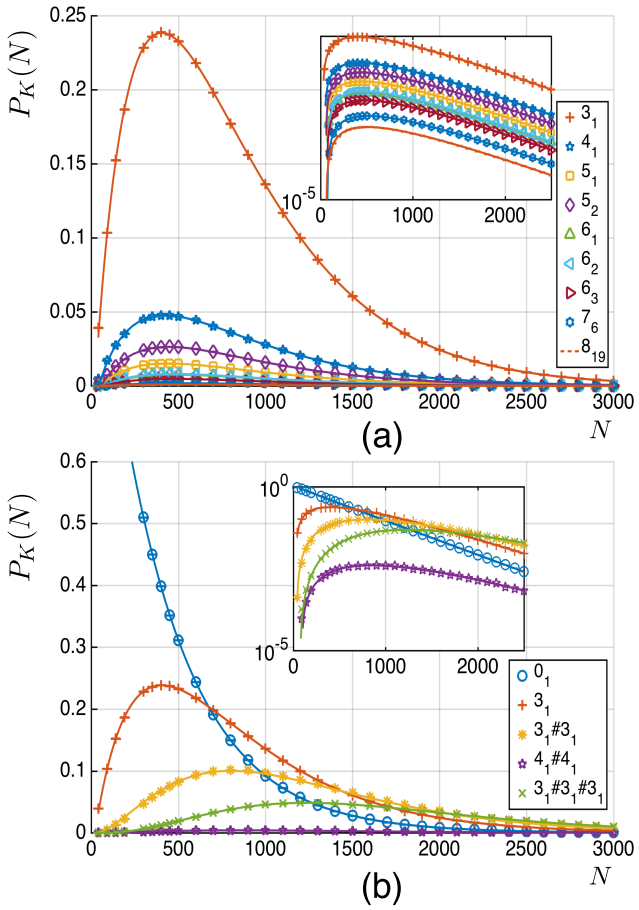

Figure 3.4: The probability distribution data and fit of prime knots (a) and composite knots (b) as a function of N, the edge number of the polygon, of quaternionic non-equilateral case. The difference between the equilateral and the quaternionic systems is that the distributions have a wider span over N in quaternionic case, but the overall styles are similar.

In the plot we observe that the probability function of knots have the same

qualitative behaviour to that in equilateral random polygon model, such as prime knots in the inset plot where probability is in logarithmic scale are in the same shape with the same asymptotic line gradient, and composite knots with different number of components arrives at their probability peak at different N. However, there is difference between these two sets of plots. While the equilateral random prime knots arrive at their peak at N around 250, the quaternionic random prime knots arrive at their peak at N around 450. Similarly, the total span of the probability function of the quaternionic model is wider than that of the equilateral model. Take the prime knot 3_1 as an example, while in quaternionic model it is just starting to approach its asymptotic flat tail at $N = 3000$, in equilateral model it has already been in such flat tail since around $N = 2000$. Similarly, composite knots arrive at their peak at larger N in quaternionic model compared to equilateral model. Therefore, one may conclude that the probability distribution of knots is in the same structure between different knot models, while the quaternionic knot has larger span. This model based difference comes from the fact that if the edge length is not a constant, those edges with shorter length are less probable to take place as effective crossings that lead to knot.

From the comparison on the result obtained from these two models, we should be confident that the probability of knots is a phenomenon with model-independent universality on certain degree. Therefore, in the following content we will explore such universality in quantitative leveled detail.

We start verifying our result from our claim that $v_K = v_0 + n_p$. If we look at the ratio of the probability of two knots, then we obtain

$$\frac{P_{K1}}{P_{K2}} = \frac{C_{K1}}{C_{K2}} N^{v_{K1}-v_{K2}} \exp(-N_{K2}/N_{K1})(1 + \frac{\beta_{K1}}{\beta_{K2}} + \frac{\gamma_{K1}}{\gamma_{K2}}) \tag{3.6}$$

It is obvious from the equation that if v_{K1} and v_{K2} are not equal, or if

N_{K1} and N_{K2} are not equal, then the power law term or the exponential term is nonzero, then the probability ratio should approach infinity or zero in a power law or exponential trend as a function of N. However, as the panel (b) in figure 3.5 shows, the probability ratio of two knots with same number of components reaches a constant asymptotically, therefore it is a clear indication that v_K and N_K is constant for knots with same number of components.

In panel (a) of figure 3.5 we observe that the probability ratio of two knots, where the numerator has one more component than the denominator has an asymptotic gradient of 1 in the log-log plot. According to the probability ratio equation we derived earlier, this is an indication that v_K is independent to the knot type but is dependent to the number of components of the knot, and v_K increases by 1 if the number of component of the knot increase by 1. This is a direct evidence of our claim that $v_K = v_0 + n_p$. This also shows that N_K is independent to both knot type and number of component of the knot, because the exponential term gives no contribution to the plot, otherwise it would not be an asymptotic gradient to 1. In the inset of the plot we plot the gradient deviation as from 1 (panel (a)) and 0 (panel (b)). In panel (a) we choose the fitting range from 200 to 2400 and the gradient deviation is from 0 to 0.06 to 1. In panel (b) we choose the fitting range from 700 to 1800 and the gradient deviation from 1 is mainly around $10^{-}4$, while the largest deviation comes from ratio of $3_1/6_3$, since 6_3 has relatively smaller data count, which leads to larger fluctuation. The error bar is this plot reflect the variance of ratio. For random variable A and B with expectations $\mathrm{E}(A)$ and $\mathrm{E}(B)$, and variance $\mathrm{var}(A)$ and $\mathrm{var}(B)$, the ratio $R = A/B$ has expectation $\mathrm{E}(A/B) = \mathrm{E}(A)/\mathrm{E}(B)$ and the variance $\mathrm{var}(A/B) = [\mathrm{var}(A)/\mathrm{E(A)}^2 + \mathrm{var}(B)/\mathrm{E(B)}^2] \cdot \mathrm{E}(A/B)^2$ for covariance of A and B is zero, such as in this case.

We observe similar phenomena to figure 3.5 from quaternionic non-equilateral

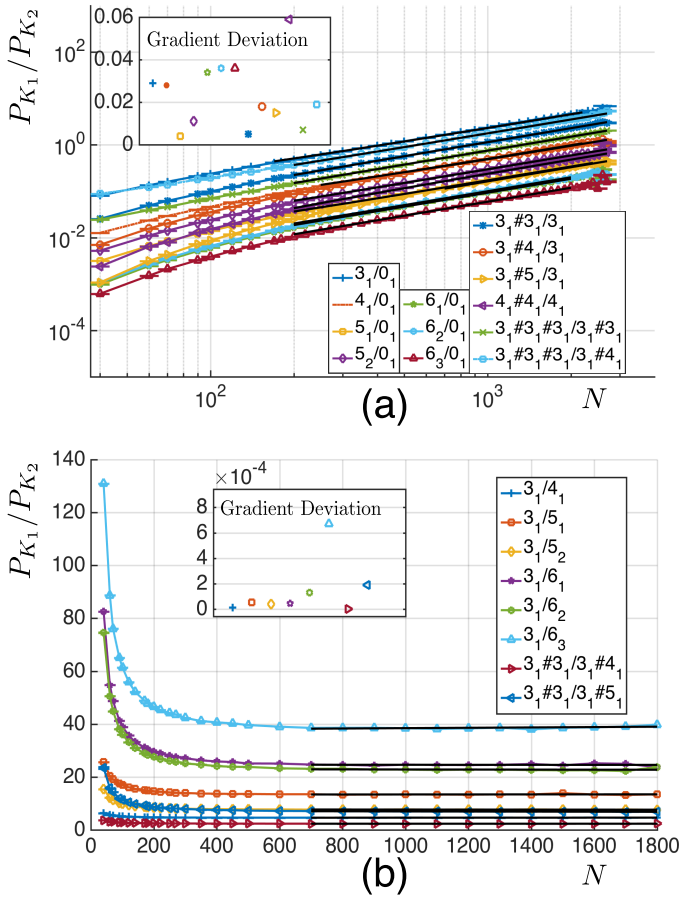

Figure 3.5: The probability ratio of knots with one more component over the other (a), and knots with the same number of component (b), as function of N, the edge number of polygons. Panel (a) is plotted in log-log scale while (b) is in normal scale. The inset plots the gradient deviation from 1 in (a) and 0 in (b), such very small deviation is convincing that the line gradient in (a) and (b) of knot probability ratio is uniformly 1 in (a) and 0 in (b).

random polygon as well, indicating a universal law between two cases. We do not repeat the corresponding plot for quaternionic model because the idea is the same but there is larger fluctuation due to data quality.

Now we have verified that the exponential term $\exp(-N/N_K)$ is universal

within the random polygon generation model, and the power law term N^{v_K} only depends on the number of components in the knot such as $v_K = v_0 + n_p$ where n_p is the number of components and v_0 is the coefficient for the unknot, which is equivalently a "knot with zero component". The question rises right after this is how to determine the specific value of them, which are N_K and v_0.

We do not determine the value of v_0 and N_K solely based on fitting one certain knot type, even though knots such as 0_1 or 3_1 has relatively better data quality than other knots, because there are in total five variable C_K, v_K, N_K, γ and β in the probability function and during the fitting they may vary to balance for the best fit. This is saying that there could be several sets of values for these variables such that they all fit well for the data, and one can not tell from the fitting deviation which set is the best. Further more, the best fitting v_K and N_K also varies when fitting different knot types, and making us unsure about the uncertainty of systematic bias by determining the value of v_K and N_K solely based on one certain knot type.

Instead, we determine the value of v_0 and N_K by comprehensively considering knots with different number of components. We consider the unknot, the 3_1 knot which has the best data quality among prime knots, $3_1\#3_1$ and $3_1\#3_1\#3_1$ which has the best data quality among composite knots with two and three components. For each knot type, we go through a range of v_0, and find the best fitted N_K to the data of each knot type. Therefore, in this way we generate a plot where for each knot type there is a set of (v_0, N_K) for the best fit, and also an error range which is 95 percent confidence range for the fit. At this stage, we also allow the beta and gamma to vary for the best fit.

As the plot shows, for each knot type, the best fit N_K decreases and v_0 increases, and the variation of each v_0 N_K pair falls almost on a line with certain gradient. Since these four knot types we looked at have different gradient, they

hence have an intersection of lines, and we find that intersection to be around $(v0, Nk) = (-0.19 \pm 0.003, 259.3 \pm 0.2)$. Furthermore, the error at this intersection is also the smallest, therefore we determine (-0.19, 259.3) to be the most effective (v0, Nk), since this value of fitted parameters should be effective comprehensively for all knot types.

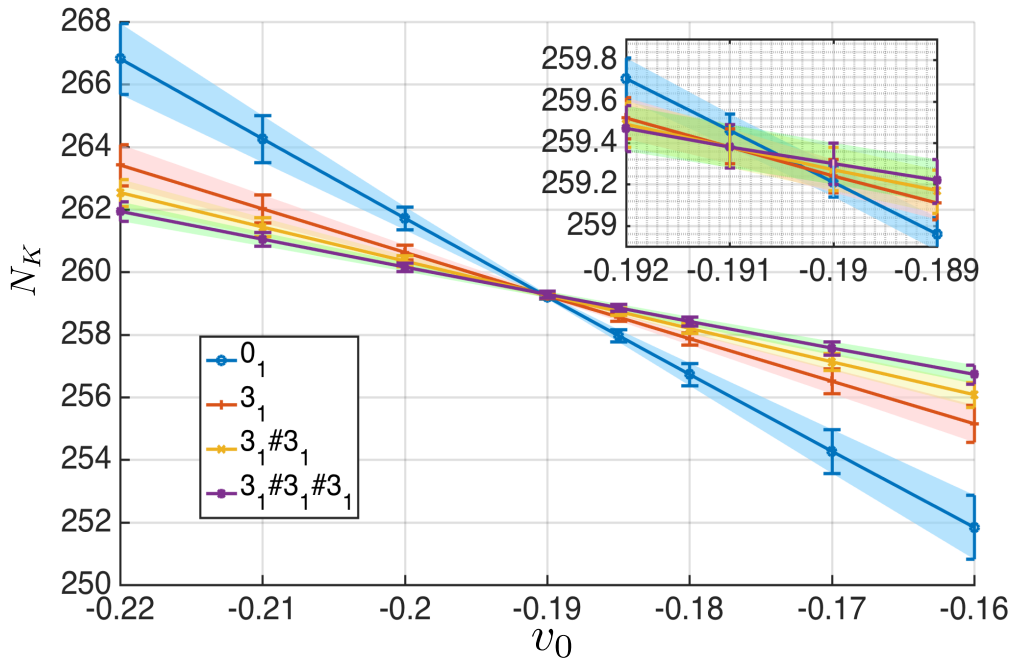

Figure 3.6: Determining the value of N_K and v_0 by varying these two terms together and looking for the intersection of fitted result based on a comprehensive set of knot types. We find $((N_K, v_0)$ to be around value $(259.3 \pm 0.2, -0.19 \pm 0.003)$ because fitting curves of knots with different number of components intersect in this neighbourhood and the estimated error range is the smallest.

In the inset of the plot, we zoom in for a more detailed plot. We look at the situation near our best fit (v_0, N_K), and find that even though not all lines intersect at the same place, the intersection is fairly between v_0 equals -0.19 and -0.191 and N_K equals 259.2 and 259.6, as the line of 3_1 intersect the line of 3_1^3 near $v_0 = -0.191$

while the rest intersections takes place basically in the middle of the range from $v_0 = -0.19$ to $v_0 = -0.191$.

With similar method we look for the best fit v_0 and N_K for the quaternionic model as well, as shown in figure 3.7. Admittedly, our data quality of the quaternionic model is not as good as our equilateral model, because due to the complexity of the algorithm generating the random polygons, it takes more time to generate quaternionic random polygons. Even though, we still managed to generate quaternionic random polygons of magnitude 10^8, and our result on quaternionic case, though not as good as equilateral case, is at least clear enough to reach a conclusion. In the plot where we followed the same method introduced above, we find the best fit (v_0, N_K) for quaternionic random knots is around $(-0.19 \pm 0.003, 430.5 \pm 1)$.

It is worth noticing that the v_0 we find for the quaternionic case is nearly the same to v_0 in equilateral case. This suggests the universality of the power law term in the knot probability function regardless of the model (equilateral or quaternionic). Such universality may extends to the scope of general 3D random polygons, and we are expecting to see our result on this universality to be found in other future studies on knot probability. Meanwhile the N_K we find for the quaternionic case is larger than the N_K in equilateral case, and this agrees to our previous observation that the total probability function has a larger span on N in quaternionic case.

In the inset of the plot we zoom in to see the details. We look for the intersection of the four lines and find that they do not intersect perfectly at one place, but instead there is a range of v_0 and N_K for the intersection and we pick that range to be the error range of the fitted value of v_0 and N_K. While the 3_1^3 intersect with 3_1 and 0_1 at $v0$ around -0.193, the 3_1^2 intersect with 3_1 and 0_1 at around $v_0 = -0.187$. So we estimate the error range of v0 to be -0.19 ± 0.003, and correspondingly $N_K = 435.0 \pm 1$. The error range we find for the quaternionic model

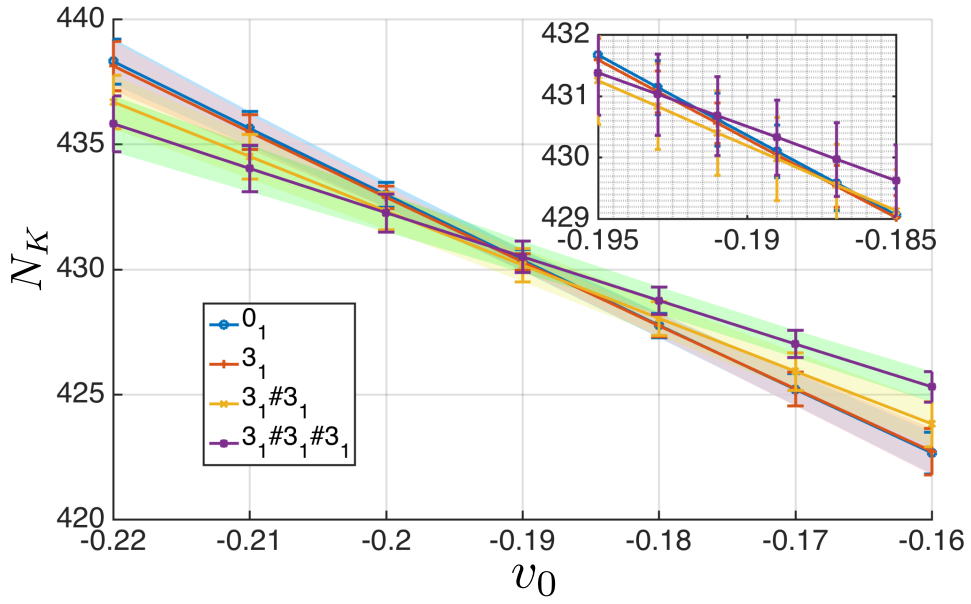

Figure 3.7: Determining the value of N_K and v_0 by varying these two terms together and looking for the intersection of fitted result based on a comprehensive set of knot types. We find $((N_K, v_0)$ to be around value $(-0.19\pm0.003, 430.5\pm1)$ because fitting curves of knots with different number of components intersect in this neighbourhood and the estimated error range is the smallest.

is larger than the error range we find for the equilateral model, but both of them are acceptable, and most importantly, are certain enough to point out the universality of the power law term for knot probability.

Now as we have seen the universality in the knot probability, we understand that while there is different knot types for prime knots and prime knots can get together to form composite knot, and while the appearance of knots may be different, the probability function of different knots in fact has great universality in it. However, it is equally important to point out those parts that are knot type dependent, and together they will complete our understanding of knot probability.

To start, it is obvious that the probability amplitude C_K, is knot type dependent. In figure 3.8 we plot the C_K in logarithmic scale against n_c, the number of crossing, and find that the mean C_k in logarithmic scale of each crossing is almost decreasing linearly. It means that the probability of knots decreases exponentially as the crossing number increases linearly in integer. This shows that most common knots that takes place statistically in nature are more likely to be simpler knots, and knots with higher crossing number are less likely to be observed statistically.

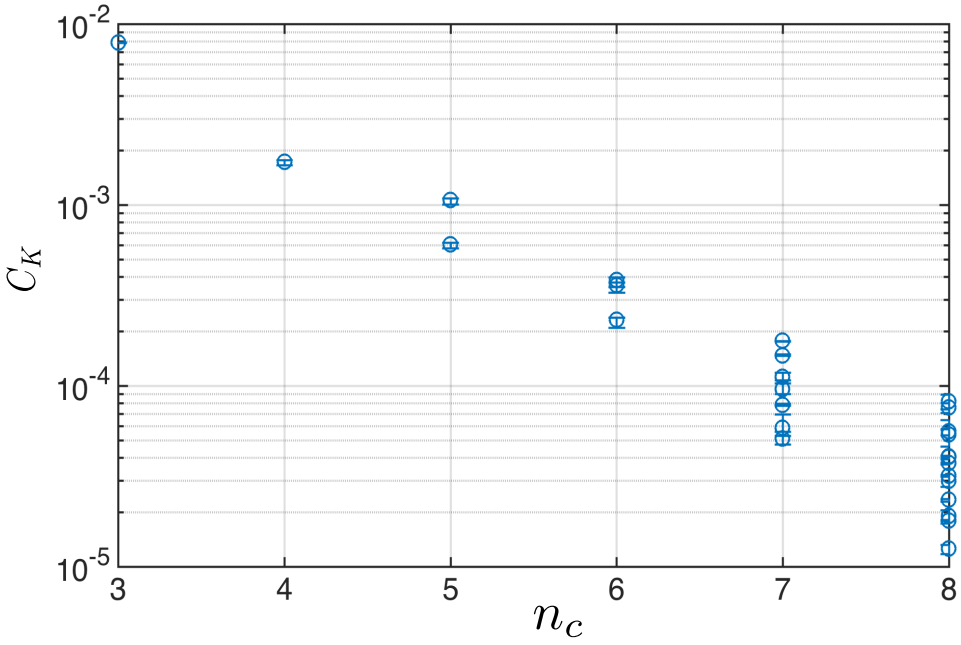

Figure 3.8: The probability amplitude C_K plotted against n_c, the number of crossing of knots, from 3 to 8. We find that the probability amplitude decreases as the number of crossings increases, which reflects an increase of the complexity of knots.

For up to 7 crossing knots, it is true that knots with higher crossing number always have a smaller C_K compared to knots with lower crossing number, however, comparing the C_K of 7 crossing knots and 8 crossing knots we find that some 8 crossing knots have C_K larger than 7 crossing knots. If we interpret C_K intuitively as the bizarreness or complexity of knot structure, then the result means that some 8

crossing knots may actually be simpler than 7 crossing knots. This means that while the mean probability of knots decreases exponentially with the crossing number, the individual probability of certain knot type may be higher than some knots with less crossing number but higher complexity. As the crossing number of knots increases, we expect this phenomenon to take place more frequently, but since the number of knots with even higher crossing number is even more vast, we do not discuss those situations individually, yet we present table 3.2 for C_K stopping at 8 crossing knots for prime knots. In the table we also include C_K of some common composite knots. We write C_K in terms of minus logarithmic scale so that the value looks more consistent and are of the same magnitude. We also include the error estimate from 95% confidence range.

It is interesting to examine the ratio of C_K of two knot types, because the ratio of C_K, reflecting the ratio of the probability of two knot types, could reflect the statistical nature of the random polygons based on the system model. For instance, if two physical systems has the same probability ratio of two knot type, then it is likely that these two systems share some similar nature statistically, because knot probability could reflect the statistical characteristics of systems as its topological defect.

We find the C_K ratio of 3_1 over other knot types. $C_{3_1}/C_{4_1} \approx 4.6$, $C_{3_1}/C_{5_1} \approx 13.0$, $C_{3_1}/C_{5_2} \approx 7.3$, $C_{3_1}/C_{6_1} \approx 22.0$, $C_{3_1}/C_{6_2} \approx 20.7$ and $C_{3_1}/C_{6_3} \approx 34.1$. This means that a trefoil knot is about 4.6 times more likely to take place than the figure-eight knot in equilateral random knots.

We also present a list of C_K in quaternionic model for prime knots and composite knots. For 8 crossing prime knots we only give an estimate C_K value for 8_8 and 8_19, because their C_K is larger than that of most other 8 crossing knots, whose data quality is limited by the probability amplitude and makes it hard to give

K	3_1	4_1	5_1	5_2	6_1	6_2	6_3
$-\log C_K$	4.84	6.36	7.41	6.83	7.93	7.87	8.37
error	0.003	0.01	0.015	0.015	0.024	0.024	0.022
K	7_1	7_2	7_3	7_4	7_5	7_6	7_7
$-\log C_K$	9.88	9.10	9.25	9.74	8.82	8.64	9.45
error	0.03	0.03	0.023	0.03	0.029	0.024	0.027
K	8_1	8_3	8_4	8_6	8_7	8_8	8_9
$-\log C_K$	10.19	10.87	10.36	9.79	10.11	9.49	10.66
error	0.38	0.4	0.38	0.2	0.24	0.12	0.22
K	8_{12}	8_{13}	8_{14}	8_{16}	8_{17}	8_{19}	0_1
$-\log C_K$	10.42	10.11	9.41	10.93	11.28	9.83	1.3
error	0.37	0.25	0.13	0.4	0.44	0.21	0.001
K	$3_1\#3_1$	$3_1\#4_1$	$3_1\#5_1$	$4_1\#4_1$	$4_1\#5_1$	$3_1\#3_1\#3_1$	$3_1\#3_1\#3_1\#3_1$
$-\log C_K$	11.65	12.53	13.72	14.77	15.15	18.84	26.37
error	0.07	0.03	0.037	0.06	0.05	0.02	0.03

Table 3.2: The probability amplitude in minus log and corresponding error range of prime and composite knots for equilateral model.

a good fit to them.

The C_K ratio in quaternionic random polygon model, in terms of ratio of 3_1 over other knots is: $C_{3_1}/C_{4_1} \approx 4.85$, $C_{3_1}/C_{5_1} \approx 13.87$, $C_{3_1}/C_{5_2} \approx 8.0$, $C_{3_1}/C_{6_1} \approx 23.57$, $C_{3_1}/C_{6_2} \approx 23.8$ and $C_{3_1}/C_{6_3} \approx 38.86$. Comparing these result to C_K ratio listed above for equilateral random knots, we find these two C_K ratio value lists are close but not identical. We find our C_K ratio result is different from previous results on lattice model by Janse van Rensburg and Rechnitzer [JR11], but close to previous studies by Deguchi [DT97] done on $\mathbb{R}^3$ random polygon model which is off lattice.

K	3_1	4_1	5_1	5_2	6_1	6_2	6_3
$-\log C_K$	5.14	6.72	7.77	7.22	8.30	8.31	8.80
error	0.01	0.02	0.026	0.024	0.034	0.036	0.05
K	7_1	7_2	7_3	7_4	7_5	7_6	7_7
$-\log C_K$	10.29	9.48	9.60	10.29	9.48	9.59	9.85
error	0.09	0.046	0.048	0.084	0.046	0.046	0.062
K	8_6	8_{19}	$3_1\#3_1$	$3_1\#4_1$	$4_1\#4_1$	$3_1\#3_1\#3_1$	0_1
$-\log C_K$	10.28	10.29	12.47	13.24	15.55	20.10	1.46
error	0.079	0.08	0.1	0.08	0.06	0.2	0.006

Table 3.3: The probability amplitude in minus log and corresponding error range of prime and composite knots for quaternionic model.

Therefore, our result suggests that the C_K ratio may be a universal phenomenon for random knots in $\mathbb{R}^3$, bur may be different to random knots on lattice model which is $\mathbb{Z}^3$.

Besides the probability ratio C_K, the position of the probability peak is another characteristic that distinguish knot types. While we have seen that for prime knots, the great universality leads to the knot-type independence of the power law term and exponential term, suggesting that the dominant term of prime knot probability only differs by amplitude term C_K, there in fact still remains the correction term that is different for different knot type, and a direct contribution from the correction term is the position of the probability peak.

Prime knots have the same dominant term, which is the exponential term and the power law term, and these two terms make the shape of prime knots probability look very similar. However, these probability functions arrive at their peak at different N, as the figure 3.9 shows. For knot 3_1, its peak appears at around 240, while

for knot 4_1 the peak position is at around 250. Following this trend, prime knots with higher crossing number arrives at their peak at larger N, as shown in the plot. This is natural because knots with higher crossing number has more complicated structure, and therefore need higher number of edges to form such polygon, so as the result it is natural that knots with larger size and more complicated structure need more edges to form and to arrive at the probability peak.

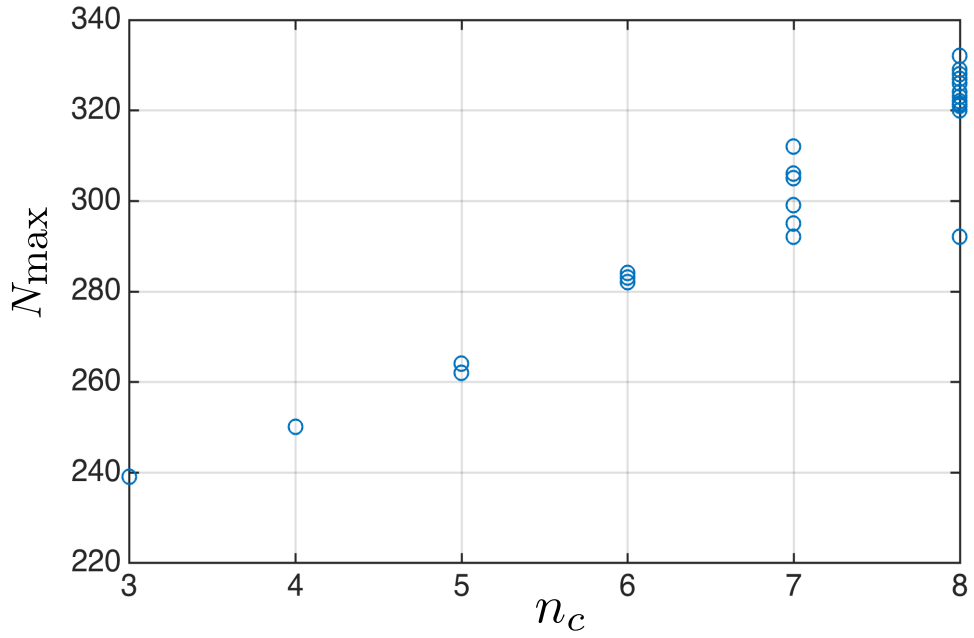

Figure 3.9: The position of the probability peak N_{max} plotted against n_c, the number of crossings of knots. We find that the N_{max} shifts higher as n_c increases, and this phenomena is consistent to our result on the correction terms β and γ, which are responsible for such shift of N_{max}.

Meanwhile, there is exception in this trend, and that is obvious from the plot. It is apparent from the plot that there is a data point in blue circle with eight crossing number that has very small N_{max}, meaning that there is an eight crossing knot whose peak position is far less than other eight crossing knots, different enough to be spotted by eyes, and is even small compared to the peak position N_{max} of most

seven crossing knots. As it turns out, this eight crossing knot is 8_{19}, the first non-alternating knot. Knot 8_{19}, as the first non-alternating knot, is special in sense of its simple and unique structure. The uniqueness of the N_{max} of 8_{19} is a good reflection of its unique structure: it distinguish it from other eight crossing knots, in this intuitive difference of N_{max}, since the statistical probability is a reflection of the geometry of knots.

We therefore believe that the N_{max} is a reflection of the geometry of knots, and of course on the other hand, its algebraic essence comes from the correction terms that we will further discuss in the following content.

We find the correction terms of knot probability to be knot type dependent. Previous studies on knot probability did not give much firm assertion to the correction term of knot probability, while we inherit from previous anticipation that the correction terms are expansion led by terms of $N^{-1/2}$ and N^{-1}, whereas the original asymptotic expansion of the knot probability function is fundamentally N^{Δ} and N^{-1}, and we hereby agree to previous studies and reckon Δ to be $-1/2$.

The figure 3.10 is we plotting the probability ratio of knots against one over the square root of N. The blue circle is the data of the probability ratio, while the yellow curve is the fitted curve of the probability ratio and the red straight horizontal line is the ratio of C_K, C_{K1}/C_{K2}, which is theoretically where the probability ratio curve should approach as N goes to infinity, or equivalently as $1/\sqrt{N}$ goes to zero. The green shaded area is the estimated error range of the C_K ratio, which is calculated based on the error range of the C_K of two knot types. The variance of the ratio of two knot probability, $\mathrm{var}(P_{K1}/P_{K2})$ has expression

$$\mathrm{var}(\frac{P_{K1}}{P_{K2}}) = \left(\frac{\mathrm{var}(P_{K1})}{\mathrm{E}(P_{K1})^2} + \frac{\mathrm{var}(P_{K2})}{\mathrm{E}(P_{K2})^2}\right) \mathrm{E}(\frac{P_{K1}}{P_{K2}})^2 \tag{3.7}$$

Since the covariance of the two knot type probability P_{K1} and P_{K2} is zero, and E is

the expectation value.

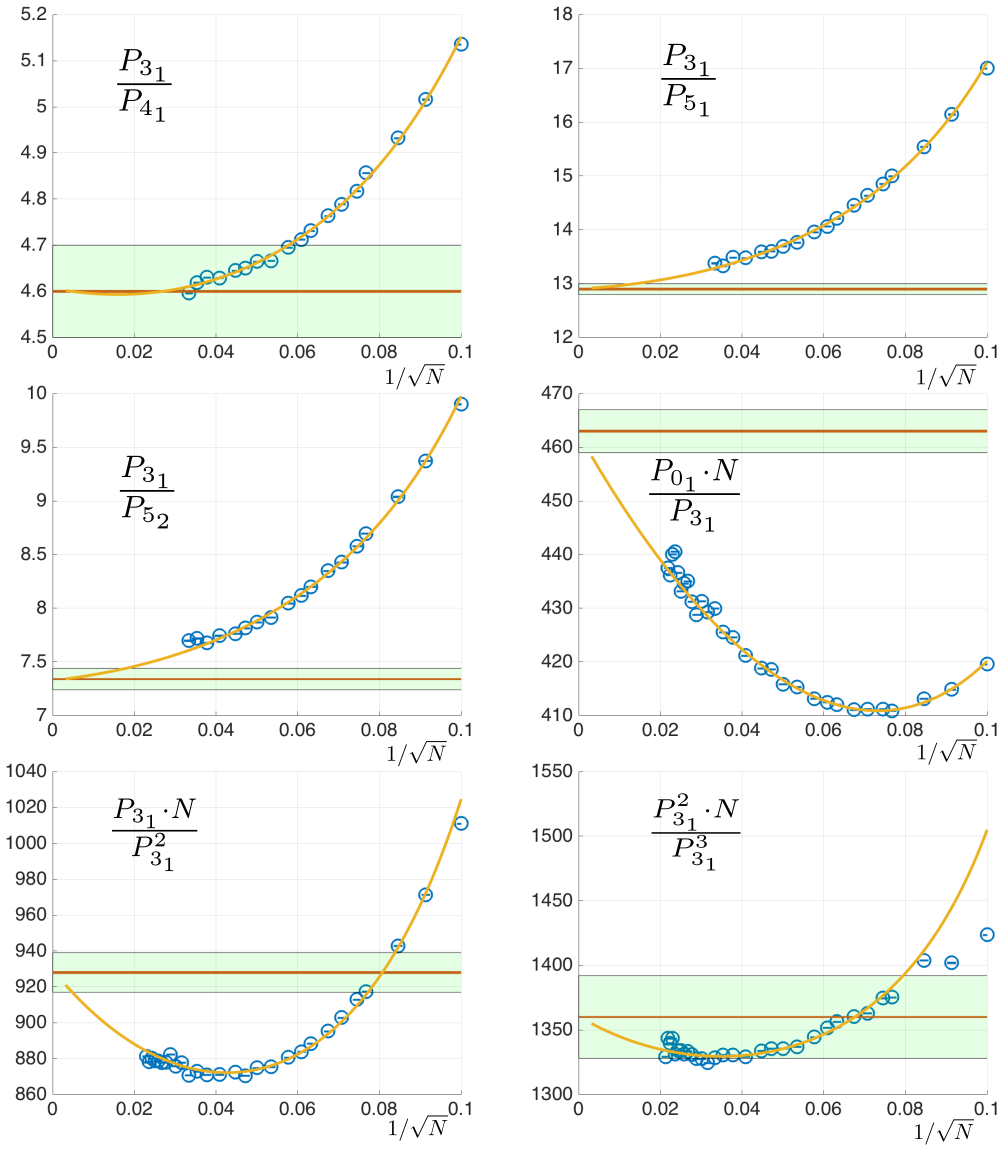

Figure 3.10: The ratio of knot probability plotted against $1/\sqrt{N}$. The curves approaches zero with non-zero gradient suggests that the correction terms of different knot types are different. While some ratio such that P_{3_1}/P_{3_1} has a smaller asymptotic gradient suggesting that the correction terms of these two knots are close, apparent non-zero gradient such as P_{3_1}/P_{5_2} suggests that the correction term of these two knots are more different.

As we have realized in above content, the power law and the exponential term of the knot probability are constant terms for prime knots, therefore plotting the ratio against $1/\sqrt{N}$ gives us information on the correction terms. If the ratio of two prime knots plotting against $1/\sqrt{N}$ approaches the ratio of C_K, C_{K1}/C_{K2}, with zero gradient as $1/\sqrt{N}$ approaches zero, then it means that the $\beta/\sqrt{N}$ term of the two knots is constant. On the other hand, if the ratio of two prime knots approaches the ratio of C_K, C_{K1}/C_{K2}, with nonzero gradient as $1/\sqrt{N}$ approaches zero, then it means that the $\beta/\sqrt{N}$ term of two knots is knot type dependent. Furthermore, if the $\beta/\sqrt{N}$ term of two knots are not the same, the larger is their difference, the greater absolute value of the gradient of the probability ratio curve it has.

In the figure, we firstly look at knot 3_1 over knot 4_1 plotting against $1/\sqrt{N}$. The data of probability ratio approaches around 4.6 as N tends to infinity, which equivalently is $1/\sqrt{N}$ tends to zero. The data approaches the C_K ratio as almost a flat curve, and such very small gradient of the curve implies that the β value of knot 3_1 and 4_1 is very close to each other, and this agrees to our observation on the peak position of knots, whereas the peak of knot 3_1's probability is close to that of knot 4_1, indicating that their correction terms are close as well. Comparatively, the ratio of knot 3_1 over knot 5_1 and 5_2 have a greater gradient of the curve as they tend to the ratio of Ck as $1/\sqrt{N}$ approaches zero. This suggests that the difference between correction term of 5_1 and 5_2 is larger than that between 4_1 and 3_1.

Besides the probability ratio of prime knots, we also plot the probability ratio of knots with different number of component. Specifically we plot knots multiplying N over knots with one more component. We plot $P_{0_1} \cdot N/P_{3_1}$, $P_{3_1} \cdot N/P_{3_1^2}$, and $P_{3_1^2} \cdot N/P_{3_1^3}$. We find they nonetheless have nonzero gradient as they tend to the C_K ratio, and suggesting that they all have different beta value. The set of six plots are the ratio plots with best data quality, even though there is still data fluctuation.

This is because what we plot, the probability ratio of knots, is very sensitive and more sensitive than previous plots we made on other quantities, because the error of the ratio of two incidences is magnified by the error of each incidence, where here the two incidence is the two knots' probability.

Similarly, our result observed from the equilateral model also exist in quaternionic model as the figure 3.11 shows. The data quality of our quaternionic model is not as good as good as the equilateral so we picked the two sets of ratio plots with the best data quality, and it is clear enough that our claim on the correction terms being knot type dependent holds for quaternionic model as well. Plotting is similar style, the blue circle is the data of probability ratio, while the yellow curve is the fitted curve and the red horizontal line is the C_k ratio value, and the green shaded area is the error range. The probability ratio of 3_1 over 4_1 and $0_1 \cdot N$ over 3_1 both have nonzero gradient as $1/\sqrt{N}$ approaches zero.

Acknowledging the fact that the correction terms are knot type dependent, we estimate the value of them from the best fit value while setting the power law and the exponential term with known values and only let the C_K, β and γ to vary for the best fit. We present a list of the best fit β and γ in the following chart. We do not give a specific error range to β and γ individually because it only makes sense to talk about them together since they vary together for the best fit result to the data.

Now we have a clear and deep understanding on each term of the knot probability formula. One issue we need to clarify is about the probability of the unknot, since our result does not exactly agree to previous anticipation on the probability of the unknot.

In previous studies, people anticipated the probability of the unknot P_{0_1} to

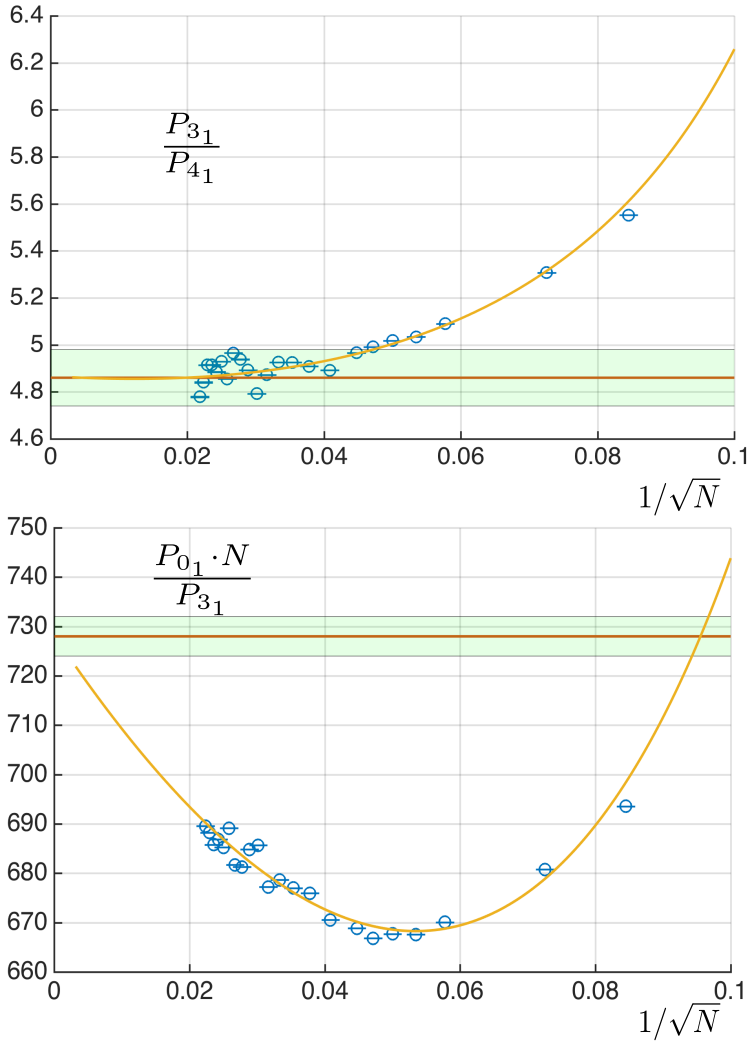

Figure 3.11: The ratio of knot probability plotted against $1/\sqrt{N}$. Similar to the equilateral model, but the data quality is not as good, so there is larger fluctuation. Therefore we only present two cases with best data quality.

be dependent to the exponential term but not to the power law term. The study on the probability of the unknot is probably the earliest and the primal motivation on the study of knot probability in general physics perspective, because the unknot is a single knot type that represent a state of being "unknotted", while other knot types such as 3_1 or 4_1 are all a certain knot type of a "knotted" state. Sometime

K	3_1	4_1	5_1	5_2	6_1	6_2	6_3
$-\beta_K$	1.24	1.14	1.30	1.44	3.63	3.47	3.79
$-\gamma_K$	12.5	21.9	29.7	29.9	22.1	22.9	20.8
K	7_1	7_2	7_3	7_4	7_5	7_6	7_7
$-\beta_K$	5.65	5.91	5.60	4.24	6.55	6.78	6.38
$-\gamma_K$	9.97	10.3	12.0	22.5	5.40	4.03	7.43
K	8_1	8_3	8_4	8_6	8_7	8_8	8_9
$-\beta_K$	8.77	10.24	8.65	9.18	8.68	9.66	8.92
γ_K	8.67	20.6	7.96	10.8	7.26	15.28	9.50
K	8_{12}	8_{13}	8_{14}	8_{16}	8_{17}	8_{19}	0_1
$-\beta_K$	9.78	9.15	10.16	8.31	9.62	7.10	-3.8
γ_K	16.2	12.2	18.8	2.64	15.2	5.7	8.3

Table 3.4: The value of correction terms β and γ for prime knots from 3 to 8 crossings. The values are obtained from the terms balancing each other for the best fit. For simple composite knots there is $\beta_{3_1^2} = +1.7$, $\gamma_{3_1^2} = -48.9$ and $\beta_{3_1^3} = +3.3$, $\gamma_{3_1^2} = -69$.

people may care more about whether a loop is knotted or not, rather than what specific knot type it is in. While it is recognized that, as the number of edges of a random polygon increases to infinity, such polygon will eventually be almost certainly knotted. Since exponential decays are commonly observed in statistical physics and fundamentally appreciated in connection to scale invariance, previously people anticipated the probability of the unknot decays exponentially. However, as we have shown in our result, a single exponential term is not enough to describe the probability of the unknot, while the true essence of the unknot probability is really the probability of a knot with zero component, as falling into the universal class of all knot types with different number of components. While we have shown the

consistency of our model on the probability of all knot types including the unknot, we show in the following why it is not enough to simply fitting the unknot probability without the power law term.

In the figure 3.12 we plot the data of the unknot probability in logarithmic scale in blue circle against N. We plot three types of fitting the unknot in three color: black, red, and blue representing fitting the unknot data with the solely the exponential term $C_K \exp(-N/N_K)(1 + \beta/\sqrt{N} + \gamma/N)$ with the universal N_K we found, fitting with our formula which is a combination of power law and exponential term $C_K N^{\nu_K} \exp(-N/N_K)(1 + \beta/\sqrt{N} + \gamma/N)$, and fitting with the best fit N_K for solely the exponential term $C_K \exp(-N/N_0)(1 + \beta/\sqrt{N} + \gamma/N)$. Simply saying the black and the blue curve are fitting the unknot data with two possibly best choice in exponential term only, while the red curve is fitting the data with both exponential and power law term as we propose. It is obvious that the red curve fits significantly better than the other two to the data. In the inset we plot in the same color the fit deviation of these three models,

$$\text{Fit Deviation} = |P_{0_1} - f_{0_1}|/P_{0_1} \tag{3.8}$$

which is the relative deviation from the fit to the data. The fit deviation suggests that for as N increases, the fit deviation of the two models with the power law term increases linearly, while our model keeps fitting well to the data. The black curve starts to have a systematic deviation starting at N around 300, and the blue curve starts to have a systematic deviation starting at N around 700. Therefore, it is a strong support to our model, and shows the deficiency of fitting without the power law term. Developing from previous knowledge to our correction is somehow like going from Newtonian mechanics to relativity: previous knowledge is not entirely wrong, but just need some amendment when put into a more general context. Newtonian mechanics works fine in our daily life, but when the speed of the moving

object is very high then it is the relativity that reveals a more true essence. Previous knowledge on the unknot probability that thought there is only exponential term is not entirely wrong, and it looks alright for small N. However, when the N is large and when we perform a high quality data simulation, we find that the fit using a single exponential term is poor, and we propose a new model with additional power law term that describes the unknot probability more accurately.

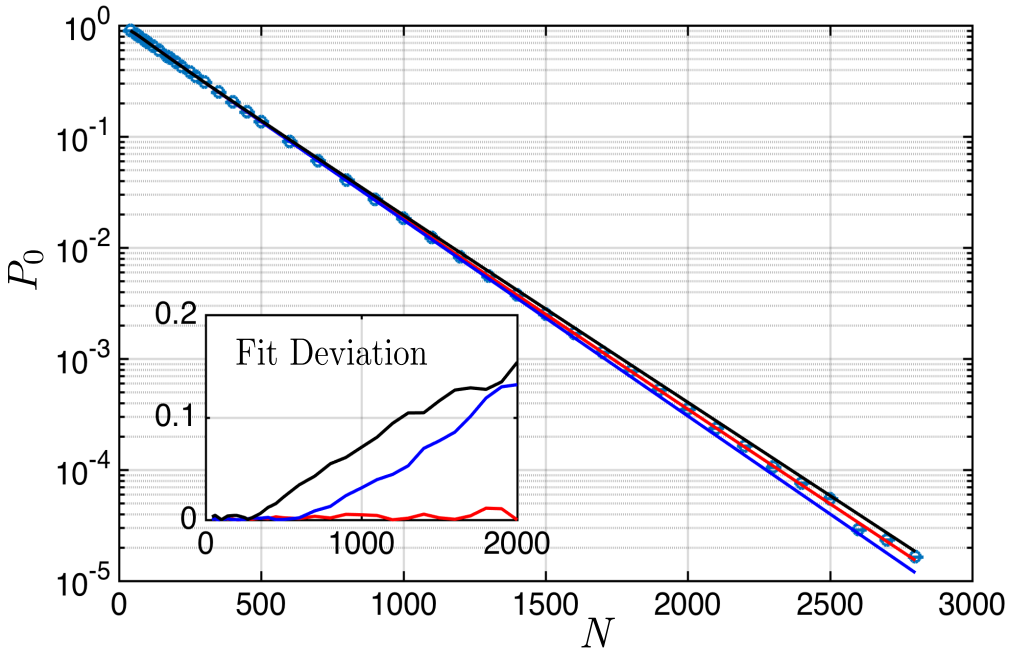

Figure 3.12: Comparison between three types of fitting the unknot data by plotting the probability against N. It is evident that our ansatz fits significantly better than the other two equations that do not contain the power law term. In the inset we plot the fit deviation of the three curves and the two equations without the power law term have a clear systematic deviation.

In quaternionic model we find similar result. The blue circle is the data of the unknot in logarithmic scale plotted against N, the three fitted curve in black, red, and blue are fitted by $C_K \exp(-N/N_K)(1+\beta/\sqrt{N}+\gamma/N)$, $C_K N^{\nu_K} \exp(-N/N_K)(1+\beta/\sqrt{N}+\gamma/N)$, and $C_K \exp(-N/N_0)(1+\beta/\sqrt{N}+\gamma/N)$. Similar to our color indica-

tion in equilateral model analysis, these three colors indicate fitting by the exponential term with N_K we found for universal class, fitting by power law and exponential term together as we propose, and fitting by the exponential term with best fit N_0.

We find similar result in quaternionic model to equilateral model. The red curve fits better than the blue and black curve, and as shown in the inset, the black curve fit deviation starts to grow almost linearly from N equals around 500, and the blue curve fit deviation starts to grow almost linearly from N equals around 1000. It is evident that the red curve fits substantially better than the other two curves without a clear systematic growth of fit deviation. The systematic deviation of the black and blue curve in this plot is not as significant as that in the equilateral model, and this is because the total span of knot probability in the range of N is larger in quaternionic model as shown in previous plot figure 3.13, and arrives at probability peak at later at larger N as shown in figure 3.13. Similarly, the systematic deviation of fitting the unknot grows slower than that in equilateral model. However, as larger N, the unknot probability is very small and decreases very quickly, leading to larger data fluctuation and much more effort to push forward simulation for even larger N. Therefore, we stop our analysis at $N = 3000$, as the imperfection of fitting without the power law shows its obvious trend in a linearly growing systematic deviation.

Readers may question the meaning and significance of showing how adding a power law term helps increasing the fitting quality, since if one fits with one more term, then it is likely and natural that the fitting quality is improved. Actually, there are two types of "better fit", distinguished by whether the improvement of the fitting is systematic or not. Take our case as example. In our analysis, if we fit without the power law term, there is a linear growth of fit deviation as N increases, and such deviation is systematic: it is not a random noise, but a linear growth. Comparatively, if we introduce the power law term, such systematic deviation vanishes, and

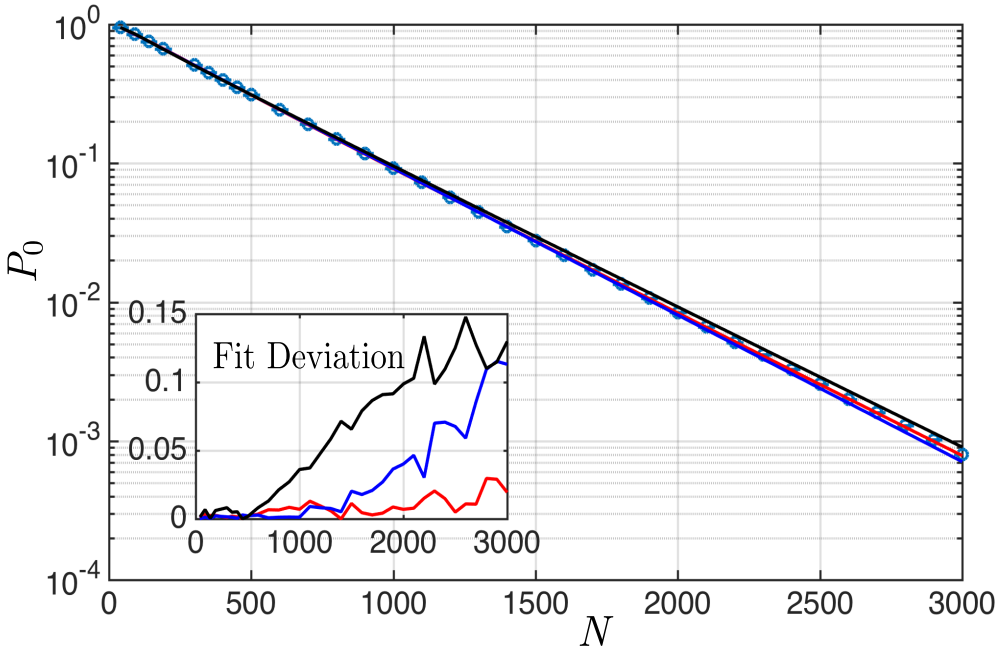

Figure 3.13: Comparison between three types of fitting the unknot data by plotting the probability against N. It is evident that our ansatz fits significantly better than the other two equations that do not contain the power law term. In the inset we plot the fit deviation of the three curves and the two equations without the power law term have a clear systematic deviation. This is similar to figure 3.12 but with large span on N, which is consistent to other results from quaternionic model.

only leaves noise-form deviation. This means that introducing the power law term improves the quality of fitting systematically, which is different from another type of improvement, that a systematic error decreases to a smaller systematic error, or a noise decreases to a smaller noise. If introducing a new fitting term only results in a smaller noise, then one may not be certain that such new term is necessary and reflecting nature. However, since we reduced systematic deviation by introducing the power law term, we believe such term is necessary and fundamental. Furthermore, having the power law term as part of the unknot probability falls into our big universal equation that well explains the probability of all knot types, where the

unknot is equally a knot type with zero component. Therefore, we believe our result improves the previous knowledge on knot probability.

Chapter Four

Wave Vortex Worldsheet in Space-Time

In this chapter we show how to construct complex field that satisfies the d'Alembert equation and whose vortex is knotted as designed, which evolves in space-time. We find that while the topology of the vortex worldsheet in space-time is invariant under Lorentz boost, the topology of vortex in time-slice is dependent to the reference frame of the observer. We also discuss the vortex speed and find the superluminal and subluminal region on the vortex worldsheet.

4.1 Fundamental Topological Events in Space-Time

As we introduced in the introduction chapter, previously people [Bra28; Mil16] have developed techniques on constructing knots in static three-dimensional complex space in terms of u, v which are

$$u = \frac{x^2 + y^2 + z^2 - 1 + 2iz}{x^2 + y^2 + z^2 + 1} \tag{4.1}$$

$$v = \frac{2(x + iy)}{x^2 + y^2 + z^2 + 1} \tag{4.2}$$

In this section we develop such technique and generalize it from constructing static knot in 3D space to constructing knots in 3+1 space-time that satisfies the d'Alembert equation.

The wave equation found by d'Alembert in 1D is

$$\frac{\partial^2 u}{\partial t^2} = c^2 \frac{\partial^2 u}{\partial x^2} \tag{4.3}$$

and for general expression one may concisely write

$$\frac{1}{c^2}\partial_t^2 \psi - \nabla^2 \psi = 0 \tag{4.4}$$

which is one of the most commonly seen wave equation and describes various mechanic waves such as water wave and sound wave. While it is true that the simplest non-trivial solution to the d'Alembert equation is the plane wave equation as we used in the chapter of 2+1 random wave statistics, the solution to the d'Alembert equation may take various form, and one may even transform a given equation in (x, y, z) into an equation in (x, y, z, t) which is solution to d'Alembert equation and remains the same at t=0.

The method we use to transform certain initial state into a function that satisfies the d'Alembert wave equation is as follow [CH08]. The basic idea is that the propagation of wave in space-time is only dependent to its past light cone, which intersects with the sphere of radius ct centered at it, so one can integrate it in spherical coordinate to obtain the function from the initial state. This is a type of Green's function that if one knows the solution to a differential equation at certain point, and if the differential operator is linear, then one can find a general solution to the differential equation. Specifically, we start from designing a function whose vortex is knotted through the construction from u and v, and we let it be the known solution to the d'Alembert wave equation at $t = 0$. Then we use Green's function to integrate the function at time zero, so that we obtain a function that satisfies the

d'Alembert equation and whose vortex at time zero is knotted as designed. Consider a complex function Ψ dependent on (x, y, z), through the construction from u and v, the vortices in Ψ is knotted as designed. Consider such function and due to the spherical nature of u and v for simplicity we only take the numerator of Ψ because this only changes the unit of the field, then the equation may be transformed into form of spherical wave which is replacing the coordinate (x, y, z) into

$$\Psi'(x + ct\cos(\phi)\sin(\theta), y + ct\sin(\phi)\sin(\theta), z + ct\cos(\theta)) \tag{4.5}$$

Then integrate it in spherical coordinate

$$\Psi_s = \frac{1}{4\pi}\int_0^{\pi}\int_0^{2\pi} \Psi' \sin(\theta) d\phi\theta d\theta \tag{4.6}$$

Then take the derivative in time to obtain Ψ_t

$$\Psi_t = \frac{d}{dt}\Psi_s \tag{4.7}$$

and this Ψ_t satisfy the d'Alembert wave equation such that

$$\frac{1}{c^2}\partial_t^2\psi_t - \nabla^2\psi_t = 0 \tag{4.8}$$

and it equals to the initial static function at time zero such that

$$\Psi_{t,t=0} = \Psi \tag{4.9}$$

Following this procedure, we obtain equation $\Psi(x, y, z, t)$ that satisfies the d'Alembert equation and has geometry as designed at time is zero. Denote this transformation as F so that Ψ_t obtained in equation (4.7) will be defined as

$$F(\Psi) := \Psi_t \tag{4.10}$$

Further more, in later context we may set $c = 1$ for c in d'Alembert equation (4.4) for simplicity, unless stated otherwise.

Then the simplest example of this transformation may be performed on $\Psi = u$ whose vortex at $t = 0$ is a flat loop, and after transformation F it becomes

$$F(u) = x^2 + y^2 + z^2 + 2iz - 1 + 3t^2 \tag{4.11}$$

This field F as function of (x, y, z, t) has vortex of a loop because $F(\Psi, t = 0) = u$, but as shown in figure , the whole world sheet of the vortex, is a sphere.

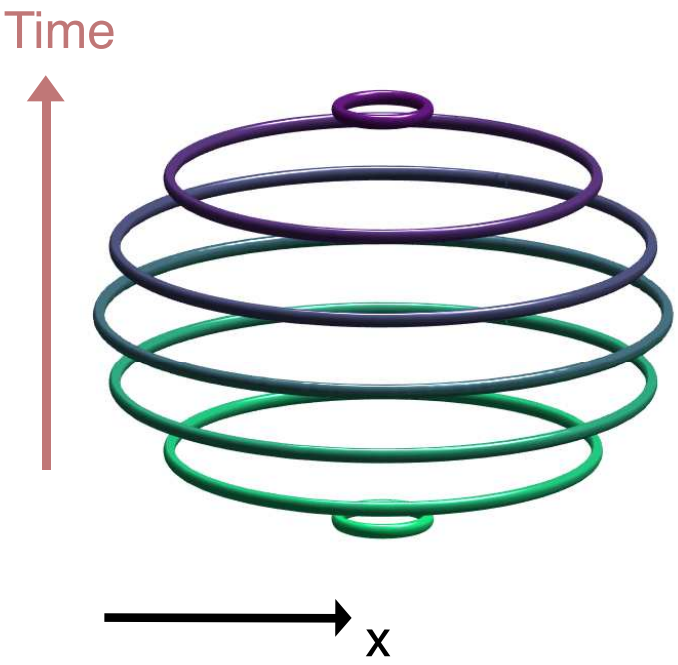

Figure 4.1: The vortex world sheet, equivalently the set of zeros in the space-time of F(u), is a sphere, which is the space-time trajectory of a loop from its creation to annihilation.

The space-time trajectory of this vortex is a sphere, because it is what a loop swipes around from creation to annihilation. Since the vortex loop at each time cross-section is two dimensional in this case, the whole vortex world sheet is three-dimensional.

We present analytical analysis to the vortex world-sheet, such as spotting the

topological event and finding the vortex speed.

The topological event in this case is the creation and annihilation of the loop. As shown in figure 4.1, the loop grows from small to large and then shrink from large to small. The "north pole" and "south pole" of the sphere is where the vortex appears and disappears. At these two points, the vortex shrinks to the origin point $x = y = z = 0$, plugging this into $\Psi = 0$ one obtains the time of topological event as

$$t_{\text{event}} = \pm\frac{\sqrt{3}}{3} \tag{4.12}$$

To find the vortex velocity, one firstly express the wave field in terms of the real and imaginary part as

$$\Psi(\boldsymbol{r}, t) = \xi(\boldsymbol{r}, t) + i\eta(\boldsymbol{r}, t) \tag{4.13}$$

and the associated current J is

$$\boldsymbol{J} = \Im(\Psi^* \nabla \Psi) \tag{4.14}$$

and the vorticity Ω is

$$\begin{aligned} \boldsymbol{\Omega} &= \frac{1}{2}\nabla \times \boldsymbol{J} \\ &= \nabla\xi \times \nabla\eta \end{aligned} \tag{4.15}$$

Since the vortex is the zeros of the real and the imaginary part of the wave, which is

$$\xi(\boldsymbol{r}, t) = 0, \eta(\boldsymbol{r}, t) = 0 \tag{4.16}$$

As we are looking for $v = \frac{dr}{dt}$ differentiating ξ and η one obtains

$$\begin{aligned} \frac{d\xi(\boldsymbol{r}, t)}{dt} &= \frac{\partial\xi}{\partial t} + \frac{\partial\xi}{\partial \boldsymbol{r}} \cdot \frac{d\boldsymbol{r}}{dt} \\ &= \xi_t + \nabla\xi \cdot \boldsymbol{v} = 0 \end{aligned} \tag{4.17}$$

and similarly

$$\begin{aligned}\frac{d\eta(\boldsymbol{r},t)}{dt} &= \frac{\partial\eta}{\partial t} + \frac{\partial\eta}{\partial \boldsymbol{r}} \cdot \frac{d\boldsymbol{r}}{dt} \\ &= \eta_t + \nabla\eta \cdot \boldsymbol{v} = 0\end{aligned} \tag{4.18}$$

Pulling the above two equations together one has

$$\boldsymbol{v}(\boldsymbol{r},t) = \frac{(\xi_t \nabla\eta - \eta_t \nabla\xi) \times \Omega}{\omega^2} \tag{4.19}$$

where $\omega = |\Omega|$

With the equation of velocity we may find the superluminal and subluminal region of the vortex world sheet, which is the region where the vortex speed, which is the norm of the vortex velocity, exceeds the light speed $c = 1$ in space-time. From $\eta = 0$ we have $z = 0$, then from $\xi = 0$ we have

$$R^2 + 3t^2 - 1 = 0 \tag{4.20}$$

where $R = \sqrt{x^2 + y^2}$. From equation (4.19), the speed of $\Psi = x^2 + y^2 + z^2 + 2iz + 3t^2 - 1$ is

$$s = \frac{3|t|}{R} = 1 \tag{4.21}$$

Thus together with 4.20, the time when the vortex speed exceed the light speed is

$$t_{lum} = \pm\frac{\sqrt{3}}{6} \tag{4.22}$$

Thus for $t \in (-\frac{\sqrt{3}}{3}, -\frac{\sqrt{3}}{6})$ and $t \in (\frac{\sqrt{3}}{6}, \frac{\sqrt{3}}{3})$ the vortex is superluminal while for $t \in (-\frac{\sqrt{3}}{6}, \frac{\sqrt{3}}{6})$ the vortex is subluminal, as shown in subplot (a) in figure 4.2, where (b) is the region on the vortex world sheet after Lorentz boost.

Before going further it is necessary to discuss the ground of existence of superluminal vortices. In a naive understanding of the theory of relativity, nothing travels faster than light. In a more accurate understanding of relativity, only object of zero mass, such as photons, may travel in the speed of light, and anything carries

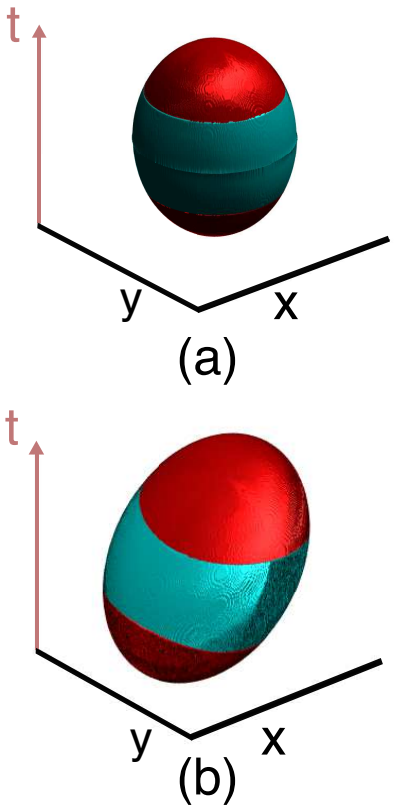

Figure 4.2: Superluminal and subluminal region, colored in red and cyan, on the vortex world sheet of the sphere, and its transformation after the Lorentz boost $v = (0, 0, 0.4c)$

mass or information may not travel faster than the speed of light. However, the phase vortex may travel faster than the speed of light because it is only a phase, rather than a "thing" or object. The reason that phase velocity may be greater than c is that the phase is not an object with mass or information, but only an observation to conscious, which is not concrete as real object.

An example of superluminal phase velocity is the movement of a light from light house as it swipes through the eyes of an observer away, or similarly a light from a torch as it swipes through a region on the wall in front of it. To the observer of the lighthouse or the light spot on the wall, the light may travel faster than the speed of

light, because it is only an illusion that the light is "swiping through". The actual movement of the light is traveling in speed of c straightly from the lighthouse/torch, and it is in reality not swiping around. It is only to the observer who is considering the whole process as one united event, that the light spot appears as moving faster than c. When a light spot on the wall appears at one position and then appears at another position in a later time, the appearance of this two light spot is only "moving" in the eyes of the observer because the observer consider the whole process as one united event. However, in reality, it is just that one light spot appearing at different position, rather than the light spot is truly moving on the wall. What moves is only the light from the torch and the rotation of torch, and the light spot on the wall does not move, yet the light spot only appears as moving to the observer.

This whole process of light spot, as intensity changes at different position and time, is an example of the phase velocity, and how phase velocity may travel faster than c. The phase velocity is not the velocity of a single object moving by itself, but rather an observation to a group of objects whose relative displacement appears as if the intensity is moving with an velocity. Therefore, the phase vortex, which is zeros of the phase, has a concrete ground of traveling faster than c.

The difference between the phase velocity and the velocity of concrete object is that concrete objects have mass, and requires infinite energy for the acceleration to be superluminal, while phase velocity is only an appearance, and exist only depending to the recognition of observer. However, this dependence to observer is different to the uncertainty principle in quantum mechanics, because the observation does not affect the phase velocity. Yet, the existence of phase velocity requires the recognition to the appearance of incidence as one united event.

Besides loop creation and annihilation, another type of topological event is the reconnection, as shown in figure 4.3.

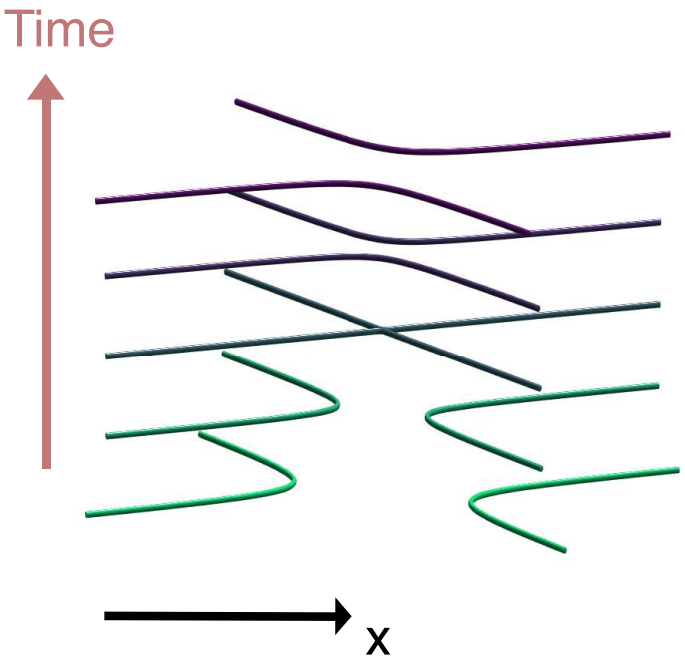

Figure 4.3: The vortex world sheet of reconnection process. Two curves approaches close and cross each other, and then become another two curves that have different two-ends to curves before the reconnection.

The reconnection is a process of three different states, which is before the crossing, crossing, and after the crossing. For the first stage, consider two curves a and b whose end points are a_1, a_2 and b_1, b_2, like the bottom two curves in figure 4.3, and they tend closer and closer to each other. Then at the crossing state, a and b intersect at a point, as the third layer in the figure. Then at the third state, the there are two separate curves, but they are not a and b, because the end points have changes. The two curves may be named c and d because the two end points of c is a_1, b_1 while the two end points of d is a_2, b_2, as shown in the upper two curves in the figure. Therefore, the reconnection is a process that two curves of end points a_1, a_2 and b_1, b_2 becoming two curves of end points a_1, b_1 and a_2, b_2 gradually with a middle state where two curves intersect with each other.

The equation of this reconnection is simply a complex hyperbolic equation. The basic hyperbolic equation writes

$$\frac{x^2}{a^2} + \frac{y^2}{b^2} - \frac{z^2}{c^2} - 1 = 0 \tag{4.23}$$

and our complex analogue to it is

$$ax^2 + by^2 + cz^2 + idz + e = 0 \tag{4.24}$$

Through our transformation F, the 3+1D transformation of equation (4.24) is

$$e + ax^2 + by^2 + cz^2 + idz + (a + b + c)t^2 = 0 \tag{4.25}$$

If we set $(a, b, c, d, e) = (-1, 1, -1, 1, 1)$, then the speed of vortex in equation (4.25) is

$$\text{speed} = \frac{t^2}{\sqrt{X^2 + Y^2}} \tag{4.26}$$

and if we set $(a, b, c, d, e) = (-2, 1, -1, 1, 2)$ for the reconnection simulation, then the speed of vortex in equation (4.25) is

$$\text{speed} = \frac{2|t|}{\sqrt{4X^2 + Y^2}} \tag{4.27}$$

The superluminal and subluminal region on the vortex world sheet of the reconnection and its transformation after the Lorentz boost $v = (0, 0, 0.4c)$ is shown in subplot (a) and (b) of figure 4.4.

It is worth noticing that on a single simultaneous vortex it is possible that part of it is superluminal while part of it is subluminal, as shown in figure 4.4. On the surface of the manifold the centre region is superluminal, while the vortex is the total horizontal cross-section, meaning that part of the vortex near the center is superluminal while part of it near the edge of the manifold is subluminal.

The reason that we state the loop creation and the reconnection to be two fundamental topological events for vortex world sheet is that they have different

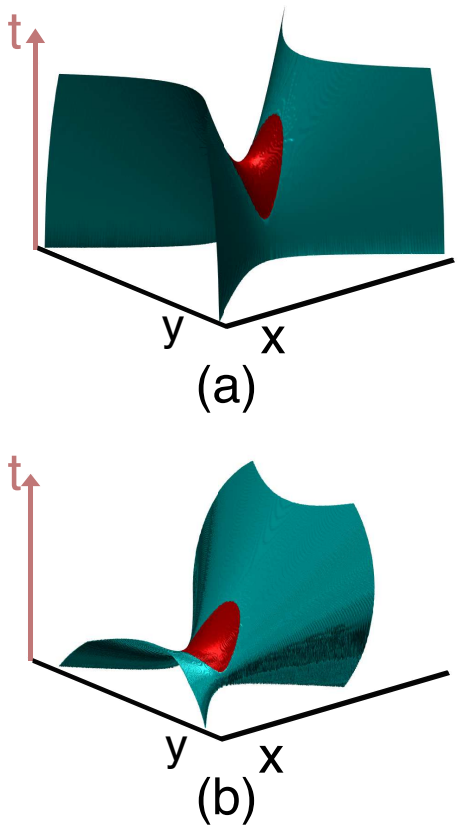

Figure 4.4: Superluminal and subluminal region, colored in red and cyan, on the vortex world sheet of the reconnection, and its transformation after the Lorentz boost $v = (0, 0, 0.4c)$

index value in terms of critical point on a 2-surface. At each time cross-section of the space time, which is a 3D space, the vortex loops are topologically equivalent to a one-dimensional sphere, S^1. Then the vortex world sheet, which is what the vortex loop swipes through in time, may become a 2-surface, which is a two-dimensional manifold that can be transformed from a plane. By definition, a point on a surface has two degrees of freedom: on each vortex line points have one degree of freedom, and then as vortex lines move in time, these points also move in time with another degree of freedom, thus in total space-time points on the vortex world sheet move in two degrees of freedom.

For comparison and local conclusion, we plot the sphere and the reconnection together, in terms of separated vortices, vortex world sheet in space-time distinguishing superluminal and subluminal region, and vortex world sheet both after Lorentz boost $v = (0, 0, 0.4c)$ while distinguishing superluminal and subluminal region in figure 4.5.

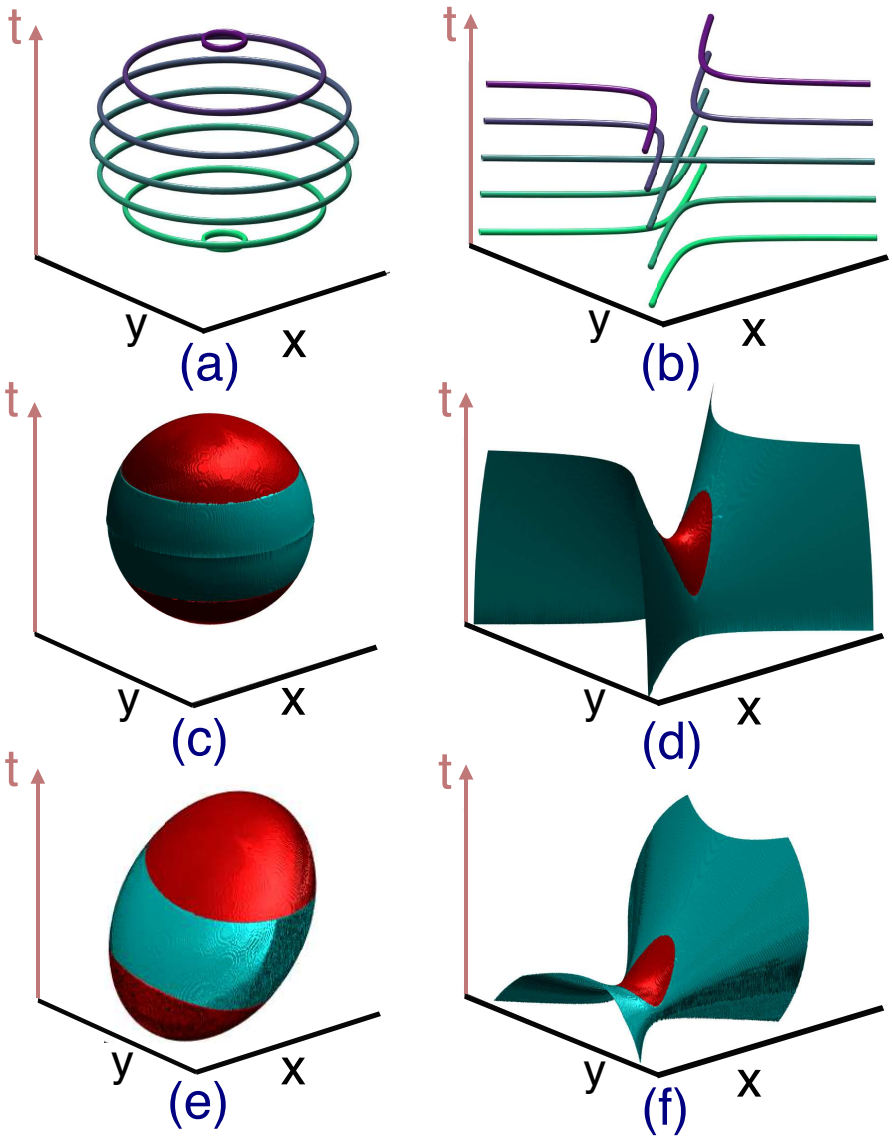

Figure 4.5: Superluminal and subluminal region, colored in red and cyan, on the vortex worldsheet of the sphere and the reconnection, and their transformation after the Lorentz boost $v = (0, 0, 0.4c)$

The loop creation and annihilation event marks local maximum and minimum of the vortex world sheet and have index value $+1$, and they are the source and sink on the sphere of its vortex world sheet. On the other hand, the intersection point during the reconnection is a saddle point. Denoting the curves before the reconnection as a_1, a_2 and b_1, b_2, and after the reconnection is a_1, b_1 and a_2, b_2, then suppose the first vortex is going from a_1 to a_2 and the second vortex is going from b_2 to b_1, then after the reconnection the curve is going from a_1 to b_1 and then b_2 to a_1. Therefore, at the intersection point of the four segments, the vortex is going inward on two face-to-face segments and going outward on two face-to-face segments. Thus on one dimension it is sinking while on the other dimension it is sourcing, so that it is a saddle point.

Since a critical point in vector field is either a sink/source or a saddle point, the loop creation/annihilation and reconnection represent the two types of fundamental topological events. With the PH theorem equation (1.32) they are linked to the Euler characteristic of the vortex world sheet.

We may apply the PH theorem to the examples of loop creation and annihilation, and to the loop reconnection. The Euler characteristic of a sphere is 2, and the vector field on it has one source and one sink whose sum of index is 2. A single reconnection has a saddle point whose index is -1, and its vortex world sheet is equivalent to a solid whose vector field is pointing inward, so k is odd, then together there is $\sum \text{index} = -1 = -1 \cdot 1 = \chi$.

We now verify another fundamental example which is the vortex world sheet

of field

$$\begin{aligned}\Psi_{torus} = {} & 4a^3 + a^4 + 5t^4 + 4a(t^2 - (x+iy)^2 + (i+z)^2) \\ & + 10t^2(x^2 + y^2 + (i+z)^2) + ((-2+x)x + y(-2i+y) \\ & + (i+z)^2)(x(2+x) + y(2i+y) + (i+z)^2) \\ & + 2a^2(1 + t^2 - x^2 + y^2 + z(2i+z))\end{aligned} \tag{4.28}$$

which is a torus shown in figure 4.6. The figure4.6 is another example of verifying

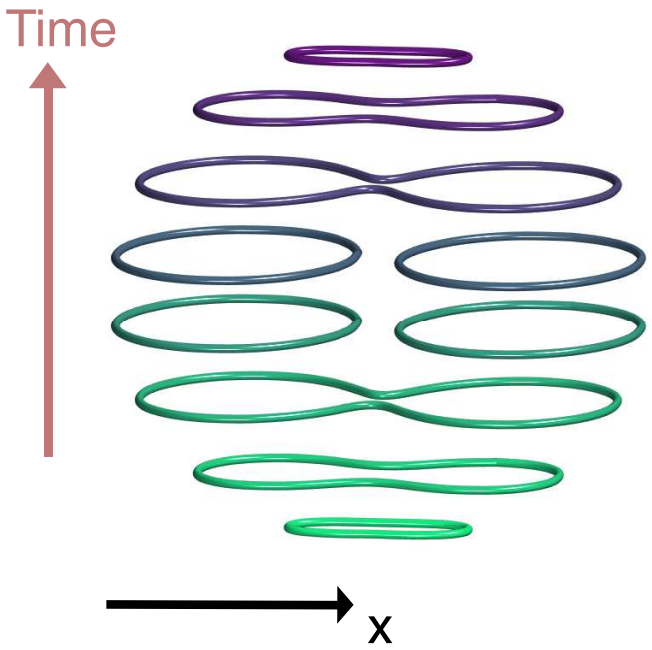

Figure 4.6: The vortex world sheet of Ψ_{torus} that forms a torus in space-time. The whole process includes a loop creation, a reconnection, and the above reversed which is a reconnection and then a loop annihilation.

the PH theorem. On the torus, there are two reconnections, whose sum of index is -2, and there is a loop creation and annihilation, whose sum of index is 2, thus in total the index of critical points on the torus is 0, and it agrees to the Euler characteristic of a torus which is zero.

As we are now familiar with these fundamental topological events, at the end of this subsection we quickly revisit the Lorentz transformation for preparation to the next subsection. The Lorentz transformation does not change the topology of the vortex worldsheet in space-time, but it changes the topology of what appears in time-slice.

The Lorentz transformation is a basic concept in physics describing how the space-time in one frame of reference is transformed into another frame of reference. Let the space-time X_1 be (x, y, z, t), then the space-time after a Lorentz transformation with velocity $\boldsymbol{v} = (v_x, v_y, v_z)$ is $X_1 \cdot B$ where

$$B = \begin{pmatrix} \gamma & -\gamma v_x & -\gamma v_y & -\gamma v_z \\ -\gamma v_x & 1 + (\gamma - 1)\frac{v_x^2}{v^2} & (\gamma - 1)\frac{v_x v_y}{v^2} & (\gamma - 1)\frac{v_x v_z}{v^2} \\ -\gamma v_y & (\gamma - 1)\frac{v_x v_y}{v^2} & 1 + (\gamma - 1)\frac{v_y^2}{v^2} & (\gamma - 1)\frac{v_y v_z}{v^2} \\ -\gamma v_z & (\gamma - 1)\frac{v_x v_z}{v^2} & (\gamma - 1)\frac{v_y v_z}{v^2} & 1 + (\gamma - 1)\frac{v_z^2}{v^2} \end{pmatrix} \tag{4.29}$$

as $\gamma = 1/\sqrt{1 - v^2}$, and v is normalized in unit of $c = 1$.

It is apparent that the Lorentz transformation does not change the topology of the vortex worldsheet in space-time, because the Lorentz transformation is a homeomorphism such that the topology before and after the transformation is equivalent. By definition, a homeomorphism is a continuous bijection whose inverse is also continuous. The Lorentz transformation and its inverse are obviously continuous because they are even differentiable, and it is obviously bijective (one-to-one and onto) from the form of the equation, which is even linear for the Lorentz boost. Thus, the Lorentz transformation is a homeomorphism and does not change the topology of the vortex worldsheet in space-time. However, as we will show in the next subsection, the Lorentz transformation does change the topology in terms of the knot type of time-slice in different frame of reference.

4.2 Knot Dynamics in d'Alembert Equation and Relativistic Decomposition

Now as we have introduced the basic knowledge and example, we discuss in this chapter the dynamics of knots in d'Alembert equation and how they may be decomposed under Lorentz transformation.

The field whose vortex is a trefoil knot is $\Psi = u^2 - v^3$, thus from equation (4.7) the function of the field that satisfy the d'Alembert equation meanwhile has vortex of trefoil knot at time zero is

$$\begin{aligned}
\Psi &= F(u^2 - v^3) \\
&= x^6 + 3x^4y^2 + 3x^4z^2 + x^4z(4i) + 21x^4t^2 - x^4 - 8x^3 + 3x^2y^4 + 6x^2y^2z^2 + x^2y^2z(8i) \\
&+ 42x^2y^2t^2 - 2x^2y^2 + x^2y(-24i) + 3x^2z^4 + x^2z^3(8i) + 42x^2z^2t^2 - 6x^2z^2 + x^2zt^2(56i) \\
&+ 35x^2t^4 - 14x^2t^2 - x^2 + 24xy^2 + y^6 + 3y^4z^2 + y^4z(4i) + 21y^4t^2 - y^4 + y^3(8i) \\
&+ 3y^2z^4 + y^2z^3(8i) + 42y^2z^2t^2 - 6y^2z^2 + y^2zt^2(56i) + 35y^2t^4 - 14y^2t^2 - y^2 + z^6 \\
&+ z^5(4i) + 21z^4t^2 - 5z^4 + z^3t^2(56i) + 35z^2t^4 - 42z^2t^2 - 5z^2 + zt^4((140i)/3) \\
&+ z(-4i) + 7t^6 - (35t^4)/3 - 7t^2 + 1
\end{aligned} \tag{4.30}$$

Observing the vortex in equation (4.30) which is 3+1 dimensional, one may plot the vortex at different time first and then combine them in the same figure as shown in figure 4.7.

In figure 4.7, in temporal sequence firstly there is an event of loop creation. Then the vortex loop grows larger and twists, and then the reconnection takes place and the vortex becomes a trefoil knot. The time of these topological events may be obtained by solving $\Psi = 0$, $x = y = z = 0$ for t, because the vortex implies $\Psi = 0$ while the loop creation, annihilation and reconnection takes place at $x = y = z = 0$

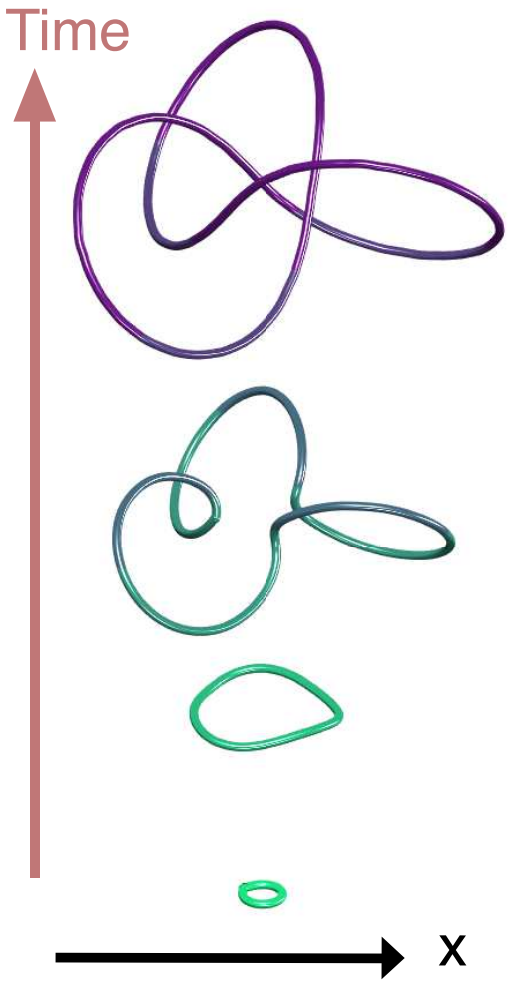

Figure 4.7: The dynamics of formation of knot 3_1 from a critical point. As time advances, the loop creation takes place, and then the loop extends and deforms. After a reconnection the loop become a trefoil knot, and regulate its shape equivalent to the static trefoil knot at t=0. The whole process is from past to time zero.

for the equation. Specifically, the time of topological events solves ± 1.45 and ± 0.35, which corresponds to the loop creation/annihilation and two reconnections, as the whole process shown in figure 4.8

figure 4.8 is a comprehensive illustration to the whole process of the trefoil knot, and is equivalent to figure 4.7 plus its time-reversal. The topological event

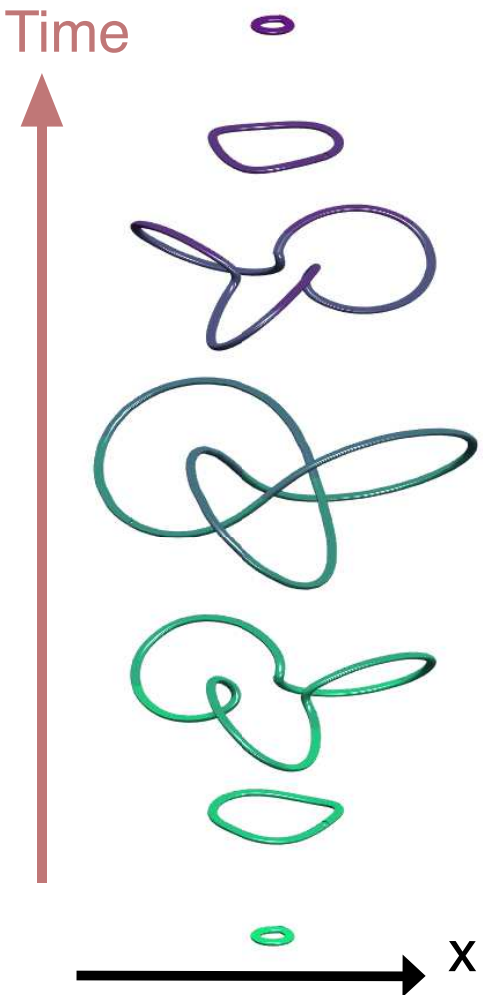

Figure 4.8: The dynamics of formation of knot 3_1 from a critical point and then endure time reversal to merge back. Firstly there is a loop creation, and then the reconnection takes place the vortex becomes a trefoil knot. Afterwards is the time reversal process that the trefoil knot endures a reconnection and decomposes into a loop, which later annihilates.

at $t = \pm 1.45$ corresponds to the loop creation and annihilation at the bottom and the top of figure 4.8. The topological event at $t = \pm 0.35$ corresponds to the two reconnection such that one transforms the loop into a knot while the other one transforms the knot back into the loop. At $t = 0$, the vortex is equivalent to the trefoil knot constructed in static.

The whole process of this trefoil knot dynamics is viewed in time slice, while the whole vortex world sheet is a continuous 2-surface. Since there are one loop creation, one loop annihilation, and two reconnections on the vortex world sheet, from Poincare-Hopf theorem it is easily seen that the total sum of indices is $1+1-2 = 0$, and agrees to the torus whose Euler characteristic is 0. Since the vortex world sheet is oriented 2-surface it is not possible for its manifold to be circle or Klein bottle. It also agrees to the fact that the trefoil knot is a torus knot, meaning that the trefoil knot dwells on the surface of a torus. Therefore, we may see the vortex world sheet as a torus and the whole process in figure 4.8 to be on the surface of a torus.

With same algorithm we construct the field whose vortex at time zero is a figure-eight knot and also satisfy the d'Alembert equation. Recall the static field whose vortex is figure-eight knot is $\Psi = 64u^3 - 12u(3 + 2(v^2 - \bar{v}^2)) - 14(v^2 + \bar{v}^2) - (v^4 - \bar{v}^4)$, then with the transformation F, the 3+1 field equation is

$$
\begin{aligned}
\Psi &= F(64u^3 - 12u(3 + 2(v^2 - \bar{v}^2)) - 14(v^2 + \bar{v}^2) - (v^4 - \bar{v}^4)) \\
&= -7 + 63t^8 + 7x^8 - 96ix^5y + 7y^8 + 78iz + 242z^2 - 278iz^3 - 278iz^5 - 242z^6 + 78iz^7 \\
&+ 7z^8 + y^6(-22 + 78iz + 28z^2) + x^6(-78 + 28y^2 + 78iz + 28z^2) \\
&+ t^6(-798 + 588x^2 + 588y^2 + 1638iz + 588z^2) + y^4(56 - 150iz - 286z^2 + 234iz^3 + 42z^4) \\
&+ y^2(78 - 150iz + 56z^2 - 428iz^3 - 506z^4 + 234iz^5 + 28z^6) \\
&+ x^3(-192iy^3 + y(-32i + 192z - 192iz^2)) \\
&+ x^4(-56 + 42y^4 - 150iz - 398z^2 + 234iz^3 + 42z^4 + y^2(-178 + 234iz + 84z^2)) \\
&+ t^4(882x^4 - 2016ixy + 882y^4 - 2646iz - 6678z^2 + 4914iz^3 + 882z^4 \\
&+ y^2(-2058 + 4914iz + 1764z^2) + x^2(-3234 + 1764y^2 + 4914iz + 1764z^2)) \\
&+ x(-96iy^5 + y^3(32i + 192z - 192iz^2) + y(96i + 192z + 192z^3 - 96iz^4)) \\
&+ x^2(22 + 28y^6 - 150iz - 56z^2 - 428iz^3 - 562z^4 + 234iz^5 + 28z^6 \\
&+ y^4(-122 + 234iz + 84z^2) + y^2(-300iz - 684z^2 + 468iz^3 + 84z^4)) \\
&+ t^2(342 + 252x^6 - 1728ix^3y + 252y^6 - 1134iz - 3636iz^3 - 4698z^4 + 2106iz^5 + 252z^6 \\
&+ y^4(-738 + 2106iz + 756z^2) + x^4(-1746 + 756y^2 + 2106iz + 756z^2) \\
&+ y^2(392 - 2484iz - 5436z^2 + 4212iz^3 + 756z^4) + x(-1728iy^3 + y(1728z - 1728iz^2)) \\
&+ x^2(-392 + 756y^4 - 2484iz - 6444z^2 + 4212iz^3 + 756z^4 \\
&+ y^2(-2484 + 4212iz + 1512z^2)))
\end{aligned}
\tag{4.31}
$$

and the vortex in this 3+1 field is the dynamics of the figure-eight knot, as shown in figure 4.9 and 4.10.

Figure 4.9 shows the formation of a figure-eight knot. Firstly there is a loop creation, then there is another loop creation. Then there is a reconnection so the vortex becomes a link. From the middle of the link there is the third loop creation,

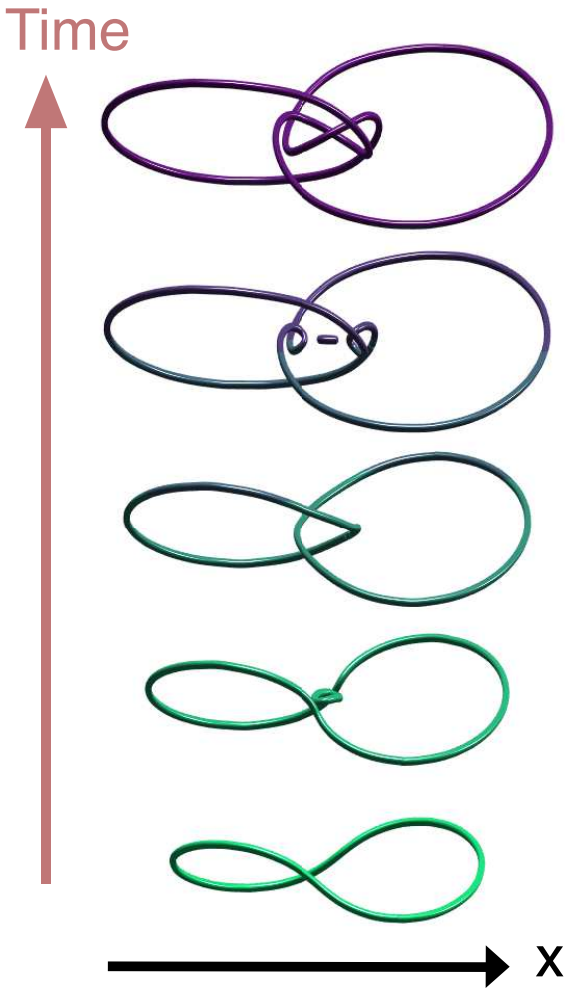

Figure 4.9: The dynamics of formation of knot 4_1. The topological events in chronological order are firstly two loop creation, and then a reconnection to make the vortices into a link. Then there is another loop creation and reconnection, so finally it forms a figure-eight knot.

then it reconnects with the link and the whole vortex becomes a figure-eight knot.

Figure 4.10 is the figure 4.9 plus its time-reversal. There are firstly two loop creation events, then a reconnection transforms the vortex into a link. A loop creation takes places and followed by another reconnection. so at time zero the vortex is a figure-eight knot. Then the vortex endures a reconnection and the

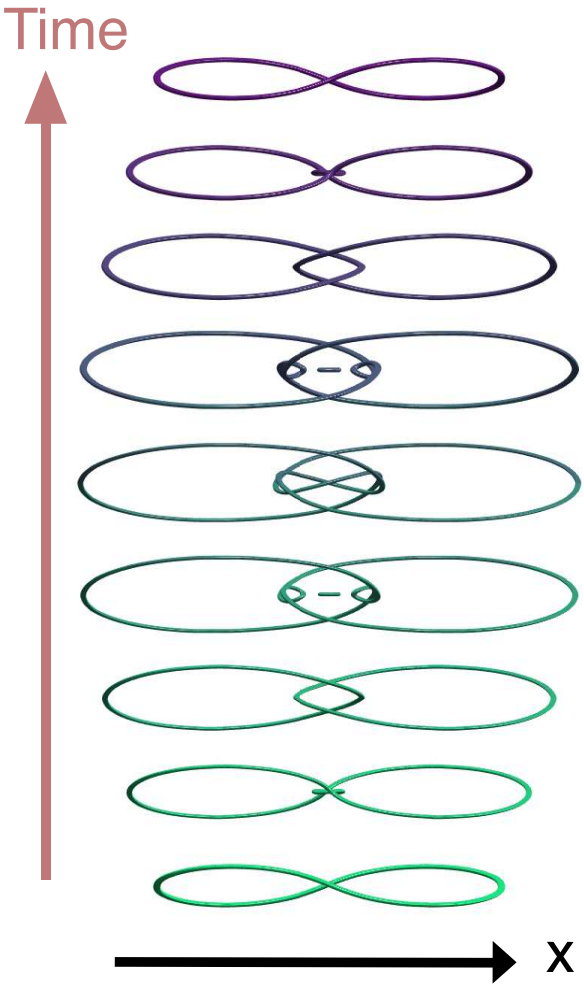

Figure 4.10: The whole process of dynamics knot 4_1, which is figure 4.9 plus its time-reversal.

isolated loop annihilates, so the vortex is a link. Finally, the link reconnects into two loops and the two loops annihilate one after another.

We now show how the figure-eight knot constructed may be decomposed under Lorentz boost such that it is not knotted in another frame of reference.

While in the rest frame of reference the vortex in equation (4.31) becomes figure-eight knot, under a Lorentz boost of velocity $(v_x, v_y, v_z) = (0, 0, 0.4c)$ the vortex never become figure-eight knot nor even knotted, but only a link with a

separated loop, as shown in figure 4.11 and 4.12.

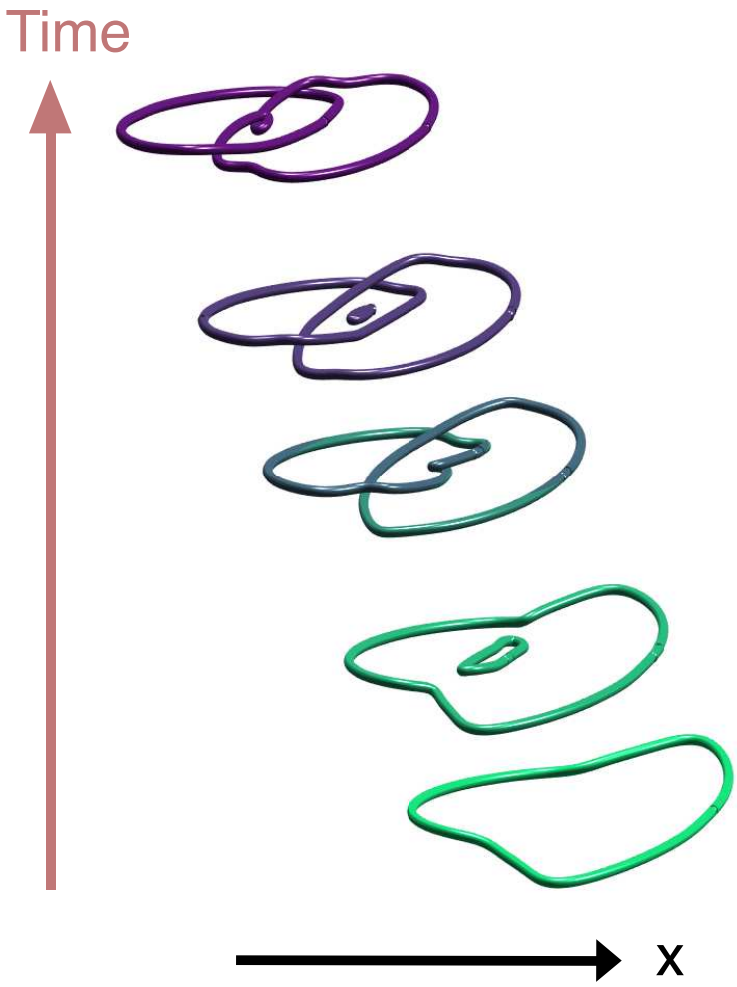

Figure 4.11: The vortex that forms knot 4_1 in the rest frame of reference under a Lorentz boost with velocity $(v_x, v_y, v_z) = (0, 0, 0.4)$. As shown in the plot the Betti number of the space-time manifold does not change but the vortex does not become a figure-right knot. The loop that was born inside the link does not reconnect with the link into a figure-eight knot, but for instead move in the space-time and then get absorbed by one loop of the link.

Figure 4.11 shows the dynamics of the vortex under a Lorentz boost. Firstly there are two loop creations and a reconnection transforming the vortex into a link, and after that, the third loop comes from the reconnection on the side of one link,

yet the third loop does not reconnect with the link in the same way to the vortex in the rest frame. Rather, the third loop moves in isolation to the link, until it is absorbed by the side of the link.

The Betti number of the vortex world sheet in space-time is invariant under Lorentz boost, and both in frame of reference with or without Lorentz boost there are in total three loops. The first two loops form a link in both frames with or without the Lorentz boost, yet the third loop is isolated from the link under the Lorentz boost, while in comparison it reconnect with the link and form into a figure-eight knot in the rest frame. The figure-eight knot and the link plus isolated loop have same Betti number and they slices from two space-time manifolds of equivalent topology, yet they appear of different topology in different frame of reference. Such knot type difference is accounted to "ambient isotopy", which is a measure of whether the ambient space of object can be continuously distorted to another. Loops of different knot type yet with same homology have different ambient isotopy.

Figure 4.12 is the complete process of the vortex world sheet under Lorentz boost. The process is symmetric in time in terms of topological events. In the beginning there are two loop creations and a reconnection transforming them into a link, and correspondingly in the end there are two loop annihilations following an unlinking process. In the middle, there is an isolated loop moving in the middle of the link. To observer it looks like as if the loop is "shooting" or "launching" from one side of the link to another side of the link.

Comparing the complete dynamic process of the vortex loop with and without Lorentz boost in figure 4.12 and figure 4.10, we show that the knot type is not relativistic-invariant, and is dependent to the frame of reference. Without Lorentz boost, the vortex forms a figure-eight knot by reconnecting a link with a loop in the middle of it, however, with Lorentz boost, such loop does not form figure-eight knot

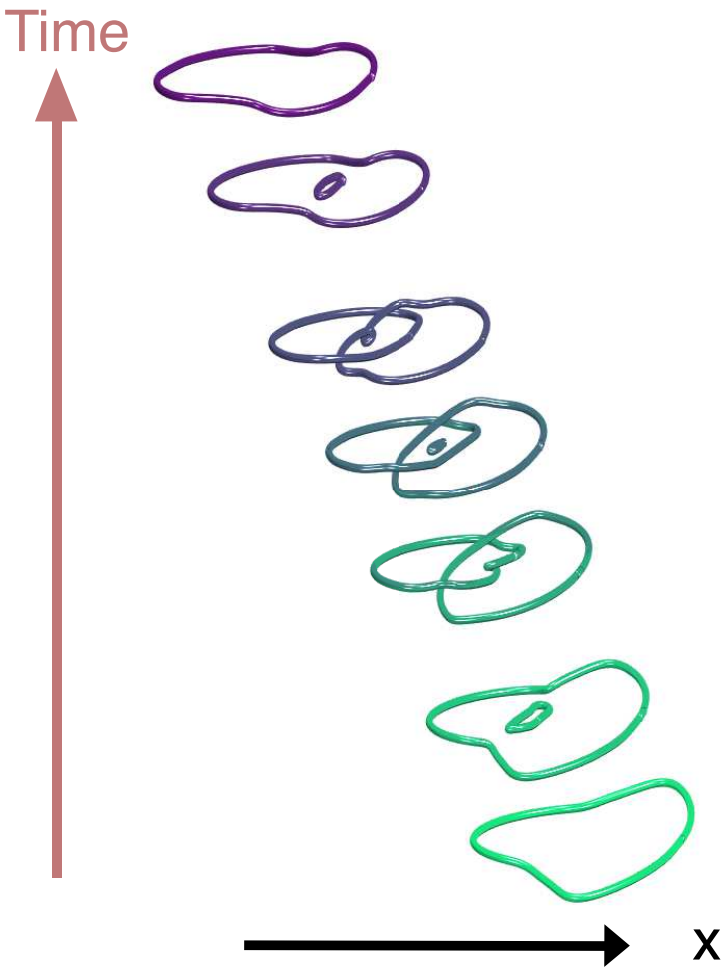

Figure 4.12: The whole process of the figure-eight knot under the Lorentz boost. Unlike figure 4.10 in the rest frame of reference, the vortex under Lorentz boost never become a figure-eight knot.

with the link. The Lorentz boost does not change the overall topology of vortex world sheet in space-time, but it changes the time slice for observers in different frame of reference, and topological events rely on the sequence of emergence of homology. Lorentz boost only bring distortion to the space-time manifold without changing its topology, yet cutting the distorted manifold from different angle leads to different time slice, and bring different sequence of emergence of homologies in the space-time manifold.

In terms of the Poincare-Hopf theorem, there are in total three loop creation and three loop annihilation, and there are in total four reconnections, so the total sum of critical point index is $6-4=2$. Since the velocity is pointing inwards on the boundary to the manifold, the Euler characteristic is $-1 \cdot 2 = -2$. It agrees to the fact that the figure-eight knot is on the surface of a two-holed torus, whose Euler characteristic is -2.

Thus here we arrive at one of the central result in this chapter, that the Lorentz boost brings topology change to time-slice in different frame of reference. Topology as a mathematical concept has been widely adapted in a wide scope of scientific research because it measures invariant that is persistent to perturbations. For example in vortex dynamics, a small perturbation may affect the shape of the vortex, such as bending its local geometry, but it may less likely to change the topology of the vortex, such as a vortex loop is still a loop if its local geometry is changed, while the topology is not changed. However, we now see that topology may be changed under Lorentz boost: a pair of reconnection in the rest frame may appear as a loop in another frame of reference, and a knot may be unknotted in another frame of reference. This finding does not violate the fact that Lorentz boost is a homeomorphism that preserve the topology of space-time manifold, yet it exaggerates the limitation of the observer that observations are only time slice of the space-time, and one may not observe the past and future of an incident simultaneously in the time of his own frame of reference, while such sequence of events may be changed in another frame of reference.

4.3 Designing Knot with Time Dependence in Wave

Equation (4.7) transforms a 3 dimensional wave field whose vortex is a knot as designed, into a 3+1 dimensional wave field where the vortex is the designed knot and its dynamics of emerging and disappearing. However, such 3+1 field has time-reversal symmetry, and the knot at time zero has no "velocity", referring that both the wave field and the time derivative of the wave field is not explicitly containing t at $t = 0$. Now we generalize our construction and show how to construct wave field that is not symmetric in time and has nonzero velocity at time zero.

Taking the trefoil knot as an example. In terms of u, v the field whose vortex is a trefoil knot is $u^2 - v^3$, and it is the state equivalent to the 3+1 wave field at time zero. Obviously $u^2 - v^3$ has no time dependence, yet we may add a time-dependence term to it, and let it be wt. Then, one may design a wave field Ψ

$$\Psi = u^2 - v^3 + \frac{wt}{(x^2 + y^2 + z^2 + 1)^3} \tag{4.32}$$

and for simplicity of calculation without changing its topology by taking its numerator Ψ_n which is

$$\begin{aligned}
\psi_n = {} & x^6 + 3x^4y^2 + 3x^4z^2 + x^4z(4i) - x^4 - 8x^3 \\
& + 3x^2y^4 + 6x^2y^2z^2 + x^2y^2z(8i) - 2x^2y^2 + x^2y(-24i) \\
& + 3x^2z^4 + x^2z^3(8i) - 6x^2z^2 - x^2 + 24xy^2 \\
& + y^6 + 3y^4z^2 + y^4z(4i) - y^4 + y^3(8i) \\
& + 3y^2z^4 + y^2z^3(8i) - 6y^2z^2 - y^2 + z^6 \\
& + z^5(4i) - 5z^4 - 5z^2 + z(-4i) + tw + 1
\end{aligned} \tag{4.33}$$

and send it through the transformation equation (4.7) to obtain

$$\begin{aligned}
F(\Psi_n) = {} & x^6 + 3x^4y^2 + 3x^4z^2 + x^4z(4i) + 21x^4c^2t^2 \\
& - x^4 - 8x^3 + 3x^2y^4 + 6x^2y^2z^2 + x^2y^2z(8i) \\
& + 42x^2y^2c^2t^2 - 2x^2y^2 + x^2y(-24i) + 3x^2z^4 \\
& + x^2z^3(8i) + 42x^2z^2c^2t^2 - 6x^2z^2 \\
& + x^2zc^2t^2(56i) + 35x^2c^4t^4 - 14x^2c^2t^2 \\
& - x^2 + 24xy^2 + y^6 + 3y^4z^2 + y^4z(4i) \\
& + 21y^4c^2t^2 - y^4 + y^3(8i) + 3y^2z^4 + y^2z^3(8i) \\
& + 42y^2z^2c^2t^2 - 6y^2z^2 + y^2zc^2t^2(56i) + 35y^2c^4t^4 \\
& - 14y^2c^2t^2 - y^2 + z^6 + z^5(4i) + 21z^4c^2t^2 \\
& - 5z^4 + z^3c^2t^2(56i) + 35z^2c^4t^4 - 42z^2c^2t^2 \\
& - 5z^2 + zc^4t^4((140i)/3) + z(-4i) + 7c^6t^6 \\
& - (35c^4t^4)/3 - 7c^2t^2 + 2wt + 1
\end{aligned} \tag{4.34}$$

Thus this equation satisfy the d'Alembert equation and has time dependence wt at time zero. For further generality, one may even add term $wxzt$ to the initial state to introduce explicit dependence on these variables. Thus we have

$$\begin{aligned}
\Psi_n = {} & x^6 + 3x^4y^2 + 3x^4z^2 + x^4z(4i) - x^4 - 8x^3 \\
& + 3x^2y^4 + 6x^2y^2z^2 + x^2y^2z(8i) - 2x^2y^2 + x^2y(-24i) \\
& + 3x^2z^4 + x^2z^3(8i) - 6x^2z^2 - x^2 + 24xy^2 + twxz \\
& + y^6 + 3y^4z^2 + y^4z(4i) - y^4 + y^3(8i) + 3y^2z^4 \\
& + y^2z^3(8i) - 6y^2z^2 - y^2 + z^6 + z^5(4i) - 5z^4 - 5z^2 \\
& + z(-4i) + 1
\end{aligned} \tag{4.35}$$

and

$$
\begin{aligned}
F(\Psi_n) = {} & x^6 + 3x^4y^2 + 3x^4z^2 + x^4z(4i) + 21x^4c^2t^2 \\
& - x^4 - 8x^3 + 3x^2y^4 + 6x^2y^2z^2 + x^2y^2z(8i) \\
& + 42x^2y^2c^2t^2 - 2x^2y^2 + x^2y(-24i) + 3x^2z^4 \\
& + x^2z^3(8i) + 42x^2z^2c^2t^2 - 6x^2z^2 \\
& + x^2zc^2t^2(56i) + 35x^2c^4t^4 - 14x^2c^2t^2 \\
& - x^2 + 24xy^2 + 2wxzt + y^6 + 3y^4z^2 + y^4z(4i) \\
& + 21y^4c^2t^2 - y^4 + y^3(8i) + 3y^2z^4 + y^2z^3(8i) \\
& + 42y^2z^2c^2t^2 - 6y^2z^2 + y^2zc^2t^2(56i) \\
& + 35y^2c^4t^4 - 14y^2c^2t^2 - y^2 + z^6 + z^5(4i) \\
& + 21z^4c^2t^2 - 5z^4 + z^3c^2t^2(56i) \\
& + 35z^2c^4t^4 - 42z^2c^2t^2 - 5z^2 + zc^4t^4((140i)/3) \\
& + z(-4i) + 7c^6t^6 - (35c^4t^4)/3 - 7c^2t^2 + 1
\end{aligned}
\tag{4.36}
$$

and the vortex evolution of field equation (4.36) is shown in figure 4.13.

The evolution of vortex in figure 4.13 shows how we break time-reversal symmetry of knot dynamics with extra term in construction. Before time zero, there is a single loop creation, and such loop endures a reconnection and become a trefoil knot. However, after time zero the trefoil knot does not decompose in the same way to what happened before time zero. For instead, the trefoil knot firstly endures one reconnection and become a link. Then, there is another reconnection and the link become two separated loops. In the third step one of the loop has another reconnection and become two separated loops, so there are in total three loops. As time advances, these three loops disappear one after another. In total there are one loop creation and three loop annihilation, and four reconnections, so the total index sum is zero, as trefoil knots dwells on the surface of torus whose Euler characteristic is

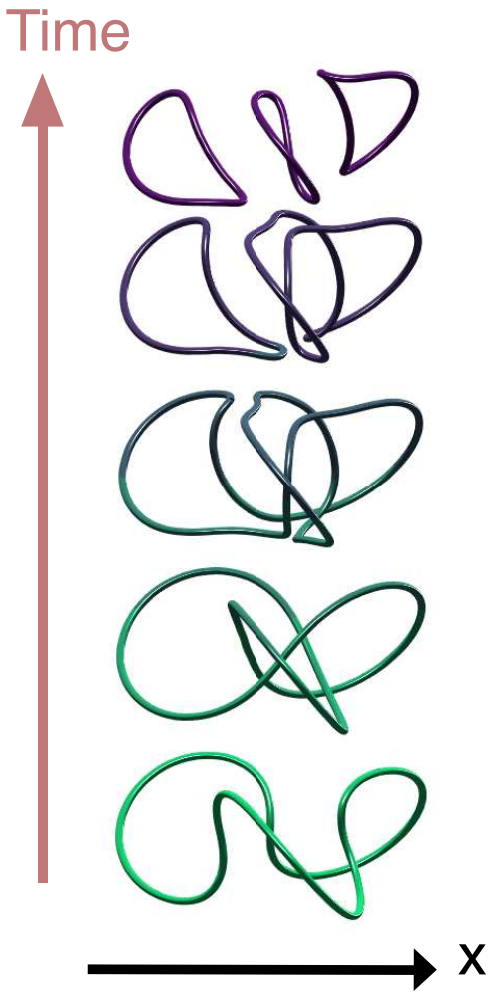

Figure 4.13: Vortex evolution in wave field of equation (4.36). The evolution is not symmetric in time. For negative time the loop undergoes a reconnection and form into a knot like figure 4.7, however, for positive time the knot does not decompose in the same way. The trefoil knot firstly undergoes a reconnection and become a link, then another reconnection transform the link into two separated loops. Then the loop on the right undergoes a reconnection and becomes two separated loops. In the end, these three loops vanish.

zero.

In this construction, we show how to design a 3+1 dimensional wave field that

satisfies the d'Alembert equation as exhibit dynamics of certain knot type design in 3 dimensional space, and such dynamics can be either symmetric in time or not depending on the state of the knot at time zero.

4.4 Vortex Worldsheet in Random Wave

In random wave model there exists an abundant amount of topology change of vortex lines as they move in space. In three-dimensional world as vortex lines move around, their behaviour may be represented by 3+1 random wave model in various scenarios. Here we study a specific example of random wave model, which is the 3+1 dimensional random wave ensemble as the solution to d'Alembert equation, which is

$$\Psi(\boldsymbol{r}, t) = \sum_{\boldsymbol{k}} a_{\boldsymbol{k}} \exp(i(\boldsymbol{k} \cdot \boldsymbol{r} - \omega t) \tag{4.37}$$

for $\boldsymbol{r} = (x, y, z)$ and $\boldsymbol{k} = \sqrt{x^2 + y^2 + z^2}$, and specifically in a periodic boundary condition which explicitly writes

$$\Psi(x, y, z, t) = \sum_{l,m,n=-N}^{N} a_{\boldsymbol{k}} \exp(2\pi i[(lx + my + nz)/L_0 - kt/T_0]) \tag{4.38}$$

As vortex lines move in 3+1 space they have various topology change, specifically we present a loop emerging from a reconnection of a single line and merge into another vortex line by another reconnection, as shown in figure 4.14

Figure 4.14 plots the dynamics of a specific process of vortex topology change. At the first stage, vortex lines are plotted in green, then, as color get darker, there is a loop emerged from a reconnection of the curve on the bottom right plotted in light green. Then at the third stage where vortices are plotted in purple, the loop vanishes because it is absorbed into another vortex line on the top left. Therefore it

Figure 4.14: A local area in the 3+1 random wave model. As time advances, a loop emerges from a reconnection, and then is absorbed in reconnection with another vortex line.

reveals the process of a vortex line bends to reconnect and gives a loop, then such loop is absorbed and merged into another vortex line.

Chapter Five

Conclusion

In this thesis, we present results on analysis of random curve and vortex filament in different scenarios. We believe this thesis reveals certain universality of curves and vortex filaments in random models such as the random wave model, and connects random field to their geometry and topology reflection in terms of knot theory. Furthermore, we present new findings on the topology of vortex worldsheet, which is a direct illustration to the topology of surfaces in space-time.

In chapter two, we study the vortices in random wave model and find that their statistical behaviour may be categorized based on length. While vortices in small scale are not fully developed and behave depending on specific models, as their length become large enough, they behave like random walks among all searched models, which are 2+1 dimensional wave as solution to d'Alembert, Schrödinger, and Klein-Gordon equation, and three dimensional wave as solution to Helmholtz equation. These vortex loops not only behave like closed random walks, their length distribution is also of universal scaling relation, whose gradient is near $-\frac{5}{2}$ as theoretical prediction agrees to numerical finding. Another universal scaling relation is of the length distribution of very long vortices that are long enough to penetrate through the boundary. They may be effectively seen as segments of a super gigantic

loop cut by the boundary, and they appear as lines rather than loops. The gradient of such scaling relation is $-\frac{3}{2}$, as theoretical prediction agrees to numerical analysis.

The universal scaling relation of vortices exists independent to specific choice of random wave model, and thus reveal the universality rising from the global statistical perspective to random waves such as classifying vortices based on homology. Furthermore, we find the vortices long enough to be model dependent are closed random walks, which are also known as random polygons, and we further investigate the probability of knot in random polygons in chapter three.

In chapter three, we investigate the probability of knot in random polygon, which is a fundamental question for random walk in three-dimensional space reflecting the topology nature of it. We raise a general equation for the knot probability of equilateral and non-equilateral random polygons and verify the equation by a high quality massive data generated by my supervisor's former postdoc. Our result answers the question of knot probability which is a very old question, and since our result is in R^3, it generalize previous knowledge in Z^3, and show why it is necessary to adapt our new equation for knot probability in R^3. We believe our result may be applied a broad range of studies regarding random curves in three-dimensional space such as vortices, polymers, proteins, and many other.

In chapter four, we study the vortices rather from a deterministic construction than from random search. We generalize previous construction of knotted vortices in 3D static complex field into construction of knotted vortices in 3+1D space-time obeying the d'Alembert equation. The vortices swipes through space in time and thus become vortex worldsheet in 3+1D space-time. We find that while the topology of the vortex worldsheet in Lorenz-invariant, the topology of vortices in time-slice is dependent to the reference frame of observers under Lorentz transformation. We give example of how the same space-time vortex worldsheet may appear as of different

knot type in different frame of reference under Lorentz transformation, that while the homology is preserved, the ambient isotopy is relativistic-dependent.

Since knots are closely related to fundamental quantities of the field such as the helicity and Chern-Simons action, we expect further studies will reveal the significance of the finding that the topology of vortices in time-slice is depending on relativity in an even deeper way. We also plan to study the topology of vortex worldsheet in 3+1 dimensional wave chaos in the future.

References

[Ale28] J. W. Alexander. "Topological Invariants of Knots and Links". In: *Transactions of the American Mathematical Society* 30.2 (1928), pp. 275–306. ISSN: 00029947.

[Alp+18] F. Alpeggiani et al. "Electromagnetic helicity in complex media". In: *Physical review letters* 120.24 (2018), p. 243605.

[BD00] M. V. Berry and M. R. Dennis. "Phase Singularities in Isotropic Random Waves". In: *Proceedings: Mathematical, Physical and Engineering Sciences* 456.2001 (2000), pp. 2059–2079. ISSN: 13645021.

[Ber78] M. V. Berry. "Disruption of wavefronts: statistics of dislocations in incoherent Gaussian random waves". In: *Journal of Physics A* 11 (1978), pp. 27–37.

[Ber89] M. V. Berry. "Quantum chaology, not quantum chaos". In: *Physica Scripta* 40.3 (Sept. 1989), pp. 335–336.

[BF84] M. A. Berger and G. B. Field. "The topological properties of magnetic helicity". In: *Journal of Fluid Mechanics* 147 (1984), pp. 133–148.

[BGS02] G. Blum, S. Gnutzmann, and U. Smilansky. "Nodal Domains Statistics: A Criterion for Quantum Chaos". In: *Physical Review Letters* 88.11 (Mar. 2002).

[BGS84] O. Bohigas, M. J. Giannoni, and C. Schmit. "Characterization of Chaotic Quantum Spectra and Universality of Level Fluctuation Laws". In: *Phys. Rev. Lett.* 52 (1 Jan. 1984), pp. 1–4.

[Bra28] K. Brauner. "Zur Geometrie der Funktionen zweier komplexer Veränderlicher. II: Das Verhalten der Funktionen in der Umgebung ihrer Verzweigungsstellen. III: Klassifikation der Singularitäten algebroider Kurven. IV: Die Verzweigungsgruppen." German. In: *Abhandlungen Hamburg* 6 (1928), pp. 1–55.

[BT77] M. V. Berry and M. Tabor. "Level Clustering in the Regular Spectrum". In: *Proceedings of the Royal Society of London. Series A, Mathematical and Physical Sciences* 356.1686 (1977), pp. 375–394. ISSN: 00804630.

[Căl59] G. Călugăreanu. "L'int´egral de Gauss et l'analyse des nœuds tridimensionnels". In: *Rev. Math. Pures Appl.* 4 (1959), pp. 5–20.

[Căl61] G. Călugăreanu. "Sur les classes d'isotopie des noeuds tridimensionels et leurs invariants". In: *Czechoslovak Math. J.* 11 (1961), pp. 588–625.

[Can+16] J. Cantarella et al. "A fast direct sampling algorithm for equilateral closed polygons". In: *Journal of Physics A: Mathematical and Theoretical* 49.27 (May 2016), p. 275202.

[CDS13] J. Cantarella, T. Deguchi, and C. Shonkwiler. "Probability Theory of Random Polygons from the Quaternionic Viewpoint". In: *Communications on Pure and Applied Mathematics* 67.10 (Aug. 2013), pp. 1658–1699. ISSN: 0010-3640.

[CH08] R. Courant and D. Hilbert. *Methods of mathematical physics: partial differential equations*. John Wiley & Sons, 2008.

[DAK18] L. De Angelis, F. Alpeggiani, and L. Kuipers. “Spatial Bunching of Same-Index Polarization Singularities in Two-Dimensional Random Vector Waves”. In: *Phys. Rev. X* 8 (4 Oct. 2018), p. 041012.

[Den+10] M. R. Dennis et al. “Isolated optical vortex knots”. In: *Nature Physics* 6.2 (2010), pp. 118–121.

[Den07] M. R. Dennis. “Nodal densities of planar gaussian random waves”. In: *European Physical Journal: Special Topics* 145 (Jan. 2007), pp. 191–210.

[Den09] M. R Dennis. “On the Burgers vector of a wave dislocation”. In: *Journal of Optics A: Pure and Applied Optics* 11.9 (Aug. 2009), p. 094002. ISSN: 1741-3567.

[Dia95] Y. Diao. “The knotting of equilateral polygons in R3”. In: *Journal of Knot Theory and its Ramifications* 4.02 (1995), pp. 189–196.

[DT94] T. Deguchi and K. Tsurusaki. “A statistical study of random knotting using the Vassiliev invariants”. In: *Journal of Knot Theory and Its Ramifications* 3.03 (1994), pp. 321–353.

[DT97] T. Deguchi and K. Tsurusaki. “Universality of random knotting”. In: *Phys. Rev. E* 55 (5 May 1997), pp. 6245–6248.

[Ham61] J. M. Hammersley. “The number of polygons on a lattice”. In: *Mathematical Proceedings of the Cambridge Philosophical Society* 57.3 (1961), pp. 516–523.

[Hat02] A. Hatcher. *Algebraic Topology*. Cambridge University Press, 2002.

[HK97] J. Hausmann and A. Knutson. “Polygon spaces and Grassmannians”. In: *Enseign. Math* 43.2 (1997), pp. 173–198.

[Jon87] V. F. R. Jones. “Hecke Algebra Representations of Braid Groups and Link Polynomials”. In: *Annals of Mathematics* 126.2 (1987), pp. 335–388. ISSN: 0003486X.

[JR11] E J Janse van Rensburg and A Rechnitzer. “On the universality of knot probability ratios”. In: *Journal of Physics A: Mathematical and Theoretical* 44.16 (Mar. 2011), p. 162002.

[KBS01] D. Kivotides, C. F. Barenghi, and D. C. Samuels. “Fractal dimension of superfluid turbulence”. In: *Physical Review Letters* 87.15 (2001), p. 155301.

[Ked+16] H. Kedia et al. “Weaving Knotted Vector Fields with Tunable Helicity”. In: *Physical Review Letters* 117.27 (Dec. 2016).

[KI13] D. Kleckner and W. Irvine. “Creation and dynamics of knotted vortices”. In: *Nature physics* 9.4 (2013), pp. 253–258.

[Lee13] J. M. Lee. “Smooth manifolds”. In: *Introduction to Smooth Manifolds*. Springer, 2013, pp. 1–31.

[LM10] O. Legrand and F. Mortessagne. “Wave chaos for the Helmholtz equation”. In: *New Directions in Linear Acoustics and Vibration*. Ed. by Matthew Wright & Richard Weaver. Cambridge University Press, 2010, pp. 24–41.

[Lon57] M. S. Longuet-Higgins. “Statistical Properties of an Isotropic Random Surface”. In: *Philosophical Transactions of the Royal Society of London. Series A, Mathematical and Physical Sciences* 250.975 (1957), pp. 157–174. ISSN: 00804614.

[LR12] X. Liu and R. L. Ricca. “The Jones polynomial for fluid knots from helicity”. In: *Journal of Physics A: Mathematical and Theoretical* 45.20 (May 2012), p. 205501.

[MA14] T. Machon and G. P. Alexander. "Knotted Defects in Nematic Liquid Crystals". In: *Phys. Rev. Lett.* 113 (2 July 2014), p. 027801.

[Mag+13] F. Maggioni et al. "Vortex knots dynamics in Euler fluids". In: *Procedia IUTAM* 7 (2013), pp. 29–38.

[Mil16] J. Milnor. "Singular Points of Complex Hypersurfaces.(AM-61), Volume 61". In: *Singular Points of Complex Hypersurfaces.(AM-61), Volume 61*. Princeton University Press, 2016.

[MK88] S. W. McDonald and A. N. Kaufman. "Wave chaos in the stadium: Statistical properties of short-wave solutions of the Helmholtz equation". In: *Phys. Rev. A* 37 (8 Apr. 1988), pp. 3067–3086.

[MR92] H. K. Moffatt and R. L. Ricca. "Helicity and the Călugăreanu invariant". In: *Proceedings: Mathematical and Physical Sciences* 439.1906 (1992), pp. 411–429.

[MT92] H. K. Moffatt and A. Tsinober. "Helicity in laminar and turbulent flow". In: *Annual review of fluid mechanics* 24.1 (1992), pp. 281–312.

[Nah+13] A. Nahum et al. "Length Distributions in Loop Soups". In: *Phys. Rev. Lett.* 111 (10 Sept. 2013), p. 100601.

[ODP09] K. O'holleran, M. R. Dennis, and M. J. Padgett. "Topology of light's darkness". In: *Physical review letters* 102.14 (2009), p. 143902.

[OHo+08] K. O'Holleran et al. "Fractality of Light's Darkness". In: *Physical review letters* 100 (Mar. 2008), p. 053902.

[OW07] E. Orlandini and S. G. Whittington. "Statistical topology of closed curves: Some applications in polymer physics". In: *Rev. Mod. Phys.* 79 (2 Apr. 2007), pp. 611–642.

[Pis99] Len M Pismen. *Vortices in nonlinear fields: from liquid crystals to superfluids, from non-equilibrium patterns to cosmic strings*. Vol. 100. Oxford University Press, 1999.

[POB12] D. Proment, M. Onorato, and C. F. Barenghi. "Vortex knots in a Bose-Einstein condensate". In: *Physical Review E* 85.3 (2012), p. 036306.

[Ric98] R. Ricca. "Applications of knot theory in fluid mechanics". In: *Banach Center Publications* 42 (1998), pp. 321–346.

[Rol76] D. Rolfsen. *Knots and links*. Publish or Perish, 1976.

[RSB99] R. L. Ricca, D. C Samuels, and C. F. Barenghi. "Evolution of vortex knots". In: *Journal of Fluid Mechanics* 391 (1999), pp. 29–44.

[RW11] G Rychlewski and S. G. Whittington. "Self-avoiding walks and polymer adsorption: low temperature behaviour". In: *Journal of Statistical Physics* 145.3 (2011), pp. 661–668.

[SBR98] D. C Samuels, C. F. Barenghi, and R. L. Ricca. "Quantized vortex knots". In: *Journal of Low Temperature Physics* 110.1 (1998), pp. 509–514.

[Sin70] Y. Sinai. "Dynamical systems with elastic reflections. Ergodic properties of dispersing billiards". In: *Uspekhi Matematicheskikh Nauk* 25.2 (1970), pp. 141–192.

[Spr03] J. C. Sprott. *Chaos and time-series analysis*. Vol. 69. Oxford University Press Oxford, 2003.

[Str18] S. H Strogatz. *Nonlinear dynamics and chaos: with applications to physics, biology, chemistry, and engineering*. CRC press, 2018.

[SW88] D W Sumners and S G Whittington. "Knots in self-avoiding walks". In: *Journal of Physics A: Mathematical and General* 21.7 (Apr. 1988), pp. 1689–1694.

[TB10] S. Tomsovic and M. Brown. “Ocean Acoustics: A Novel Laboratory for Wave Chaos”. In: *New Directions in Linear Acoustics and Vibration: Quantum Chaos, Random Matrix Theory and Complexity*. Ed. by Matthew Wright and RichardEditors Weaver. Cambridge University Press, 2010, pp. 169–187.

[TR96] J. L. Trueba and A. F. Ranada. “The electromagnetic helicity”. In: *European Journal of Physics* 17.3 (1996), p. 141.

[UD17] E. Uehara and T. Deguchi. “Knotting probability of self-avoiding polygons under a topological constraint”. In: *The Journal of Chemical Physics* 147.9 (2017), p. 094901.

[VV84] T. Vachaspati and A. Vilenkin. “Formation and evolution of cosmic strings”. In: *Phys. Rev. D* 30 (10 Nov. 1984), pp. 2036–2045.

[WDL+98] S. G. Whittington, L Sumners De Witt, T. Lodge, et al. *Topology and geometry in polymer science*. Vol. 103. Springer Science & Business Media, 1998.

[Wit89] E. Witten. “Quantum field theory and the Jones polynomial”. In: *Communications in Mathematical Physics* 121.3 (1989), pp. 351–399.

[Xio+21] A. Xiong et al. “Knot probabilities in equilateral random polygons”. In: *Journal of Physics A: Mathematical and Theoretical* 54.40 (Sept. 2021), p. 405001.

[ZG07] S. Zhang and A. Z. Genack. “Statistics of Diffusive and Localized Fields in the Vortex Core”. In: *Physical Review Letters* 99.20 (Nov. 2007).

[Zhu18] J. Zhu. “Vorticity and helicity decompositions and dynamics with real Schur form of the velocity gradient”. In: *Physics of Fluids* 30.3 (2018), p. 031703.